

AD-A032 409

AIR FORCE WEAPONS LAB KIRTLAND AFB N MEX
SKYLAB II - RADIATION DOSIMETRY SYSTEMS AND FLIGHT RESULTS. (U)
SEP 76 G C AINSWORTH, M F SCHNEIDER

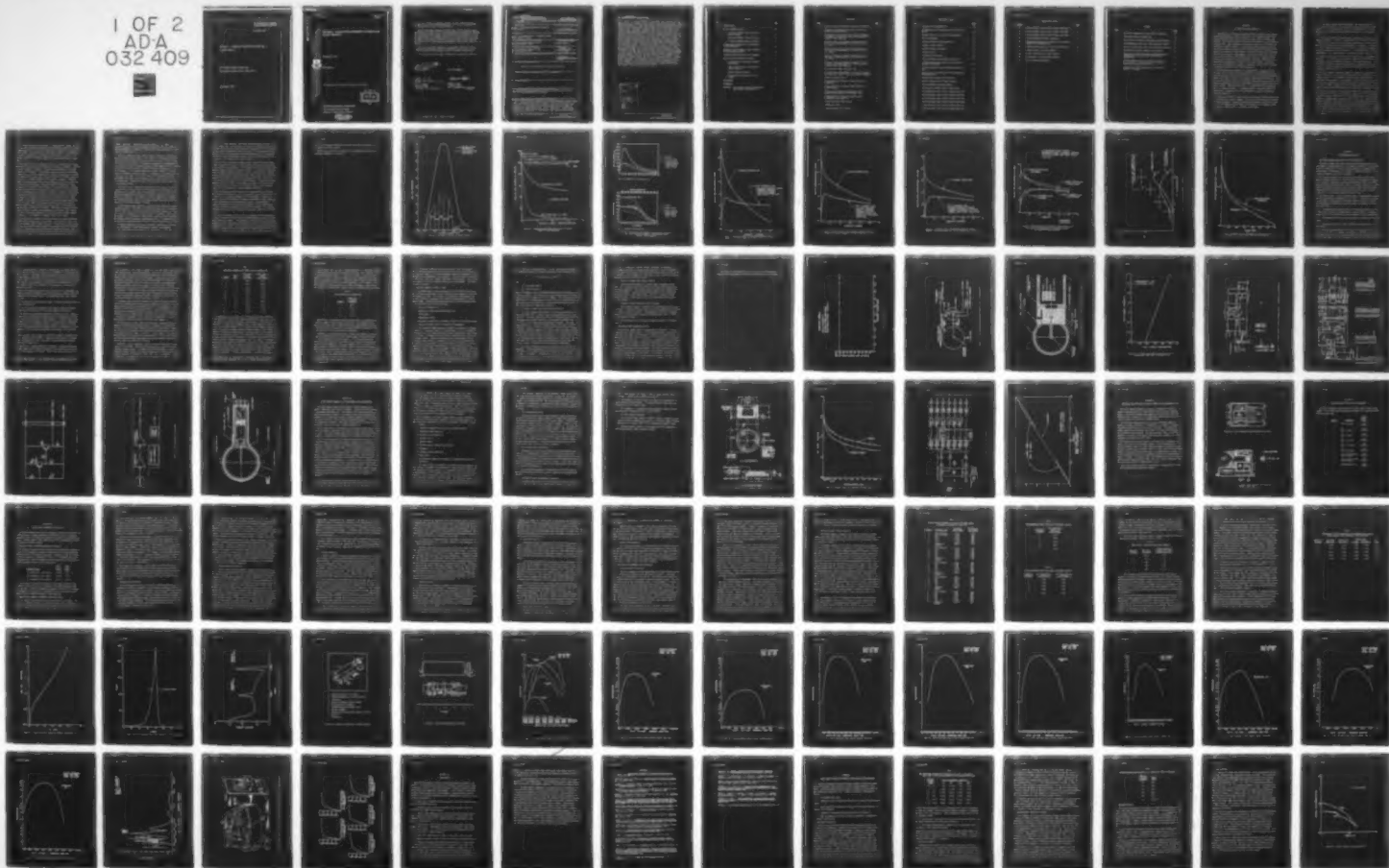
F/G 18/4

UNCLASSIFIED

AFWL-TR-73-222

NL

1 OF 2
AD-A
032 409



**U.S. DEPARTMENT OF COMMERCE
National Technical Information Service**

AD-A032 409

**SKYLAB II - RADIATION DOSIMETRY SYSTEMS AND
FLIGHT RESULTS**

**AIR FORCE WEAPONS LABORATORY
KIRTLAND AIR FORCE BASE, NEW MEXICO**

SEPTEMBER 1976

AD A032409

334111
AFWL-TR-73-222

AFWL-TR-
73-222

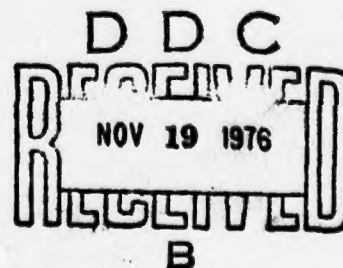
**SKYLAB II - RADIATION DOSIMETRY SYSTEMS AND
FLIGHT RESULTS**

September 1976



Final Report

Approved for public release; distribution unlimited.



AIR FORCE WEAPONS LABORATORY
Air Force Systems Command
Kirtland Air Force Base, NM 87117

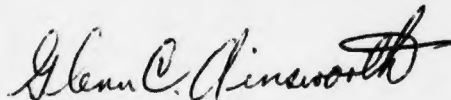
REPRODUCED BY
**NATIONAL TECHNICAL
INFORMATION SERVICE**
U. S. DEPARTMENT OF COMMERCE
SPRINGFIELD, VA. 22161

This final report was prepared by the Air Force Weapons Laboratory, Kirtland AFB, NM, under Job Order 88091815. Mr. Glenn C. Ainsworth (ALE) was the Laboratory Project Officer-in-Charge.

When US Government drawings, specifications, or other data are used for any purpose other than a definitely related Government procurement operation, the Government thereby incurs no responsibility nor any obligation whatsoever, and the fact that the Government may have formulated, furnished, or in any way supplied the said drawings, specifications, or other data is not to be regarded by implication or otherwise as in any manner licensing the holder or any other person or corporation or conveying any rights or permission to manufacture, use, or sell any patented invention that may in any way be related thereto.

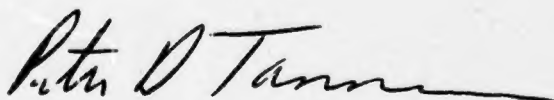
This report has been reviewed by the Information Office (OI) and is releasable to the National Technical Information Service (NTIS). At NTIS, it will be available to the general public, including foreign nations.

This technical report has been reviewed and is approved for publication.

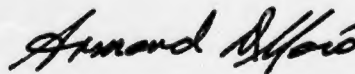


GLENN C. AINSWORTH
Project Officer

FOR THE COMMANDER



PETER D. TANNEN
Lt Colonel, USAF
Chief, Electrical Laser Branch



ARMAND D. MAIO
Lt Colonel, USAF
Chief, Advanced Laser Technology
Division

UNCLASSIFIED

SECURITY CLASSIFICATION OF THIS PAGE (When Data Entered)

REPORT DOCUMENTATION PAGE		READ INSTRUCTIONS BEFORE COMPLETING FORM
1. REPORT NUMBER AFWL-TR-73-222	2. GOVT ACCESSION NO.	3. RECIPIENT'S CATALOG NUMBER
4. TITLE (and Subtitle) SKYLAB II - RADIATION DOSIMETRY SYSTEMS AND FLIGHT RESULTS		5. TYPE OF REPORT & PERIOD COVERED Final Report
		6. PERFORMING ORG. REPORT NUMBER
7. AUTHOR(s) Glenn C. Ainsworth; Marion F. Schneider; Joseph F. Janni; Andrew D. Grimm		8. CONTRACT OR GRANT NUMBER(s)
9. PERFORMING ORGANIZATION NAME AND ADDRESS Air Force Weapons Laboratory (LRE) Kirtland AFB, NM 87117		10. PROGRAM ELEMENT, PROJECT, TASK AREA & WORK UNIT NUMBERS 62610F; 88091815
11. CONTROLLING OFFICE NAME AND ADDRESS Air Force Weapons Laboratory (LRE) Kirtland AFB, NM 87117		12. REPORT DATE September 1976
		13. NUMBER OF PAGES 107
14. MONITORING AGENCY NAME & ADDRESS (if different from Controlling Office)		15. SECURITY CLASS. (of this report) UNCLASSIFIED
		15a. DECLASSIFICATION/DOWNGRADING SCHEDULE
16. DISTRIBUTION STATEMENT (of this Report) Approved for public release; distribution unlimited.		
17. DISTRIBUTION STATEMENT (of the abstract entered in Block 20, if different from Report)		
18. SUPPLEMENTARY NOTES		
19. KEY WORDS (Continue on reverse side if necessary and identify by block number) Van Allen Belts; Space environment; Cosmic rays; Radiobiology; Radiation detectors; Radiation shielding and design		
20. ABSTRACT (Continue on reverse side if necessary and identify by block number) Active and passive dosimetry systems to measure absorbed dose, charged particle spectra, and linear energy transfer spectra inside of the NASA Skylab II space- craft were flown from 25 May to 22 June 1973. The active dosimetry system consisted of a tissue-equivalent ionization chamber which was capable of measuring dose rates from less than 0.2 millirad/hour to 10 rads/hour and silicon solid state detectors which measure linear energy transfer spectra from 2.8 to 42.4 keV/micron, and proton and alpha particle energy spectra from		

UNCLASSIFIED

SECURITY CLASSIFICATION OF THIS PAGE(When Data Entered)

0.5 to 75 MeV. The active dosimeter was equipped with a portable radiation sensor for use in astronaut on-body and spacecraft shielding surveys. Data were transmitted in real time and recorded by onboard spacecraft tape recorders. The passive dosimetry systems were mounted in five fixed locations and contained a variety of passive radiation sensors that were recovered at the end of the mission. The passive dosimeters consisted of calcium and lithium-fluoride thermoluminescent dosimeters, special quartz-fiber ionization chambers, activation foils, Ilford G.5 and K.2 nuclear emulsions, and plastic heavy particle track dosimeters. The passive dosimeters had the capability to record the total mission dose from 5 millirads to 5000 rads and the linear energy transfer spectra from 0.20 to 85 keV/micron. The active dosimeters flown on Skylab II recorded dose rates during passage through the South Atlantic anomaly region of the earth's radiation belts that ranged from 10 millirads/hour for orbits that grazed the anomaly to 83 millirads/hour for more penetrating passes. Cosmic ray dose rates as high as 2.0 millirads/hour with an average dose rate of 0.2 millirads/hour were measured at higher geomagnetic latitudes. The thermoluminescent passive dosimeters recorded a five-location average dose of 1213 millirads for the entire mission compared to a 920 millirad total dose average for the quartz-fiber ionization chambers. Total dose levels for each of the five locations showed a decrease with increased shielding and ranged from 1665 millirads at the location of least shielding to 960 millirads at the location of greatest shielding. Secondary neutron doses were below detectable limits for both the fast and thermal neutron components. The instrumentation functioned as expected and is adequate to assess mixed fields of space radiation on future manned space missions operating in any portion of the earth's radiation belts or during the largest known solar-flare particle events.

ACCESSION for	
HTIS	Write Section <input checked="" type="checkbox"/>
DDC	Both Section <input type="checkbox"/>
UNANNOUNCED	<input type="checkbox"/>
JUSTIFICATION	
BY	
DISTRIBUTION/AVAILABILITY CODES	
Dist.	AVAIL. S&C/OF OFFICE
A	

UNCLASSIFIED

SECURITY CLASSIFICATION OF THIS PAGE(When Data Entered)

CONTENTS

<u>Section</u>		<u>Page</u>
I	INTRODUCTION	7
II	ACTIVE DOSIMETER DESIGN	22
	Ionization Chamber Sensor Theory and Physical Design	22
	Ionization Chamber Electronic Design	27
	Ionization Chamber Mechanical Design	29
III	LINEAR ENERGY TRANSFER (LET) SPECTROMETER SYSTEM DESCRIPTION	40
IV	MECHANICAL AND ELECTRICAL DESIGN OF OVERALL ACTIVE DOSIMETER SYSTEM	48
V	TELEMETRY OUTPUTS FOR THE ACTIVE DOSIMETER	50
VI	APOLLO ACTIVE DOSIMETER TEST RESULTS	51
	Tissue-Equivalent Ionization Chamber Test Results	51
	Linear Energy Transfer Spectrometer Detector Testing	51
	Passive Dosimetry Systems	52
	System Flight Performance Data and Results	57
VII	CONCLUSIONS	83
	REFERENCES	85
	APPENDIX: Linear Energy Transfer Spectrometer Sensor Design Considerations	87

ILLUSTRATIONS

<u>Figure</u>		<u>Page</u>
1	Radiation Shielding Variations for Gemini Spacecraft	13
2	Theoretical Depth-Dose Distribution for Critical Organs in Space Radiations	14
3	Differential and Integral Proton Spectra Integrated over Gemini 4 Mission Duration and Predicted Apollo Integral Proton Spectrum	15
4	Relative Primary and Secondary Radiation Dose as a Function of Shielding Depth for a Solar Flare of $P_0 = 50$ MV	16
5	Relative Primary and Secondary Radiation Dose as a Function of Shielding Depth for a Solar Flare of $P_0 = 100$ MV	17
6	Relative Primary and Secondary Radiation Dose as a Function of Shielding Depth for a Solar Flare of $P_0 = 195$ MV	18
7	Relative Primary and Secondary Radiation Dose as a Function of Shielding Depth for a Freden and White Van Allen Belt Proton Spectrum	19
8	Effective Dose (REM) = Rad Dose x RBE	20
9	Calculated Rad and REM Doses as a Function of Shield Thickness for a Typical Inner Van Allen Belt Spectrum	21
10	Gas-Wall Equivalent Test	31
11	Tissue-Equivalent Ionization Chamber Sensor and Preamplifier	32
12	Tissue-Equivalent Ionization Chamber Sphere and Barrel Assembly	33
13	Grid-to-Plate Transfer Characteristics for a Raytheon 8520 Logarithmic Electrometer Tube	34
14	Tissue-Equivalent Ionization Chamber Sensor, Preamplifier, and Amplifier	35
15	Ionization Chamber Power Supply	36
16	Temperature Sensor	37
17	Active Dosimeter Block Diagram	38

ILLUSTRATIONS (cont'd)

<u>Figure</u>		<u>Page</u>
18	Sensor and Barrel Assemblies	39
19	LET Detector and LET Detector Insert Final Flight System	44
20	Stopping Power as a Function of Proton Energy	45
21	LETs Block Diagram	46
22	Schematic Detectors and Preamplifiers	97
23	Schematic Signal Analyzer	98
24	Schematic Counter and Output	99
25	LET Ramp Output	47
26	Schematic of Power Supply	100
27	Active Dosimeter Module Mounting (Top View)	49
28	Active Dosimeter Module Mounting Sensor-Locking Assembly (Side Views)	49
29	Tissue-Equivalent Ionization Chamber Calibration Data	65
30	Americium-241, 5.476-MeV Alpha Particle Spectrum, Entrance Detector	66
31	Anticoincident Detector Sr-90 Spectrum	67
32	Complete Dosimeter Unit (Graphic Anatomy)	68
33	Passive Dosimeters Mounting Package	69
34	South Atlantic Anomaly Series of Revolutions	70
35	Active Dosimeter South Atlantic Anomaly Dose Rates	71
36	Active Dosimeter South Atlantic Anomaly Dose Rates	72
37	Active Dosimeter South Atlantic Anomaly Dose Rates	73
38	Active Dosimeter South Atlantic Anomaly Dose Rates	74
39	Active Dosimeter South Atlantic Anomaly Dose Rates	75
40	Active Dosimeter South Atlantic Anomaly Dose Rates	76

ILLUSTRATIONS (cont'd)

<u>Figure</u>		<u>Page</u>
41	Active Dosimeter South Atlantic Anomaly Dose Rates	77
42	Active Dosimeter South Atlantic Anomaly Dose Rates	78
43	Active Dosimeter South Atlantic Anomaly Dose Rates	79
44	Astronaut Radiation Survey in Skylab II	80
45	Command Module (Skylab II) Indicating Five Mounting Locations for D008 Radiation	81
46	Shielding Distributions for the Five Passive Units	82
47	Proton Integral Flux Energy Spectra	92
48	Proton Differential Flux Energy Spectra	93
49	Differential Proton Penetration Spectra	94
50	Proton Penetration Geometry	95

TABLES

<u>Table</u>		<u>Page</u>
1	ICRU Muscle Compound and Shonka Chemical Composition	25
2	Tissue-Equivalent Gas Composition	26
3	Skylab Passive Dosimeter Accumulated Dose Measurements	60
4	Thermoluminescent Mean Dose versus Spacecraft Location	61
5	Calcium Fluoride Dose Levels versus Spacecraft Location	61
6	Quartz-Fiber Ionization Chamber Dose Readings	62
7	Comparison of Passive Dosimeter TLD Measurements and Lockheed Space Shielding Code Theoretical Dose Computations	64
8	Omnidirectional Proton Flux (protons/cm ² sec) at B = 0.20 and L = 1.20 which Fall in Given Energy Ranges after Penetrating Shielding	88
9	Maximum Proton Energy Deposited in a Function of Angle of Incidence	90

SECTION I

INTRODUCTION AND BACKGROUND

Instrumentation to measure the radiobiologically significant high energy radiations encountered in manned spaceflight is of fundamental importance in ensuring astronaut safety and the ultimate mission success of these space programs. Since the discovery of high energy radiations in space, it has been recognized that manned operations in space would require a very careful consideration of these radiations. To date, manned space operations have not encountered dangerous radiation levels, either because of the absence of high energy solar particles, the avoidance of the areas of high fluxes of trapped particles in the earth's magnetosphere, and the relatively short duration of missions where high fluxes were encountered. However, on future long-term missions the reduction of radiation exposure may be more difficult, and a very comprehensive measurement of radiation levels must be made. This report describes an advanced active dosimetry system that will measure the important radiations encountered within a manned spacecraft.

The most significant radiations to be monitored in extended long-term missions, like the well-shielded NASA SKYLAB and the NASA/DOD Space Shuttle and Space Stations, are solar flare and Van Allen Belt protons with energies greater than about 30 MeV prior to passing through spacecraft shielding. The shielding is usually sufficient to eliminate the primary electron contribution, although bremsstrahlung and the highest energy electrons may contribute to the total exposure. These particles exist in a complex and often unpredictable array of fluxes and spectra. For manned operations the energy spectra and depositions of these particles must be measured at specific locations of astronaut operations.

The physical effects of these high energy corpuscular radiations can range from insignificant cellular damage to loss of life, depending on the magnitude and type of exposure. Numerous ground-based experiments show that the degree of radiation effectiveness in impairing the functions of biological systems is determined principally by the following two factors:

a. The locally absorbed radiation dosage: the absorbed dose is the quotient of dE divided by dm . dE is the energy imparted by ionizing radiation to matter in a volume element dm . The unit of absorbed dose is the rad, defined to be 100 ergs of absorbed energy per gram of absorbing material (ref. 1).

b. The locally delivered linear energy transfer (LET) spectrum of the absorbed radiations: the LET of charged particles in a medium is the quotient of dE divided by dL where dE is the average energy locally imparted to the medium by a charged particle of specified energy in traversing a distance of dL . LET is defined to include all of the delta rays (energetic secondary electrons) produced by the primary particle. The quantity (LET) is closely approximated by the stopping power for high-energy charged particles (ref. 2).

A number of the most important biological effects have been summarized in reference 3. It is noted that the range of effects given in reference 3 are very general and are formulated for uniform X and gamma radiations. In space, the proton and electron radiation spectra may vary considerably from one location to another and show wide differences, depending on the shielding configurations traversed (ref. 3).

The highly complex shielding afforded the astronauts by spacecraft and body self-shielding will cause the high-energy protons to degrade in a very nonuniform manner. This produces a significant depth-dose gradient in radiation-sensitive organs in the astronaut's body. The dose to each astronaut will also vary, depending on shielding locations frequented by him. Figure 1 (after ref. 4) shows a measured variation of depth dose with shielding in the earth's inner Van Allen Belt measured by the authors on the Gemini 4 spacecraft.

An idealized picture of the theoretical depth dose for the Van Allen Belt and a typical solar flare as a function of a number of critical organ depths is shown in figure 2 (after ref. 5). Such depth-dose gradients had not been measured for command module operations prior to this time. Adequate space-radiation dosimetry systems must be able to collect depth-dose measurements as well as measure surface dose and to conduct these measurements over short time periods to detect rapid large changes in the radiation field. For example, on the Gemini flights the authors observed a rise of three orders of magnitude in the radiation levels inside the spacecraft a few minutes after it entered the radiation belt.

The complex space-radiation spectra from Van Allen Belt, solar, and cosmic radiations when transmitted through highly inhomogeneous spacecraft shielding configurations result in even more complex spectra consisting of degraded primary protons, secondary protons, and neutron emissions. The differential and integral energy spectra anticipated inside the Apollo spacecraft and passively measured in the Gemini spacecraft shielding structures are shown in figure 3.

The secondary radiations appearing inside of the spacecraft will become more appreciable as the depth of spacecraft shielding is increased. A 500-MeV proton has a range of 148 gm/cm² in aluminum and a probability of nuclear interaction of 76 percent. For a 400-MeV proton the range is approximately 104 gm/cm² which leads to a probability of nuclear interaction of 65 percent. As the range of the proton drops to about 10 gm/cm² for a 100-MeV proton, the probability of a nuclear interaction is reduced to 16 percent. Figures 4 through 7 are computations from radiation transport and shielding codes that show the relative importance of secondary radiations compared to primary radiations as a function of depth of material for several exterior radiation spectra for the radiation belts and solar flares (ref. 6). For the Van Allen Belt it is predicted that at a depth of 20 gm/cm² of shielding, the secondary particles produce 22 percent of the interior radiation dose. At 50 gm/cm² of shielding the secondary contribution to the interior radiation dose is 40 percent. The secondary radiations are of additional concern because they consist of a large number of low-energy radiations whose LET spectrum is skewed to higher values, increasing relative biological effectiveness of radiation dose as shielding is increased. Therefore, as increased shielding reduces the overall radiation dose received by an astronaut, the increased production of low-energy secondaries raises the biological effectiveness of the radiations. This concept is discussed later in this section.

The calculations presented in figures 4 through 7 are idealized because uniform shielding distributions are employed. In the realistic case, as in the Skylab Command Module, thousands of small solid angles are present whose radial shielding varies from a few gm/cm² to hundreds of gm/cm² of different materials. Incomplete knowledge of secondary radiation production cross sections and difficulties in obtaining exact external spectral maps of the entire operating range of the space radiation environment make calculations

somewhat uncertain in predicting long-term exposures. As a result, one of the major objectives of the instrumentation described here was to test and refine computational techniques of dose and particle spectra inside a realistic shielding configuration.

Figure 8 indicates how the radiation dose is modified for radiations of different linear energy transfer. The variation of radiation quality factor with LET values for mammalian tissues and crystalline lens cellular destruction and division are shown. For comparative purposes the recommended radiation protection values of relative biological effectiveness (RBE) as a function of LET, defined by the National Radiation Protection Subcommittee, M-4 (ref. 7), are also shown. It is observed that there are wide variations in the RBE values for different radiation effects. For mammalian tissue damage, the RBE is constant at a value of 1.0 for LET values of 3.5 keV/micron and less. The experimental RBE curves show a nonlinear rise to values of up to 5.0 for a LET of 100 keV/micron. Beyond LET values of 90 keV/micron the RBE values decline in a nonlinear fashion.

For mixed fields of corpuscular radiations such as exist in the earth's radiation belts, in solar flares, and in galactic cosmic radiations, a wide spectrum of LET values may exist at various depths. The LET spectra must be measured and combined with the radiation doses and depth doses to give the effective or REM dose.* The problem in its most fundamental form reduces to one of determining the fraction of the dose (energy) delivered in each energy interval at the shielding depth of interest.

The LET spectrum behind spacecraft shielding causes higher RBE values with increased shielding. The effect of increased shielding on LET is indicated in figure 9 (after ref. 6), which shows that the Rem dose increases to a factor of two over the rad dose at less than 50 gm/cm² of shielding. This is due to the presence of a wide variety of lower energy radiations, mostly secondary and degraded primary protons and secondary neutrons. It is important that the LET spectrum be determined where more than a first estimate of dose is required.

An adequate dosimetry system must be capable of providing the following minimum measurements of the radiation field inside of the spacecraft: (1) the astronaut whole-body average surface (skin) dose levels; (2) the depth-dose

*REM dose = RBE x rad dose where RBE is obtained from RBE versus LET tables.

gradient at critical astronaut body organs (gastrointestinal tract, blood-forming organs, etc.); (3) the dose as a function of differently shielded spacecraft locations where the astronaut may be operating; (4) the instantaneous dose rates and depth-dose rates delivered to the astronaut where dose rates are high; (5) the accumulated doses and depth doses as the spacecraft shielding and body self-shielding locations previously mentioned; and (6) the LET spectra at the same locations, where possible.

Not only must an idealized dosimeter system provide these measurements, but it must also meet the criteria of small weight and size, be space-qualified, and have portable sensor elements. The systems must also have a wide radiation-response range and excellent long-term accuracy. The radiation levels should further be determined where possible in a test material that has radiation reaction properties that closely match human muscle tissue, i.e., the instrumentation must be able to measure the tissue-equivalent dose levels from mixed radiation fields over a wide range of energies. The active and passive dosimetry systems described in the following sections of this report fulfill very closely the above criteria in an accurate, reliable, and inexpensive manner within state-of-the-art radiation-detection methods.

The active dosimeter system contains one tissue-equivalent ionization sensor equipped for portable as well as stationary operation combined in close proximity with a low-energy charged particle spectrometer to measure LET spectra. With this instrument the astronaut can measure the dose, depth dose, and LET simultaneously and instantaneously inside a manned spacecraft. The radiation measurements are processed automatically by signal-conditioning electronic systems for transmission by spacecraft telemetry. The electrical and mechanical design of each subsystem is discussed in detail in the following sections.

The passive dosimetry system is used to supplement the active dosimetry by providing a record of the total dose using thermoluminescent devices and discharge ionization chambers. Film emulsions and heavy-particle sensors record the LET spectra for very high LET particles and provide a similar record of the Rem doses for the mission. The film emulsion data are particularly valuable for very low energy particles and higher atomic number particles which are very difficult to measure actively. Activation foils are included to provide

details of the neutron contributions to dose from natural secondary particles and possible artificial sources.

Mission data and results from Skylab II are presented for both the active and passive dosimeters in section VI.

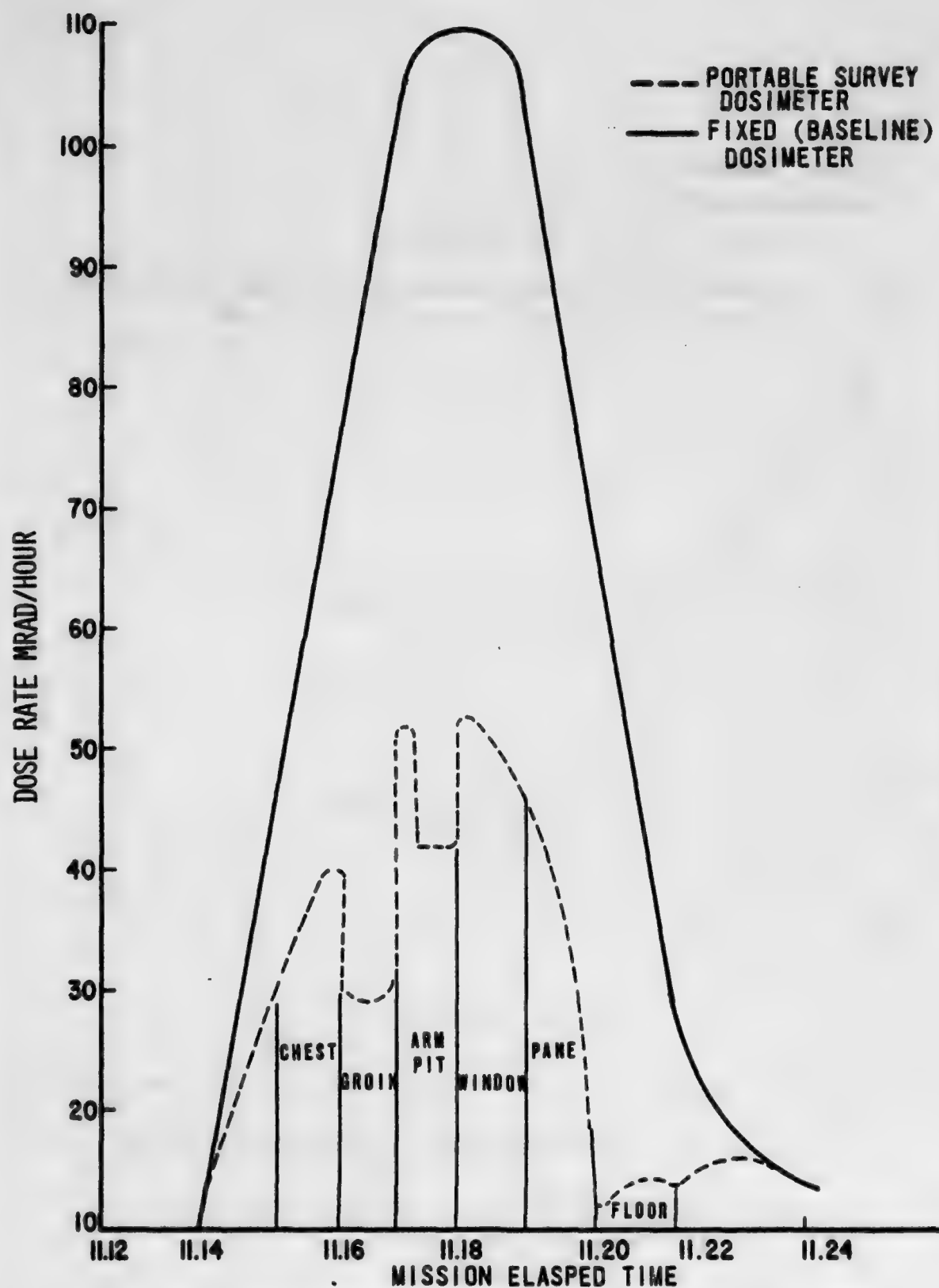


Figure 1. Radiation Shielding Variations for Gemini Spacecraft

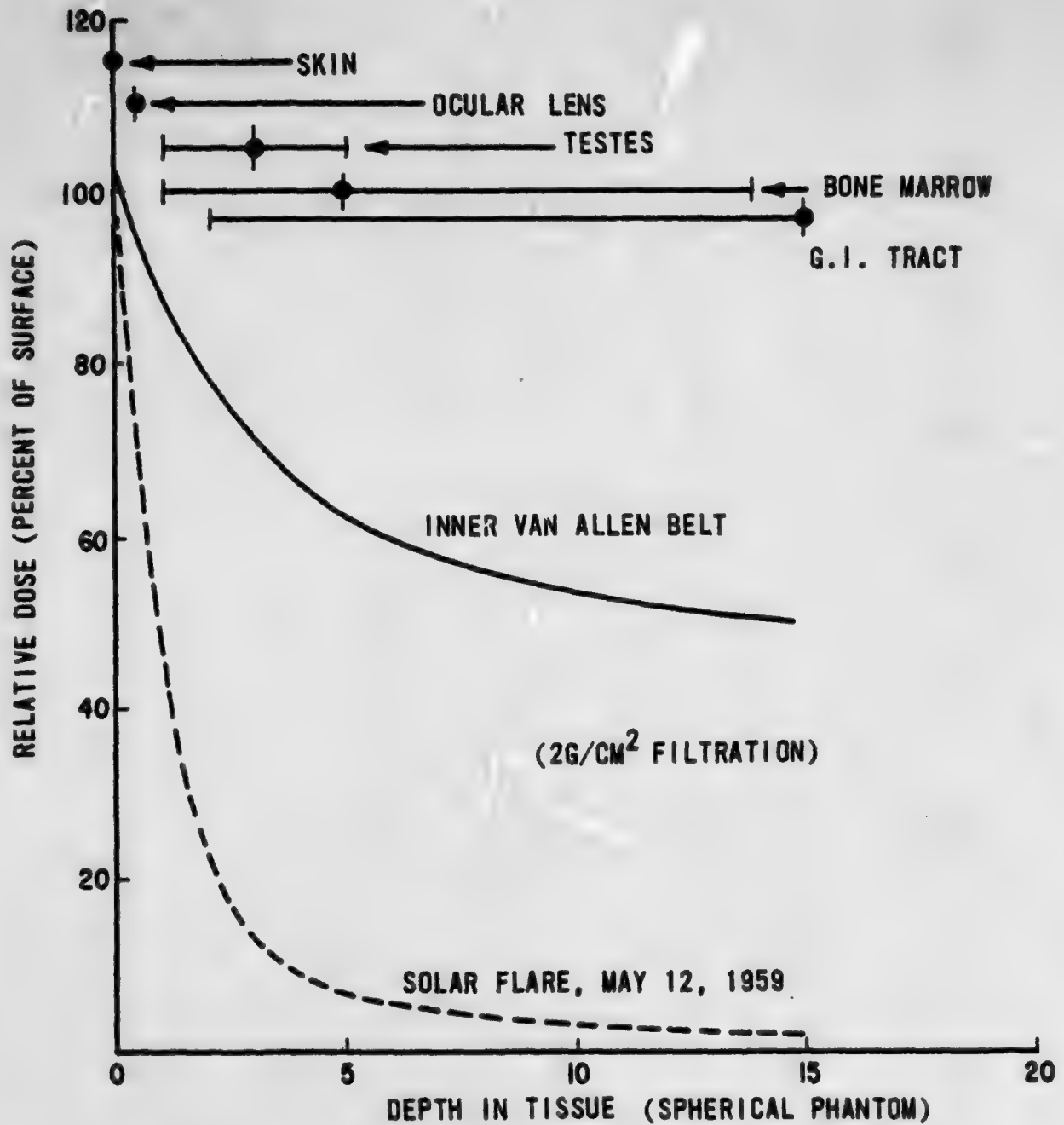
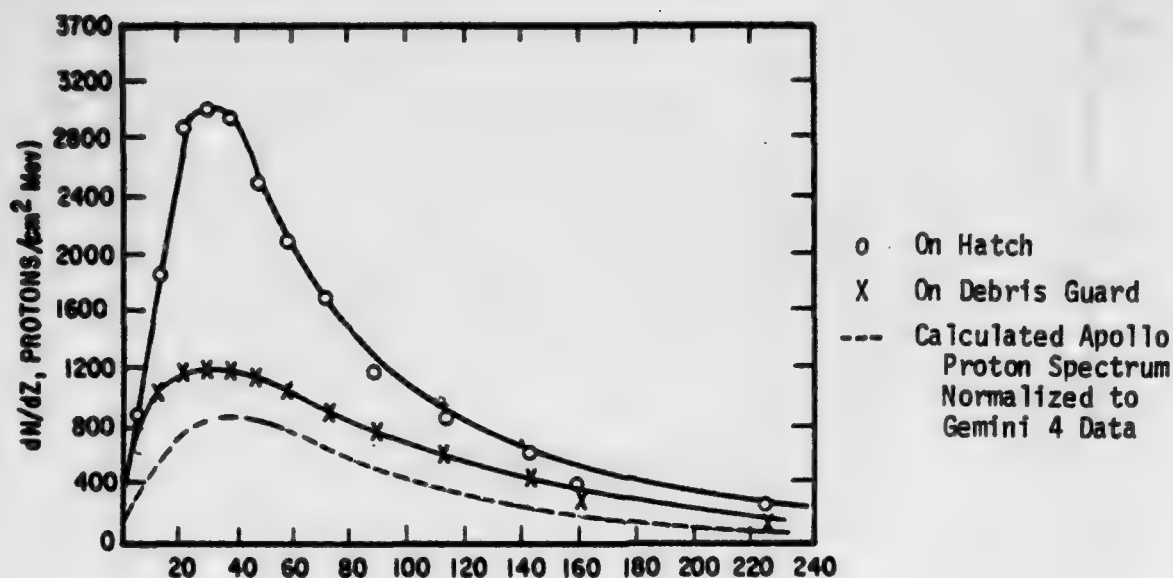
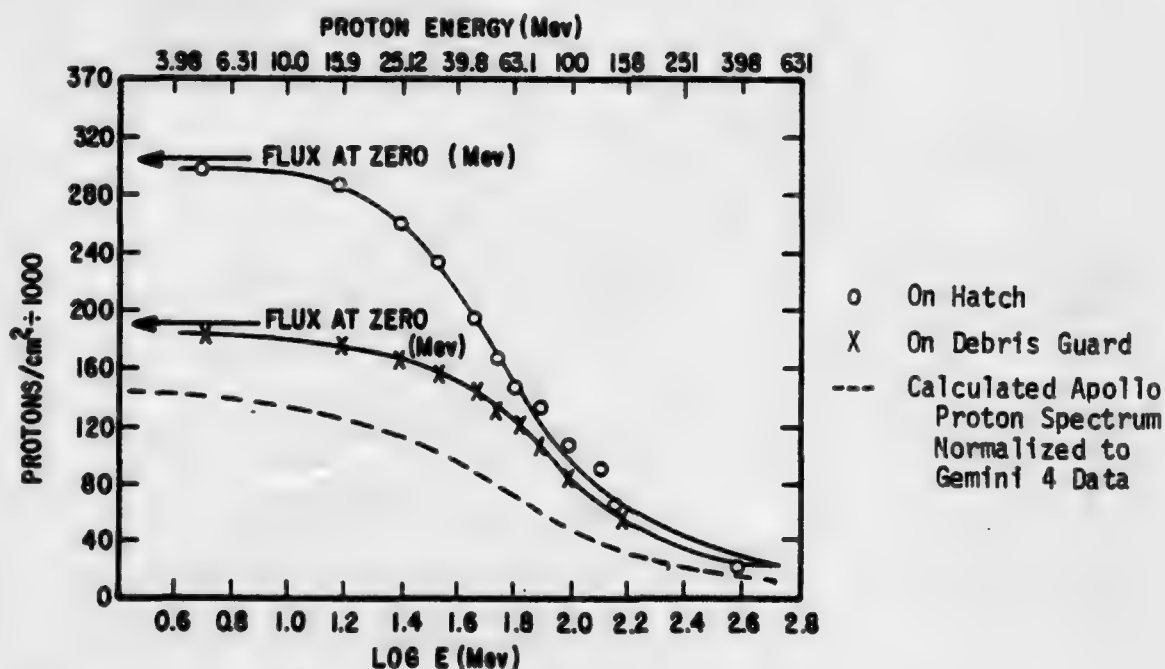


Figure 2. Theoretical Depth-Dose Distribution for Critical Organs in Space Radiations



(a) Gemini 4 Differential Proton Spectra



(b) Gemini 4 Integral Proton Spectra

Figure 3. Differential and Integral Proton Spectra Integrated over Gemini 4 Mission Duration and Predicted Apollo Integral Proton Spectrum

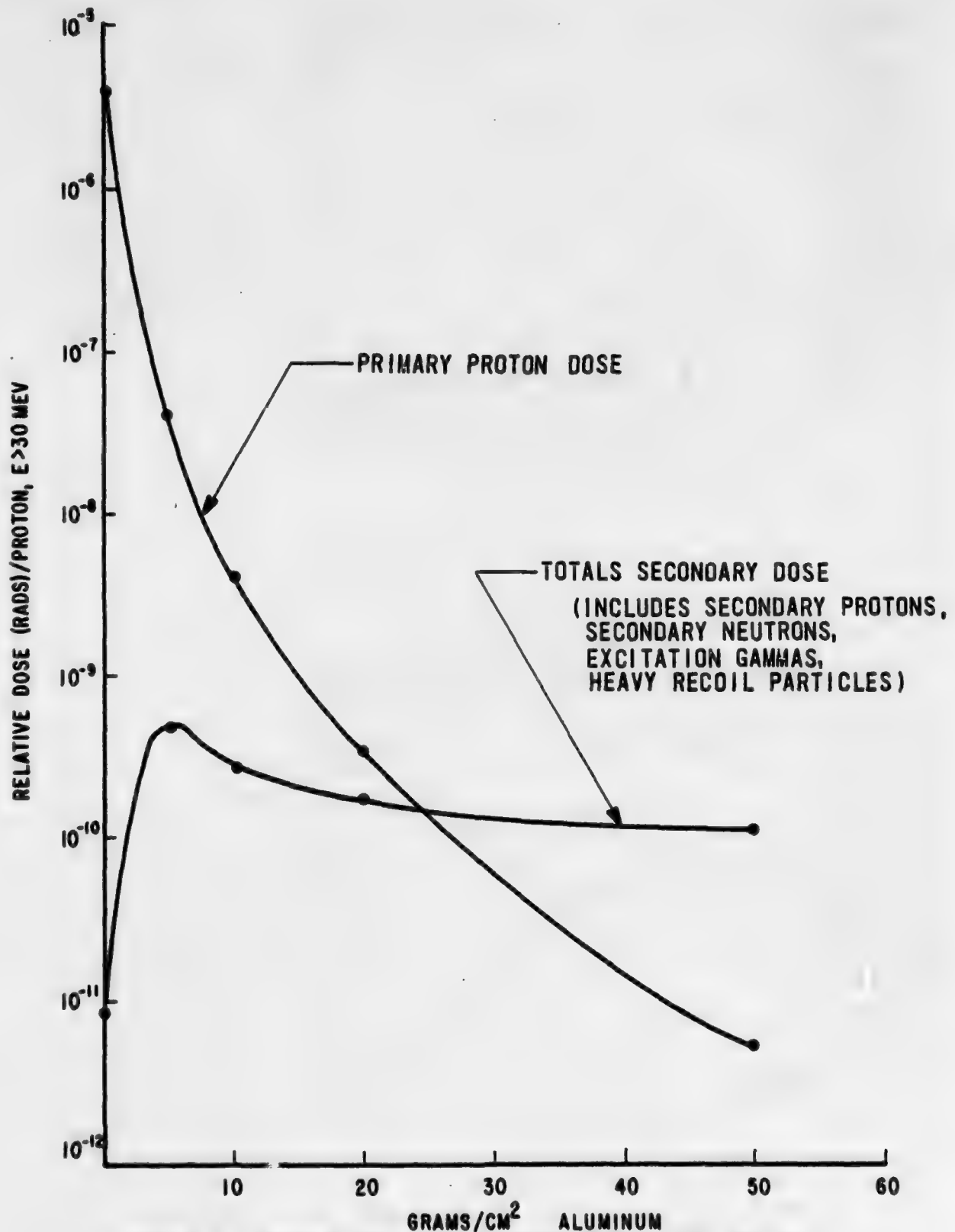


Figure 4. Relative Primary and Secondary Radiation Dose as a Function of Shielding Depth for a Solar Flare of $P_0 = 50$ MV

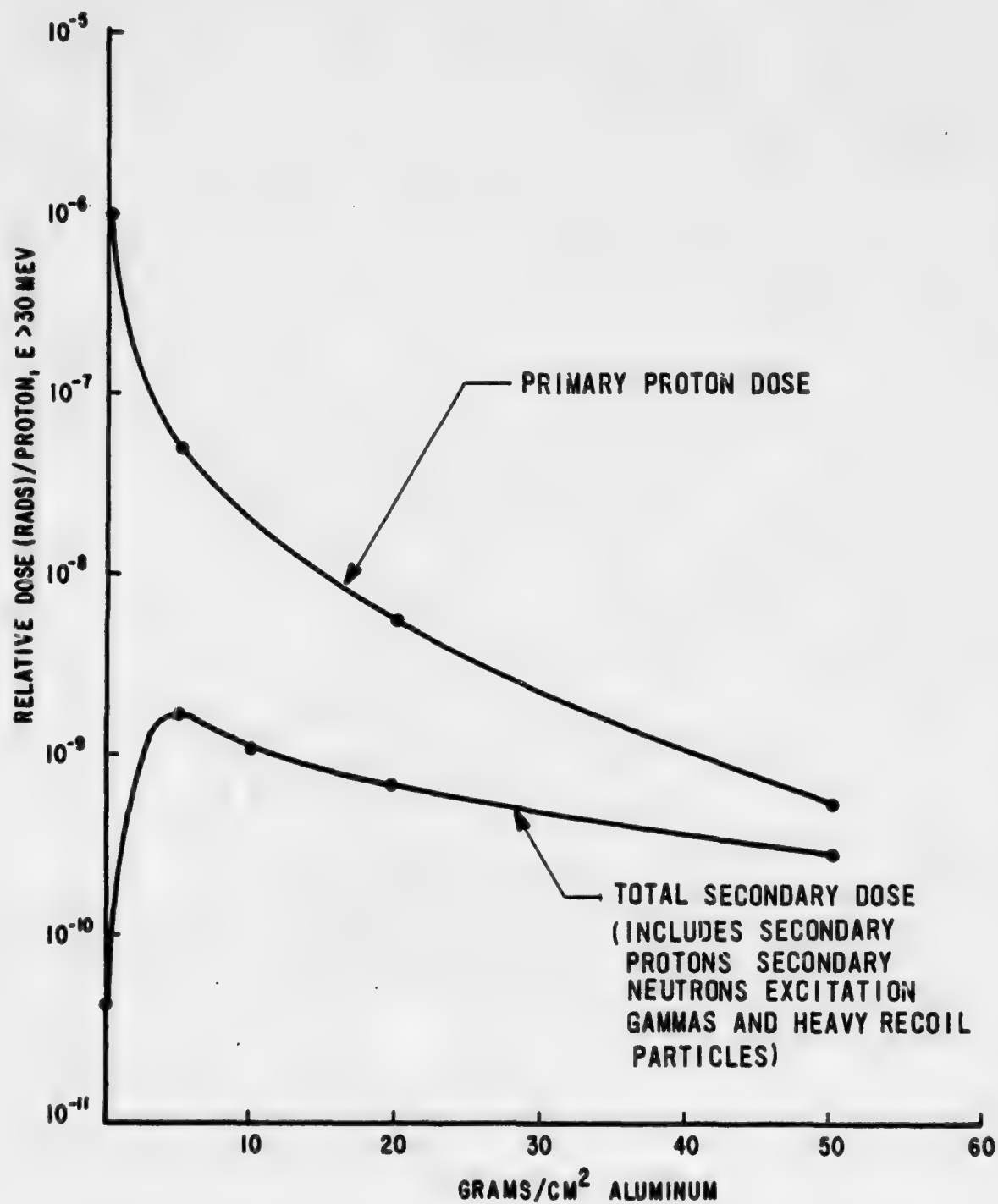


Figure 5. Relative Primary and Secondary Radiation Dose as a Function of Shielding Depth for a Solar Flare of $P_0 = 100$ MV

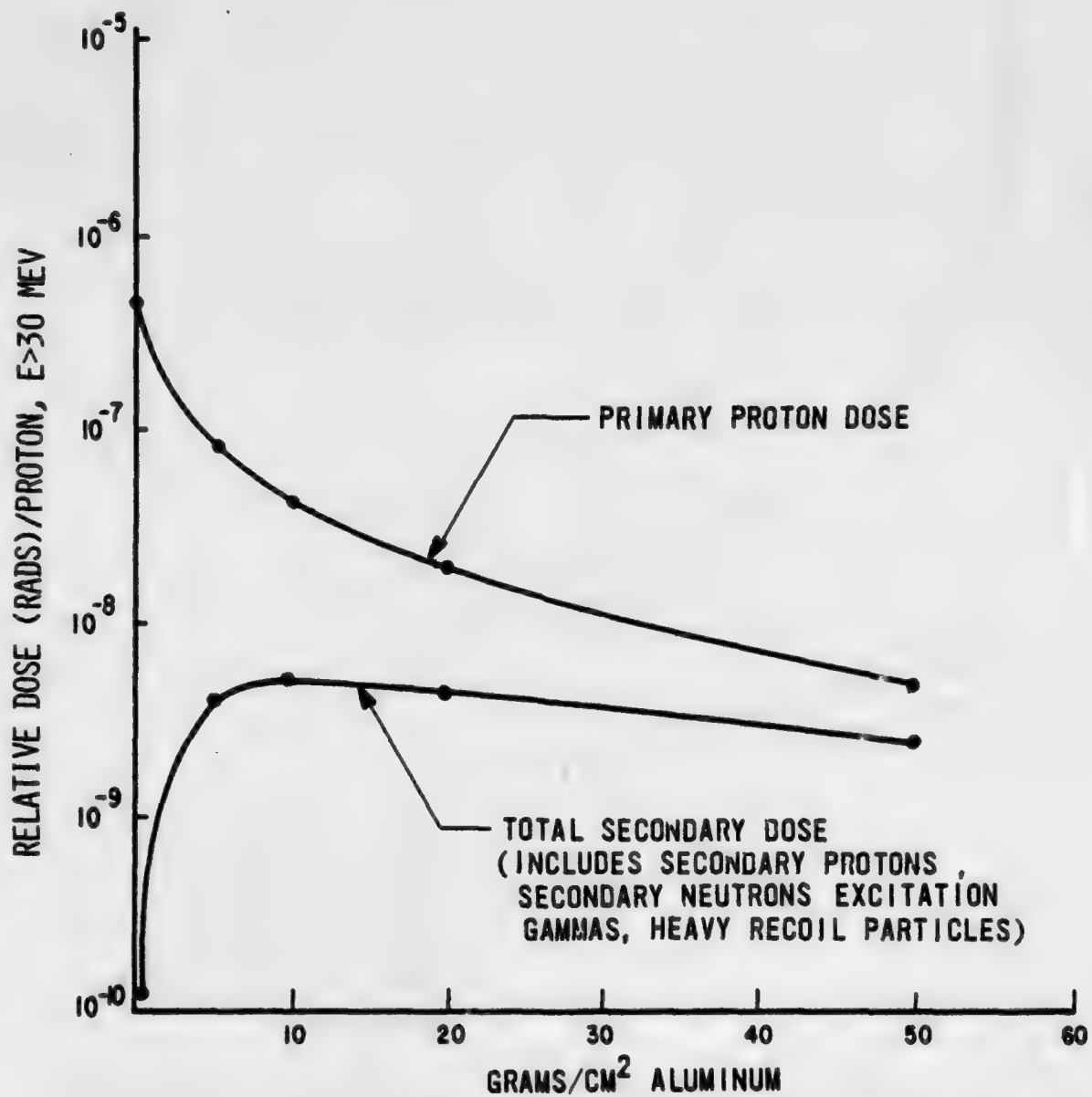


Figure 6. Relative Primary and Secondary Radiation Dose as a Function of Shielding Depth for a Solar Flare of $P_0 = 195$ MV

ALL SECONDARY DOSES INCLUDE:
 SECONDARY PROTONS SECONDARY NEUTRONS
 EXCITATION GAMMAS AND HEAVY RECOIL
 PARTICLES

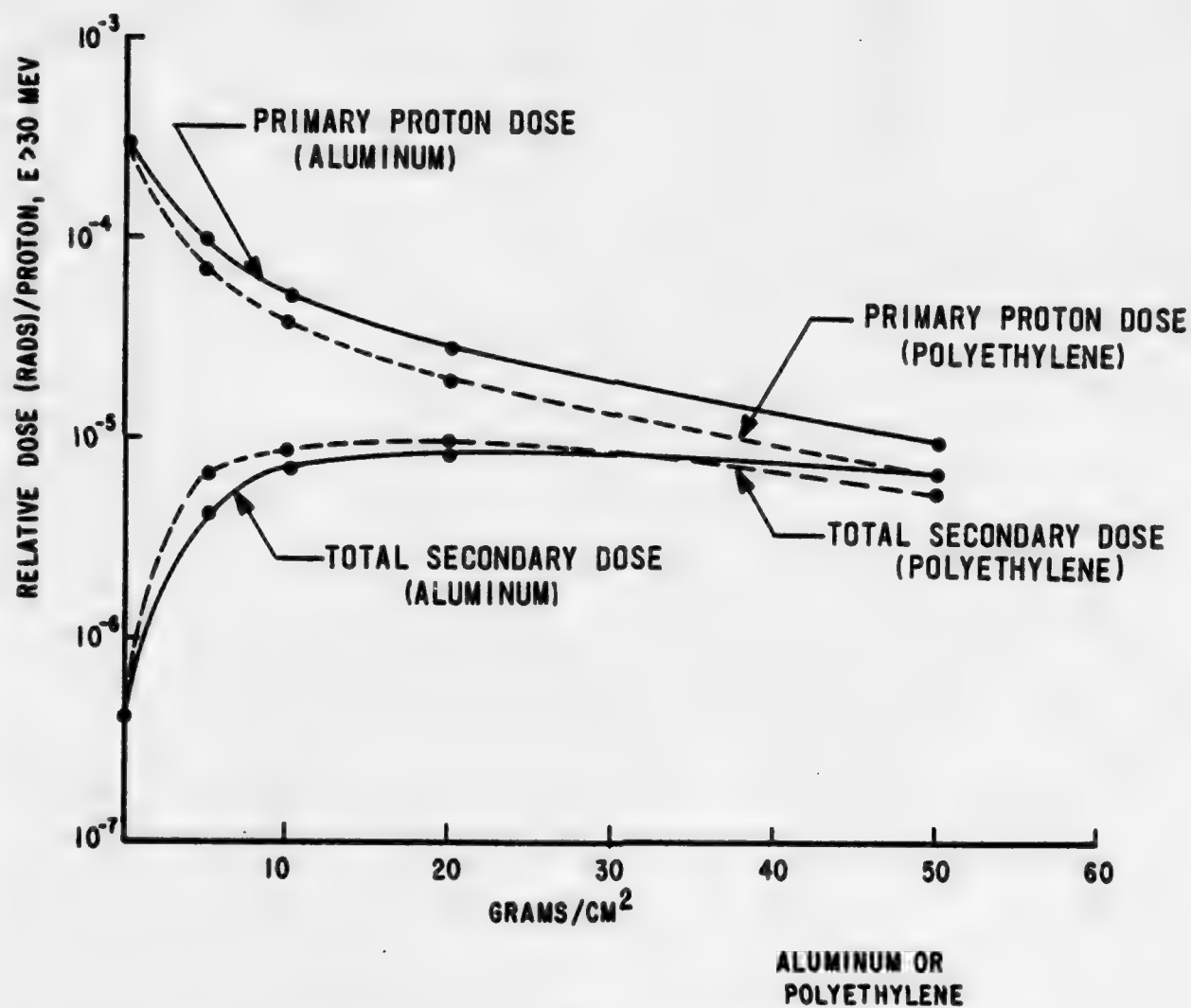


Figure 7. Relative Primary and Secondary Radiation Dose as a Function of Shielding Depth for a Freden and White Van Allen Belt Proton Spectrum

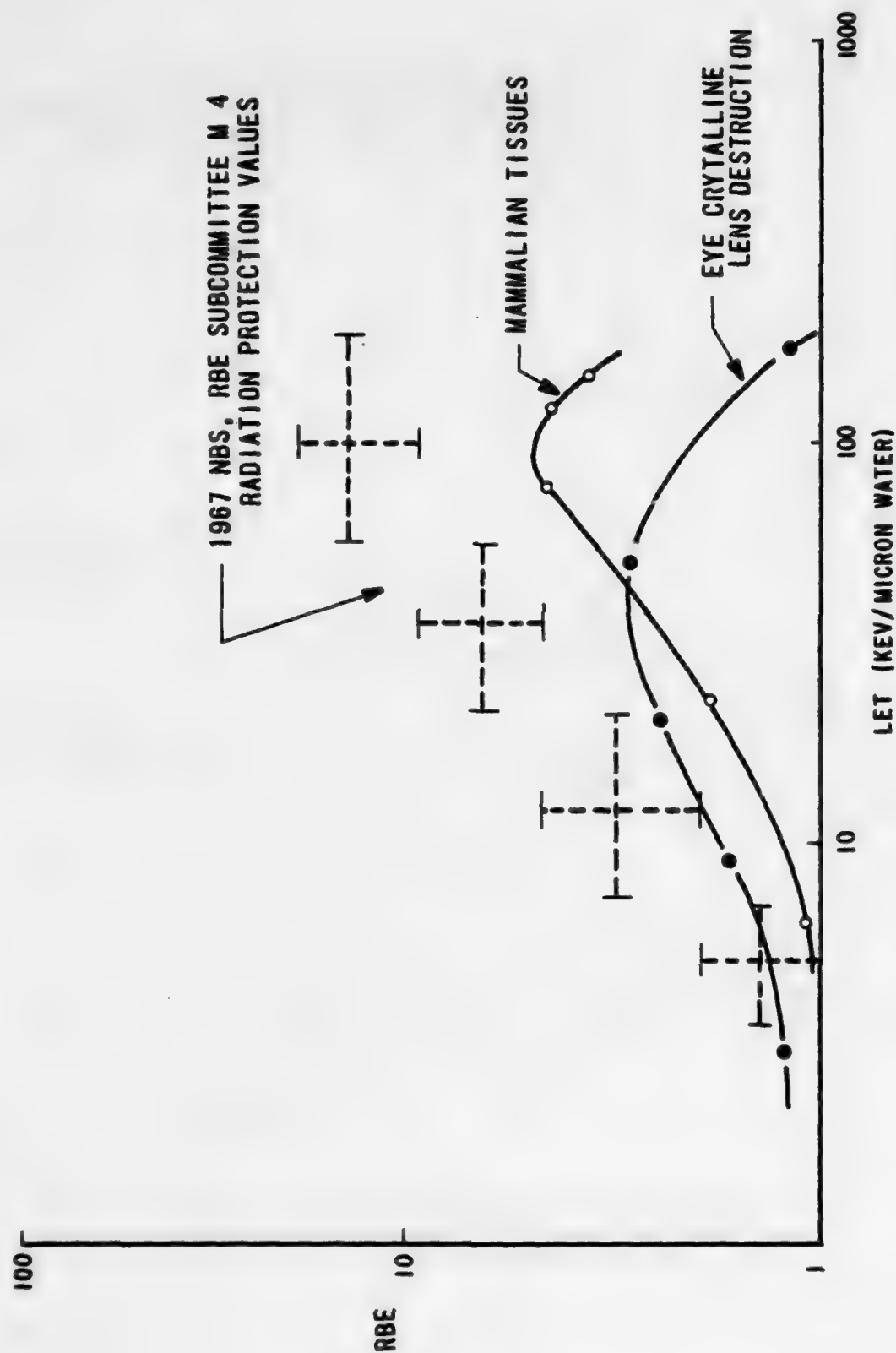


Figure 8. Effective Dose (REM) = Rad Dose x RBE

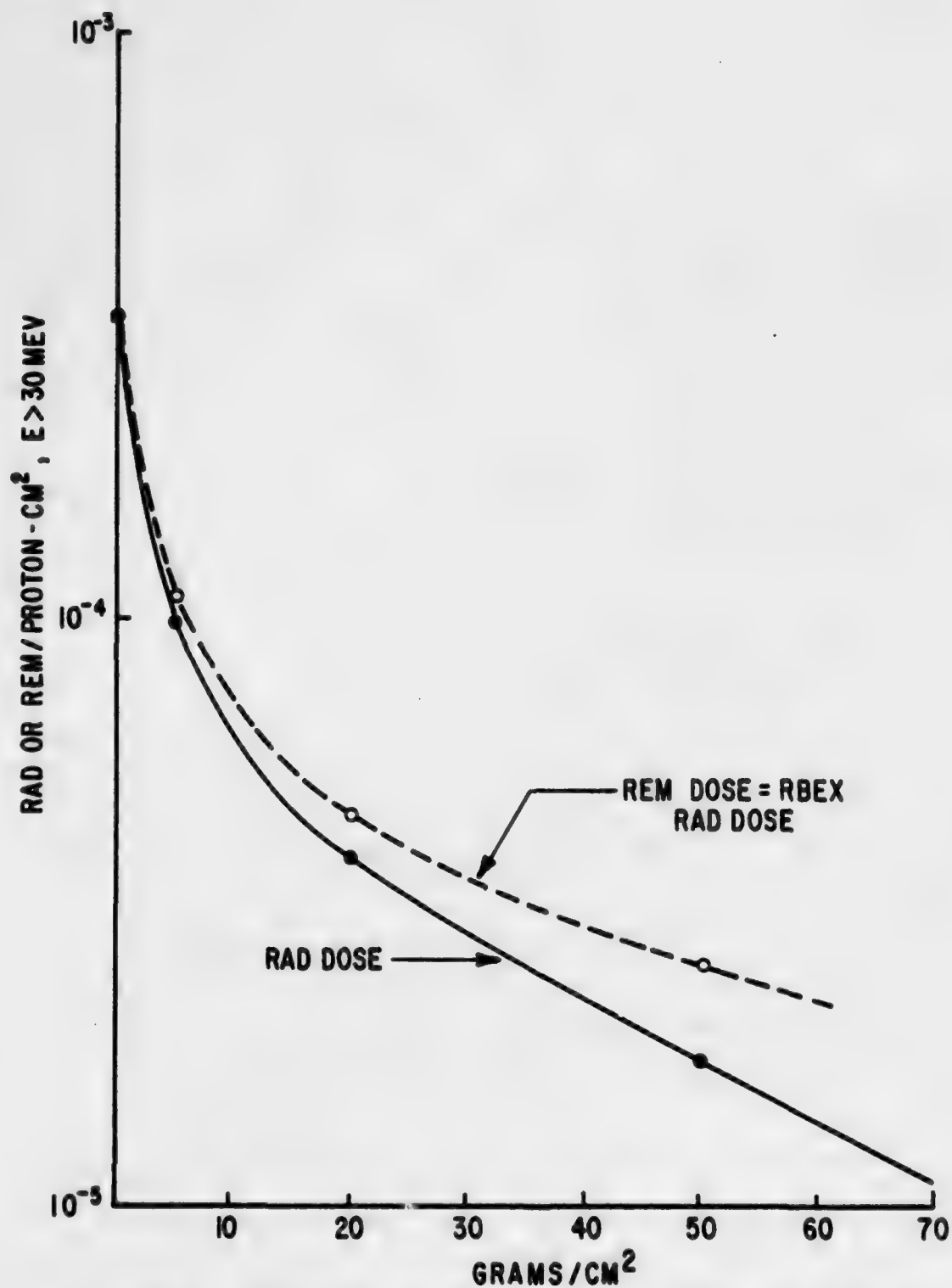


Figure 9. Calculated Rad and REM Doses as a Function of Shield Thickness for a Typical Inner Van Allen Belt Spectrum

SECTION II

ACTIVE DOSIMETER DESIGN

1. IONIZATION CHAMBER SENSOR THEORY AND PHYSICAL DESIGN

The active dosimeter described in this report involves the use of ionization chambers designed primarily on the Bragg-Gray principle. This principle relates the ionization of a gas in a cavity contained in a medium to the absorbed dose in that medium. This concept is described in detail in various radiation dosimetry texts such as reference 8.

The ionization chamber is a high sensitivity detector consisting of a charge-collecting electrode in a gas-filled cavity surrounded by a conducting wall. Radiation traversing the gas generates ion pairs which are collected by the internal electrode, and the current is recorded by means of an amplifier. A properly designed tissue-equivalent ionization chamber correctly records the energy deposited within the gas-filled cavity from all types of ionizing radiation as if the recording sensor were muscle tissue.

The simplest form of cavity ionization theory is the Bragg-Gray treatment with the modifications of Spencer and Attix (ref. 9). These basic principles are applicable to both neutral and charged incident radiation. There are three fundamental assumptions which are applicable in the case of incident charged particles.

a. A charged particle deposits energy in a continuous manner as a function of the medium, the type of charged particle, and its energy. The amount of energy imparted is assumed to be described adequately by the stopping power.

b. The charged particle flux does not change in traversing an infinitesimal cavity.

c. The energy lost per unit path length does not change over a very short path length.

If these three assumptions are satisfied, the energy per unit mass (dose) absorbed in the cavity is related to the energy per unit mass in the surrounding medium by the ratio of the gas and chamber wall mass stopping powers. By measuring the number of ion pairs created in the cavity gas, the dose delivered

to the surrounding medium is obtainable, assuming that the energy required to form an ion pair in the gas is known and is independent of particle type and energy. However, it has been shown that the energy required to form an ion pair does depend to some extent on the particle linear energy transfer (LET), which is a function of the particle type and energy. Particles for which this poses a problem include neutrons and very heavily charged particles ($Z > 3$). It is, however, usually not important for protons above 1 MeV and for all photons and electrons.

Even if the energy required to form an ion pair was LET independent, two additional restrictions commonly known as the Bragg-Gray criteria would still be imposed on the measuring device. For charged particles, these criteria state that

- a. The cavity must be sufficiently small so that the primary particle does not stop in the cavity.
- b. The cavity must be sufficiently large that the range of secondary particles (such as delta rays) is short with respect to the cavity.

If the gas and the surrounding medium are of identical atomic composition, the cavity may be large without disturbing the flux of secondary particles, i.e., it has been shown that in a medium exposed to a uniform flux of primary radiation, the flux of secondary radiation is also uniform and independent of both the density of the medium and density variations from point to point. The cavity ionization principle, therefore, permits a determination of energy absorption in a solid medium from the measured ionization in a gas-filled cavity.

When a primary flux of photons is considered instead of charged particles, further conditions must be imposed. Gamma rays impart energy only through electron interactions,* so the walls must be thick enough that secondary electron equilibrium exists.

The concept of tissue-equivalency is important in dosimetry because the biological damage due to radiation fields must be specified in terms of the rate of energy deposition in tissue. Ideally, this means that the filling gas

*For purposes of dosimetry, this statement can be considered to be rigorously correct, although there are some extremely improbable gamma-nucleus interactions.

and the material of the ionization chamber walls have the atomic composition of human muscle tissue. The minimum practical criterion is that the wall material has interaction cross sections and stopping powers very closely matched to standard muscle tissue for all radiation types. Corrections can be made in the readings obtained by nontissue-equivalent dosimeters for incorrect responses to radiations that are present at the point of dose measurement for monoenergetic beams of particles. However, for mixed fields of protons, heavy particles, electrons, and photons the task of obtaining these corrections is formidable. If this is to be done, the spectrum of particles causing the dose must be accurately known at the point of measurement, and this requires extremely sophisticated spectrometry hardware located at the dose point, each time an energy deposition (dose) measurement is made.

Tissue-equivalent ionization chambers which record the dose from photons and neutrons must meet both the Bragg-Gray assumptions and criteria. Incident photons and neutrons produce secondary particles in the chamber walls which then enter the filling gas causing ionization. The great majority of the secondaries which eventually produce ion pairs within the filling gas actually originate within the chamber walls, not within the filling gas. The concept of the gas-wall secondary particle equilibrium is essential to the proper measurement of photons and neutrons using ionization chambers.

The dosimetry of protons, alphas, and other heavy charged particles does depend on the Bragg-Gray assumptions but not rigorously on the Bragg-Gray criteria. In this case, the overwhelming majority of the ion pairs formed in the filling gas are created by the primary heavy charged particle itself, not by secondary electrons formed in the walls. For this reason, it is quite important that the filling gas be tissue equivalent. This is very different from the photon and neutron case where the tissue equivalency of the wall is much more significant than the filling gas.

Shonka (ref. 10) has developed a series of plastic resins that are ideally suited for this purpose. These are the plastics that are used in the Skylab ionization chamber sensors. To compare the tissue equivalency of various compounds to Shonka plastic, the standard composition as defined by the International Committee on Radiological Units (ICRU) (ref. 11) presented in table 1 was employed. For comparison, the various percentages by weight of the Shonka material are also presented.

Table 1

ICRU MUSCLE COMPOUND AND SHONKA CHEMICAL COMPOSITION

<u>Element</u>	<u>Atomic number</u>	<u>ICRU muscle percent by weight</u>	<u>Shonka plastic percent by weight</u>
H	1	10.20	10.25
C	6	12.30	76.05
N	7	3.50	3.50
O	8	72.90	5.19
Na	11	0.08	0.08
Mg	12	0.02	0.02
P	15	0.20	0.20
S	16	0.50	0.50
K	19	0.30	0.30
Ca	20	0.007	0.007

By comparing the total gamma- and X-radiation absorption coefficients (cross sections) for each of the elements contained in Shonka plastic to the total gamma- and X-radiation absorption coefficients for ICRU muscle, it is found (ref. 12) that the two compounds have the same response to within 12 percent for all energies between 0.01 and 10 MeV; the two compounds respond to within 0.25 percent for gamma-radiation energies between 0.1 and 4.0 MeV. A comparison of the mass stopping powers for Shonka plastic to ICRU muscle for electrons in the energy range 0.01 to 20 MeV shows that the two compounds have the same response to within 2.6 percent. For protons, Shonka plastic and ICRU muscle are within 5 percent for energies from 0.1 to 10 MeV. The choice of Shonka plastic as a sensor wall material then allows for more accurate measurement of the tissue dose than would be realized by the use of metals such as aluminum or stainless steel which are often used as ionization chamber wall materials and provide, at best, extrapolations to the true tissue dose in mixed-field dosimetry.* To avoid the necessity for making energy-dependent

*Even though a very thin aluminum shell (discussed later in this report) is employed to protect the sensor wall, it is the inner Shonka plastic wall and the sensor gas that determine the radiation response characteristics.

corrections to the dose, the dose is measured directly in the dosimetry system by using Shonka sensor material previously described. This allows the tissue dose to be measured directly in all fields of interest. It was previously stated that to have an ionization chamber cavity of reasonably large volume capable of measuring the dose in a tissue-equivalent medium, the Bragg-Gray theory requires the gas should be matched atomically to this medium. A suitable nonexplosive tissue-equivalent gas comprising methane, carbon dioxide, and nitrogen in the proportions shown in table 2 is employed inside the chamber.

Table 2
TISSUE-EQUIVALENT GAS COMPOSITION

<u>Element</u>	<u>Composition by weight (percent)</u>
C	45.6
O	40.8
H	10.1
N	3.5

Observations of the gamma and neutron sensitivity of a tissue-equivalent ionization chamber (TEIC) using this filling gas have indicated that it is stable to ± 2 percent over a 6-month period; thus, demonstrating that negligible changes in the filling gas occur through diffusion or absorption losses in the cavity wall during the period of measurement.

Experiments at the Oak Ridge cyclotron showed that dosimetry of energetic proton beams depends primarily on the stopping power of the collection gas and on the composition of the wall material. This finding assures that accurate ground calibration of dosimeters using cobalt-60/cesium-137 gamma sources can be performed for a space measurement of dose in protons if the gamma absorption coefficients of the wall material and the proton stopping powers of the gas are both well matched to their respective values for standard muscle tissue. Since a tissue-equivalent gas and wall material are both used in these sensors, they measure energy-independent tissue-absorbed dose from the main component of space radiation--high energy protons--as well as the dose from any other lesser components of the radiation field such as electrons, and bremsstrahlung.

An extrapolation experiment was also performed to test the equivalency between the mass absorption of the cavity walls and that of the filling gas. The cavity gas pressure in the active dosimeter sensor was reduced by fixed increments and extrapolated to zero pressure. It was shown that the ionization per unit mass of gas was a constant regardless of gas pressure. X-rays of half value layers of 2.0 mm of aluminum were used in the experiments. The results are shown in figure 10.

2. IONIZATION CHAMBER ELECTRONIC DESIGN

It was demonstrated in the previous section of this report that the dose rate is directly proportional to the ionization current produced in the ionization chamber cavity gas. This current is collected and conditioned by the following electrical subsystems which complete tissue-equivalent ionization chamber system. These systems were manufactured in a flight-ready configuration by the AVCO Electronics Division/Tulsa.

- a. Sensor and Preamplifier
- b. Operational (Signal Conditioning) Amplifier
- c. Power Supply
- d. Temperature Monitor

Each of these major subsystems is discussed in detail in the following sections.

a. Ionization Chamber Sensor and Preamplifier Subassembly

The ionization chamber sensor and preamplifier subsystem is displayed in figure 11. The sensor consists of two electrodes. One is an 0.0625-inch thick Shonka Type A-150 tissue-equivalent plastic sphere with an outer diameter of 2.31 inches. This sphere acts as the high-voltage electrode for the ionization chamber system. The other ionization collecting electrode is a thin cylindrical probe 0.05 inch in diameter and 0.747 inch long centered within the spherical outer electrode. These are displayed in figure 12. This electrode is also constructed of Shonka plastic. The collecting electrode is connected directly to the grid of a Raytheon CK 8520 electrometer. The CK 8520 preamplifier used to collect and amplify the instantaneous ionization current formed in the tissue-equivalent cavity operates in the triode-connected floating grid mode. This operation is called floating grid position because the grid is operating without a grid resistor at approximately zero volts with respect to the cathode. For an optimum filament current of 10 milliamperes

at 1.50 volts and a plate voltage of 6.5 volts, the relationship between the plate and grid currents for an 8520 electrometer has the following form:

$$i_p = (4.43 \log_{10} i_g + 94.5)^{3/2}$$

where

i_p = the plate current

i_g = the grid current

Figure 13 displays a plot of the 8520 electrometer plate current as a function of the grid current. This system can be used to measure radiation-induced currents from 10^{-14} amperes to over 10^{-7} amperes. This wide range of current values allows for the measurement of various levels of ionization found from cosmic rays, solar flare particles, or the trapped Van Allen particles that might be encountered on manned space missions.

b. Ionization Chamber Signal Conditioning Amplifier

The signal conditioning amplifier is displayed connected with the sensor and preamplifier in figure 14 and has been designed for this use by AVC0/Tulsa. The signal conditioning amplifier subsystem changes the CK 8520 electrometer plate current (typically a few hundred microamperes) to a 0.0- to 5.0-volt dc level compatible with spacecraft telemetry. The signal conditioning amplifier is a Fairchild SN52709 high-gain operational amplifier constructed on a single silicon chip using special planar epitaxial processes. It features high input impedance, low offset, large input common mode range, and high output swing under load. The system is a low power device drawing less than 300 milliwatts maximum power and less than 150 milliwatts as operated in the tissue-equivalent ionization chamber system. Additionally, the operational amplifier is highly stable with temperature over the range -55°C to 125°C as a result of excellent internal temperature compensation.

The signal conditioning subsystem is designed with both gain and bias adjustments. These adjustments are used to set the dc level and slope of the input current versus output voltage curves before final calibration of the instrument. For example, for operations in very low level radiation environments the gain would be set at its maximum value with a minimum slope setting for the bias to obtain maximum low level radiation response sensitivity. Gain

adjustment is obtained by variable resistor R3 between the negative side of the filament and ground of the operational amplifier. The gain adjustment has the effect of raising or lowering the amplification factor of the CK 8520 electrometer. Bias adjustment is accomplished by varying resistor R4 between operational amplifier output and ground.

c. Ionization Chamber Power Supply Assembly

The electronic conversion unit (power supply) subsystem shown in figure 15 is a standard dc-to-dc converter with series input regulation and hard diode protection. The dc-to-dc converter supplies high voltage for the ionization chamber. The power supply system operates from an unregulated input power source in the range of 28^{+4}_{-8} volts dc. The input is diode-protected against a maximum of 300 volts of inadvertently applied reverse polarity voltage.

d. Ionization Chamber Temperature Sensor Assembly

The ionization chamber is equipped with a temperature sensor subsystem consisting of a transistor whose variation of beta with temperature is measured. This system is shown in figure 16. The temperature variation is achieved by transistor Q1 which provides the desired operating range (-40°F to $+160^{\circ}\text{F}$) for the temperature sensor.

A block diagram of the ionization chamber electronics is displayed in figure 17.

3. IONIZATION CHAMBER MECHANICAL DESIGN

The ionization chamber sensor is constructed of three walls. The inner, tissue-equivalent Shonka plastic, 2.31-inch diameter sphere is covered with a second layer of 0.0625-inch thick epoxy to electrically isolate the inner conductive sphere from the third or outer wall. The outer wall is the hermetic seal for the two inner walls. It consists of a 0.025 ± 0.005 -inch thick aluminum sphere. These three concentric spheres are attached to a cylindrical (also triple walled) barrel assembly housing the inner collecting electrode and the Raytheon CK 8520 preamplifier electrometer. The outer aluminum housing for the cylindrical barrel is itself cylindrical and machined in a single assembly with one of the hemispheres of the sensor. This assembly is hermetically sealed by a combined press fit design secured with epoxy at the major diameters of the sensor hemispheres. The sensor and barrel assemblies are displayed in figure 18.

More details on the portability of this sensor and its interconnection with the parent active dosimeter are given in a later section of this document.

IONIZATION CHAMBER

**100 C.C. ION CAVITY
60 KVCP X-RAYS, NO FILTERS
HALF-VALUE LAYERS: 2.0 mm. Al**

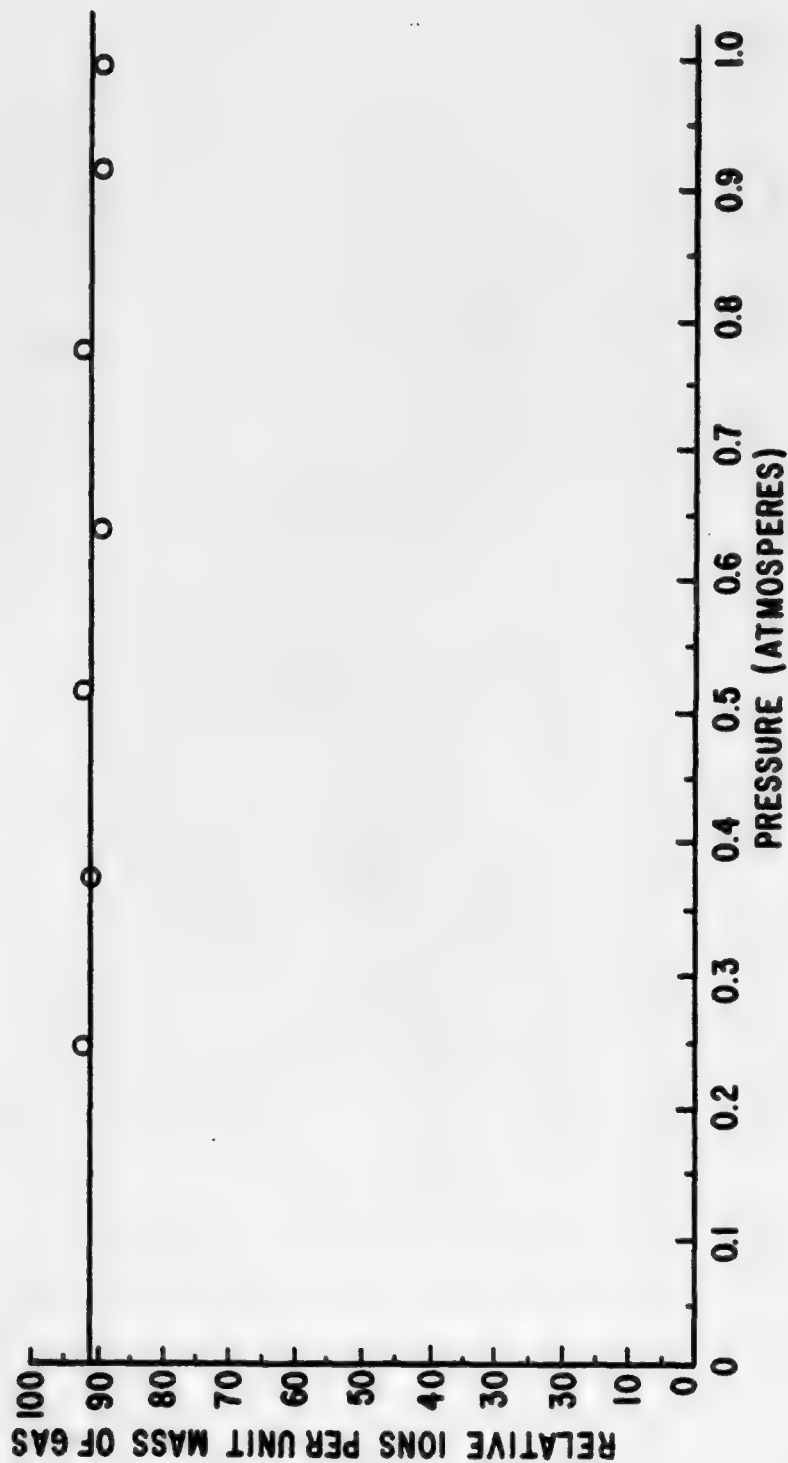


Figure 10. Gas-Hall Equivalent Test

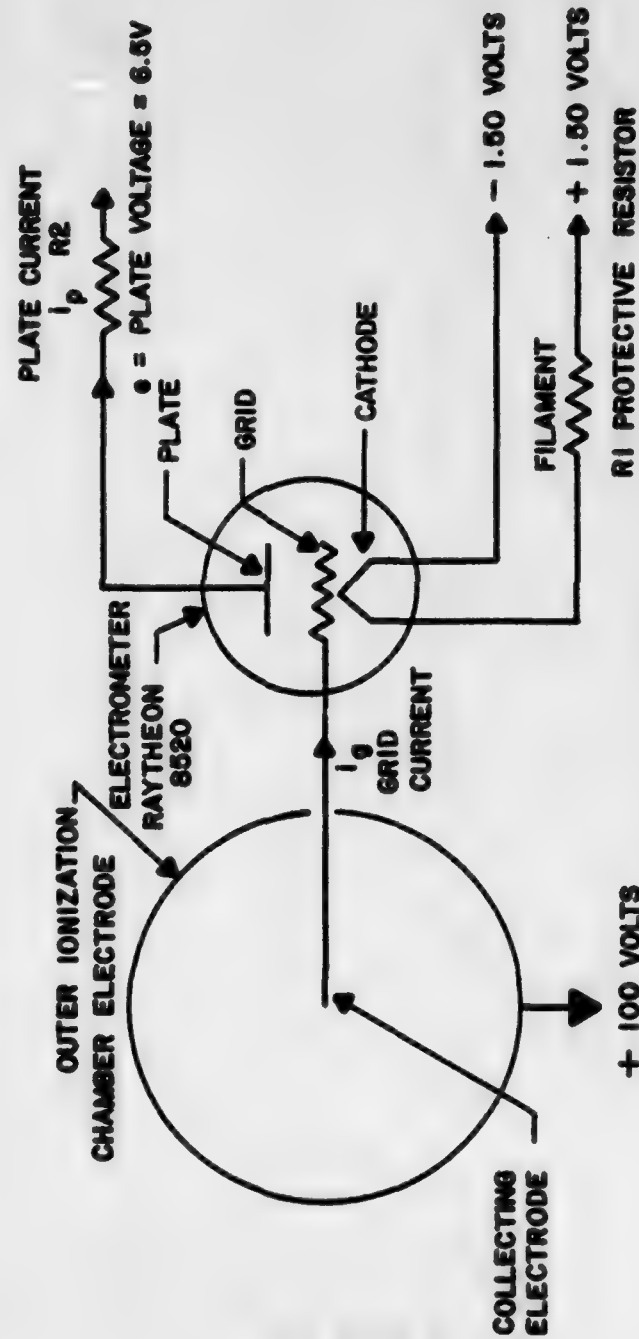


Figure 11. Tissue-Equivalent Ionization Chamber Sensor and Preamplifier

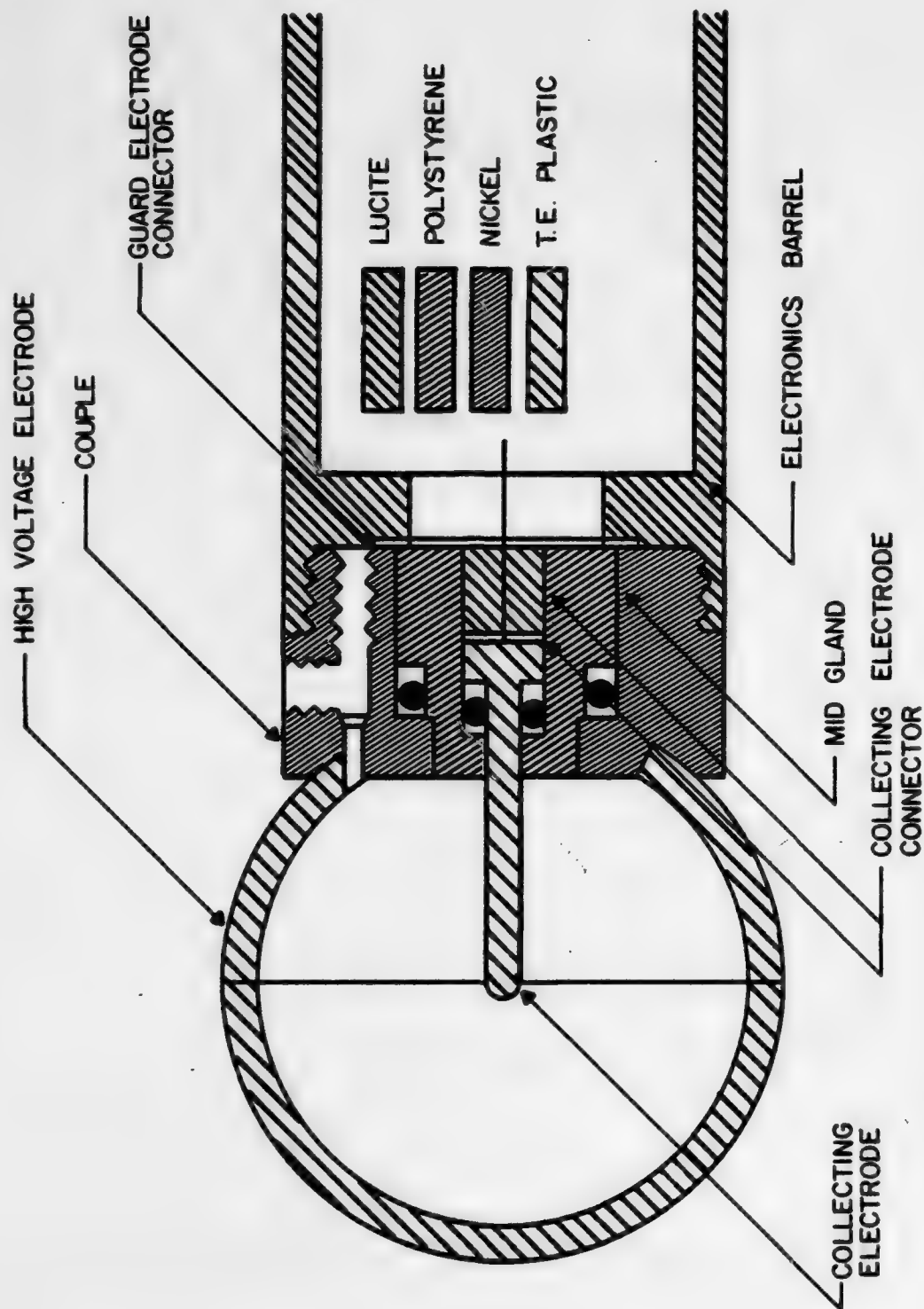


Figure 12. Tissue-Equivalent Ionization Chamber Sphere and Barrel Assembly

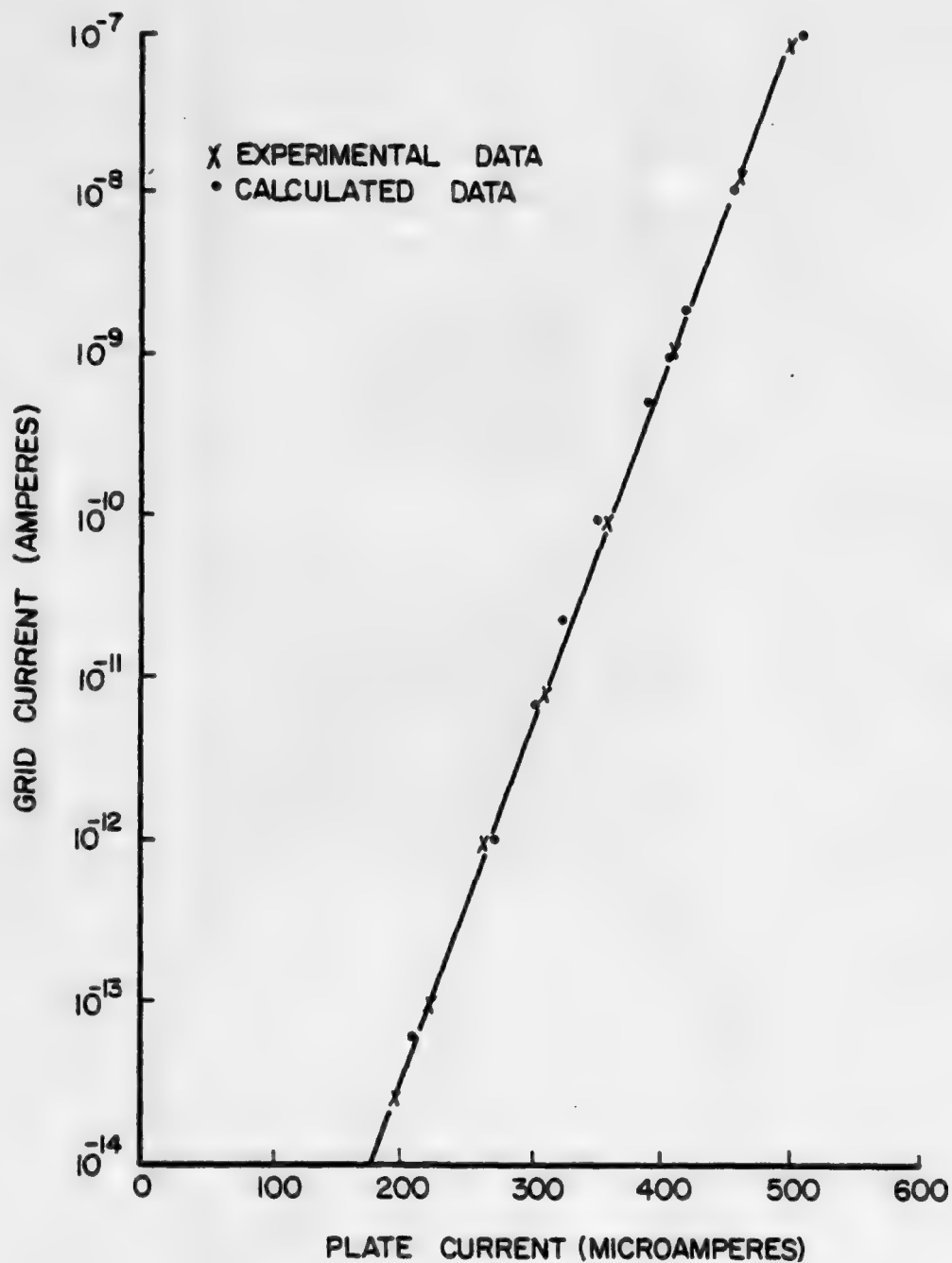
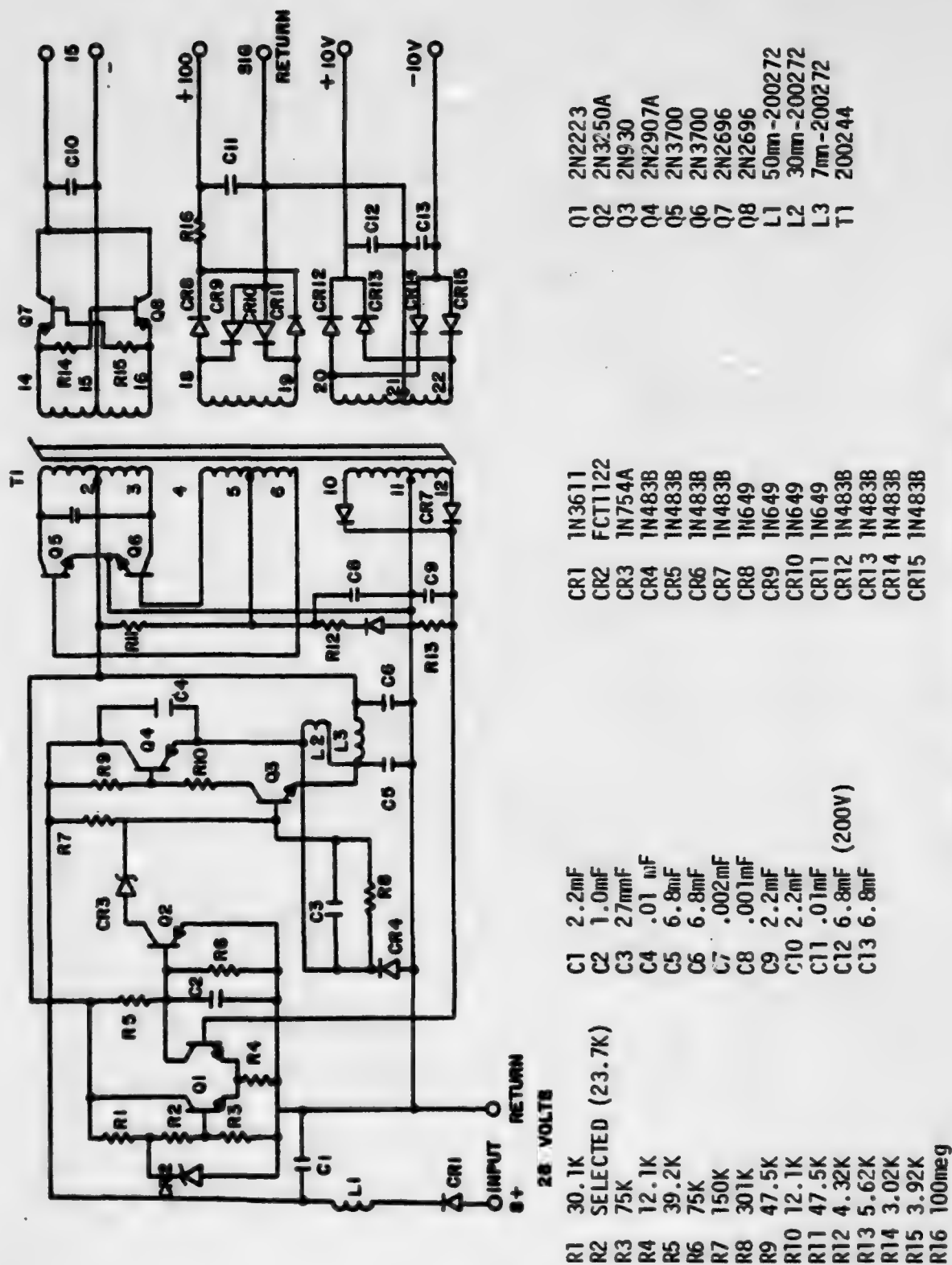


Figure 13. Grid-to-Plate Transfer Characteristics for a Raytheon 8520 Logarithmic Electrometer Tube



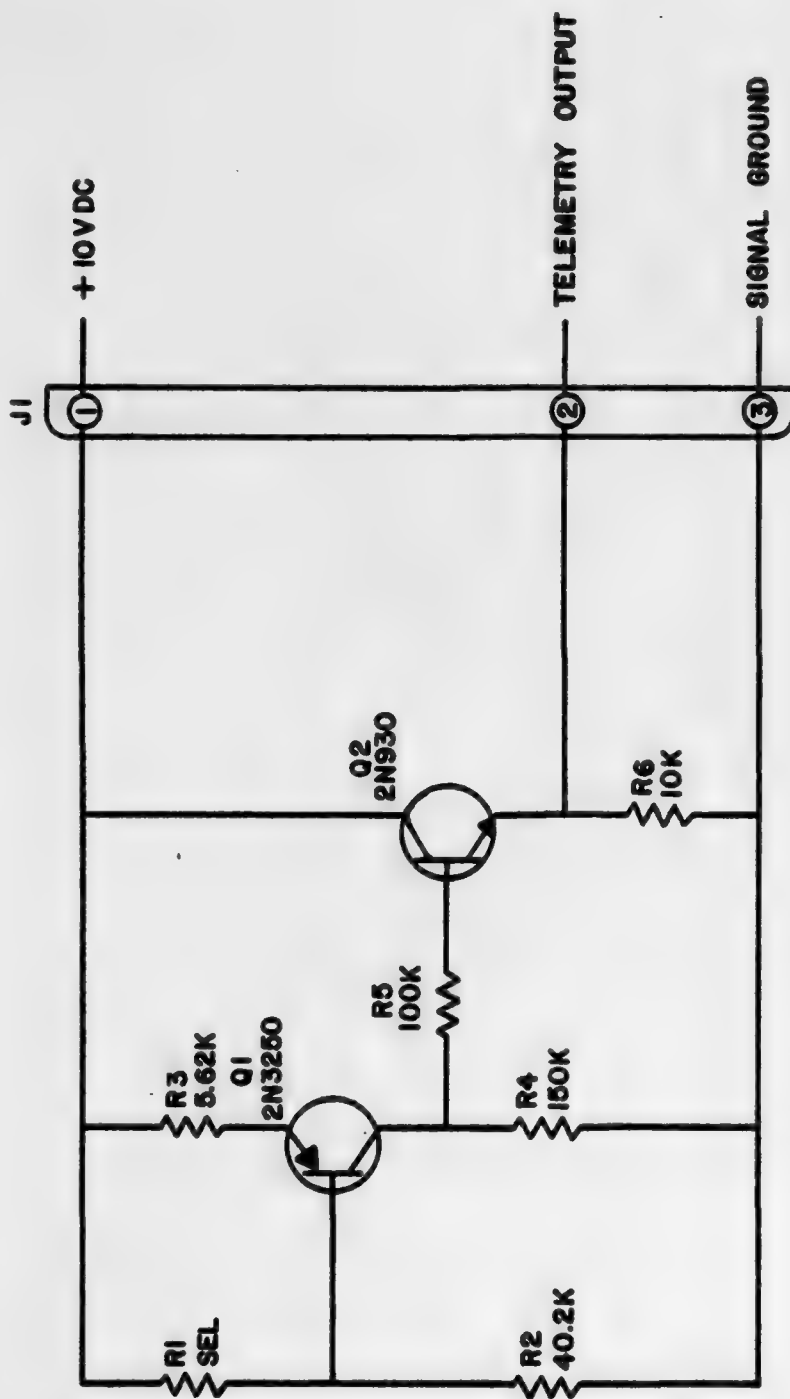


Figure 16. Temperature Sensor

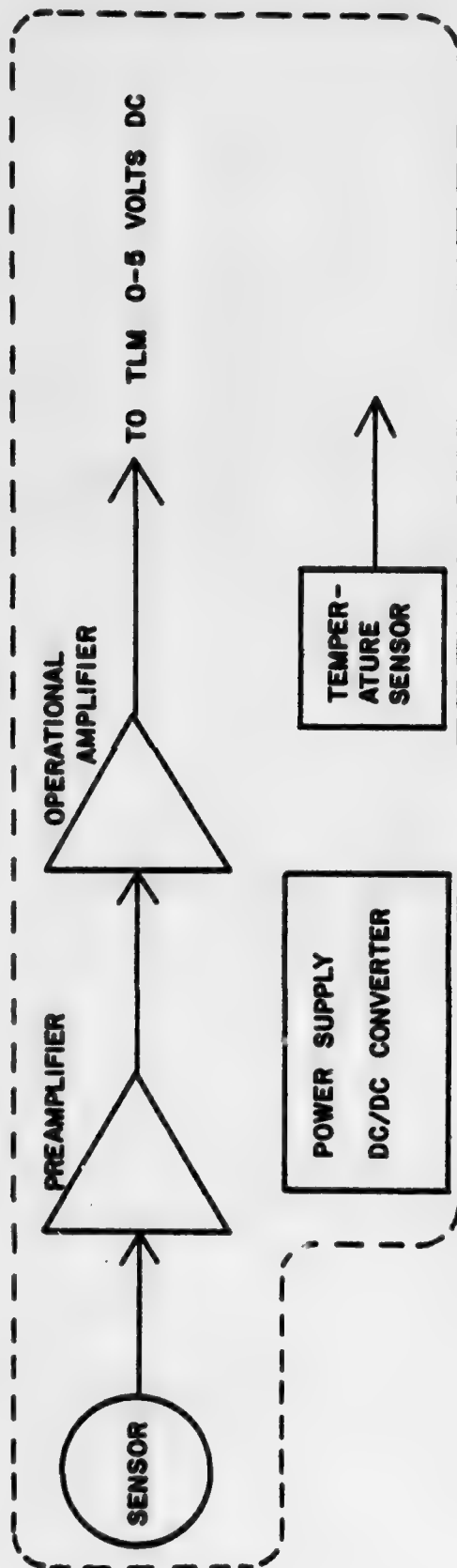


Figure 17. Active Dosimeter Block Diagram

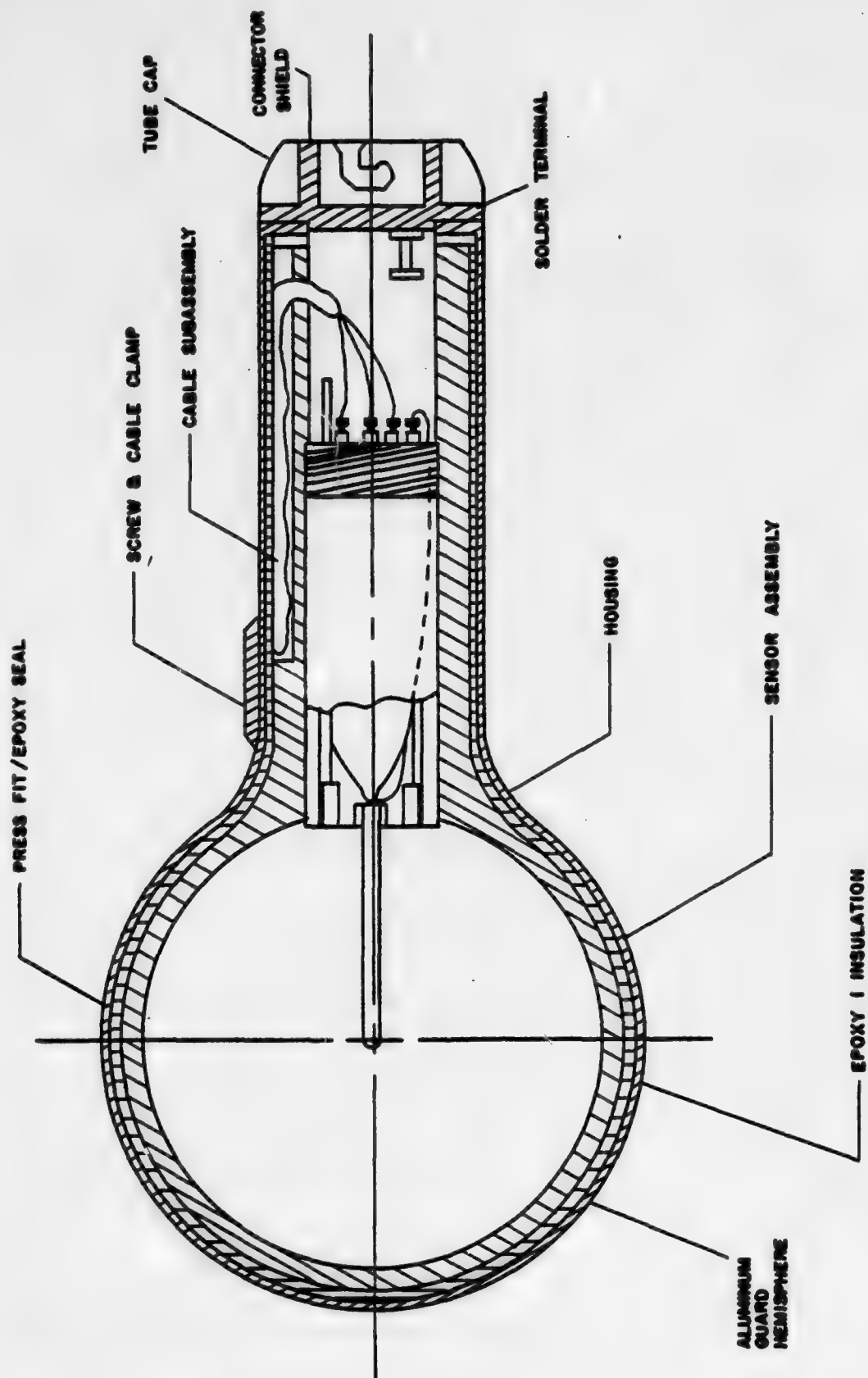


Figure 18. Sensor and Barrel Assemblies

SECTION III

LINEAR ENERGY TRANSFER (LET) SPECTROMETER SYSTEM DESCRIPTION

The linear energy transfer (LET) spectra of space radiations are, in general, complicated and difficult to measure. Devices have been developed in groundbased experiments (ref. 15) to measure LET spectrum employing low-pressure proportional counters. The numerous difficulties encountered by attempts to use proportional counters in space to measure the LET spectrum are avoided by the use of solid-state semiconductor detectors. These devices are commercially available in long-life, high-reliability versions that can be obtained in almost any variety of detector thickness.

We will describe here a two-detector, solid-state telescope used to measure the LET of protons, alpha particles, and heavy nuclei occurring inside a manned spacecraft. The sensor system employs two solid-state semiconductor detectors arranged in a charged particle telescope to collimate the radiation field.

The LET system employed in the Skylab Active Dosimeter consists of two lithium-drifted solid-state diode detectors operated as a charged particle telescope to measure the energy of protons and alpha particles that have entered the spacecraft command module. The LET detectors are Nuclear Semiconductors Inc. Model PT-3-1-1-1. The first (entrance) solid-state detector shown in figure 19 is 2.0 millimeters thick to provide the desired energy analysis of the high linear energy transfer components (lower proton and alpha particle energies) of the radiation environment entering the spacecraft. The second or antiscient detector is 1.0 millimeter thick. These two detectors are shielded with tungsten such that the protons and alpha particles enter almost entirely from one direction to simplify the analysis. The 2-millimeter detector of the charged particle telescope measures proton energies between 0.5 MeV and 18.5 MeV and alpha particles between 18.5 and 75 MeV. Shielding and detector design factors considered in this effort are presented in Appendix I.

The anticoincidence (second) detector measures total counts for protons above 18.5 MeV of energy and alpha particles above 75 MeV. The proton and alpha particle counts and energies measured by the LET spectrometer are

converted to LET spectra using range, energy, and ($dE/dX \approx LET$) tables generated by Janni (ref. 16). The relative dE/dX versus E responses for silicon and standard muscle tissue are uniquely defined and are shown in figure 20. The dE/dX values for the two materials differ by very nearly a constant over most of this energy range which will make conversion from dE/dX in silicon to muscle a straightforward process. The total counts in the intervals 0.5 to 18.5 MeV and greater than 18.5 MeV are also normalized for the TEIC dose-rate readings for baseline data in the depth-dose radiation surveys in the portable tissue equivalent ionization chamber.

The LET electronics are used to shape, analyze, select, and telemetry-condition the electrical pulses produced in the solid-state detectors. The major electrical subsystems for the LET are displayed in figure 21. These are as follows:

- (1) Detectors, preamplifier, shaper, and voltage amplifiers
- (2) Analyzer buffer amplifiers
- (3) Analyzers (discriminators)
- (4) Analyzer logic
- (5) Delayed strobe
- (6) MOSFET counters (seven-bit stair steps)
- (7) Ratemeter
- (8) Telemetry buffer amplifiers
- (9) Power supply
- a. LET Detector, Preamplifier, Shaper, and Voltage Amplifier Electronic Assemblies

The charge signals originating in the solid-state detectors when radiation strikes the detectors are converted to voltage signals by special charge loop preamplifiers A1 (see figure 21). These amplifiers have a sensitivity of approximately 10 millivolts/MeV of energy loss in the silicon solid-state detectors. The voltage pulses from the charge loops are processed by the shaper amplifiers A2 shown in the same figure. This amplifier develops a gain of 10 and requires 0.5×10^{-6} seconds for integration differentiation. The signal is finally amplified by specially designed voltage amplifiers A3 (see figure 21) which also have a gain of 10.

The electrical schematics for the detectors, preamplifiers, shaper amplifiers, and voltage amplifiers are shown in figure 22. The voltage amplifier differs from the X10 shaper amplifier in that the capacitor C10 is included in the shaper amplifier. The charge shaper and voltage amplifiers for detector 1 are completely analogous to the second detector's systems just described. For example, dual transistors Q7, Q9, and Q11 are analogous to Q1, Q3, and Q5.

b. LET Analyzer/Electronics

The pulse height analyzers (discriminators) perform the electrical function of selecting the shaped and amplified voltage pulses according to their amplitude and placing them in seven energy channels. There are seven discriminators labeled as (DISC FF or DISC OS) numbers 1 through 7 in the block diagram in figure 21 and A1 through A7 in figure 23. The pulse height analyzers are integrated circuits, RCA type CD2203s. These categorize electrical pulses generated in the first LET detector into the following energy intervals 0.5 to 2.0, 2.0 to 6.0, 6.0 to 10.0, 10.0 to 14.0, 14.0 to 18.5, and 18.5 to 75 MeV. A pulse 0.5 MeV in amplitude from the buffers triggers only the first of the pulse height analyzers, A1. Pulses of 18.5 MeV trigger all of the pulse height analyzers. The discriminators discussed previously are related to the logic circuitry as shown in figure 21.

c. LET Delayed Strobe Electronics

Integrated circuits A8 and A9 comprise the delayed strobe shown in figure 23. A9 generates pulse inversion for the delayed strobe while A8 is a double one-shot (the first one-shot has a 3-microsecond delay and the second has a 7-microsecond delay). This pulse action by the delayed strobe resets the discriminators and logic circuitry of the LET system. Since count rates of the order of no greater than 10^3 per second on the Skylab mission were predicted, this is more than satisfactory.

The pulse height analyzers (discriminators) select the shaped and amplified voltage pulses according to their amplitude into distance energy channels.

d. LET MOSFET Counter and Ratemeter Electronics

The MOSFET (Metal Oxide Silicon Field Effect Transistor) counters are shown in figure 24. They are RCA CD4004T MOSFET counters in ladder-adder R-2R

networks. These counters are output for the six energy analysis channels of LET detector. Typical output is shown in figure 25.

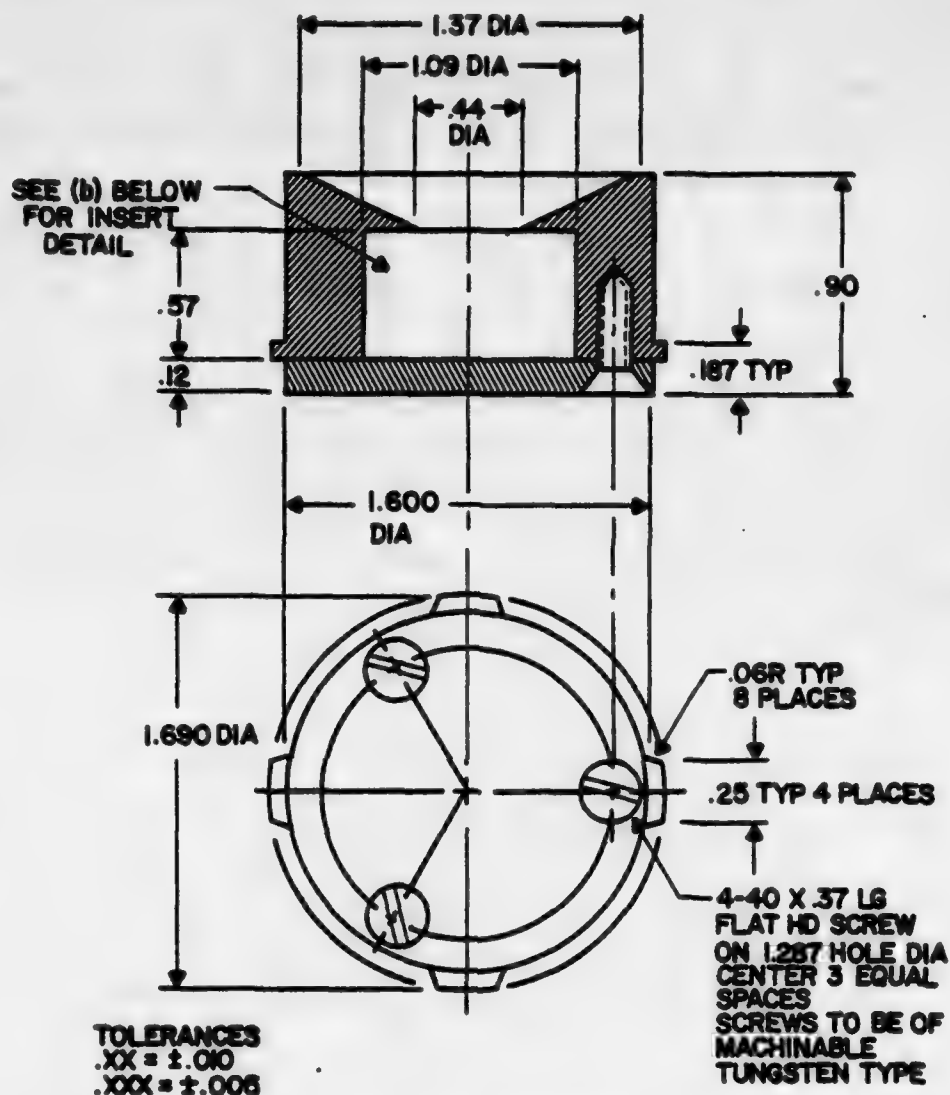
The ratemeter for the LET system in figure 24 is the output of the anticoincidence (second) detector. It converts particle count rate into a continuous 0.0- to 5.0-volt dc level.

The ratemeter is a logarithmic device designed so that 0.0 to 4000 counts/minute are recorded on a 0.0- to 5.0-vdc scale.

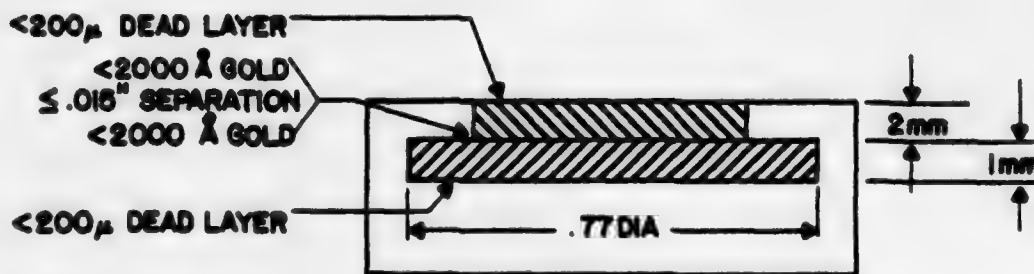
e. LET Power Supply Electronics

The LET power supply system in figure 26 supplies voltages to operate all other electronic subsystems just described. The power supply is designed to operate from a dc input of 28_{-6}^{+8} volts of unregulated spacecraft power.

The power supply regulator is the integrated circuit component A1, a National Semiconductor LM100 integrated circuit.



(a) LETS DETECTOR



(b) LETS DETECTOR INSERT

Figure 19. LET Detector and LET Detector Insert Final Flight System

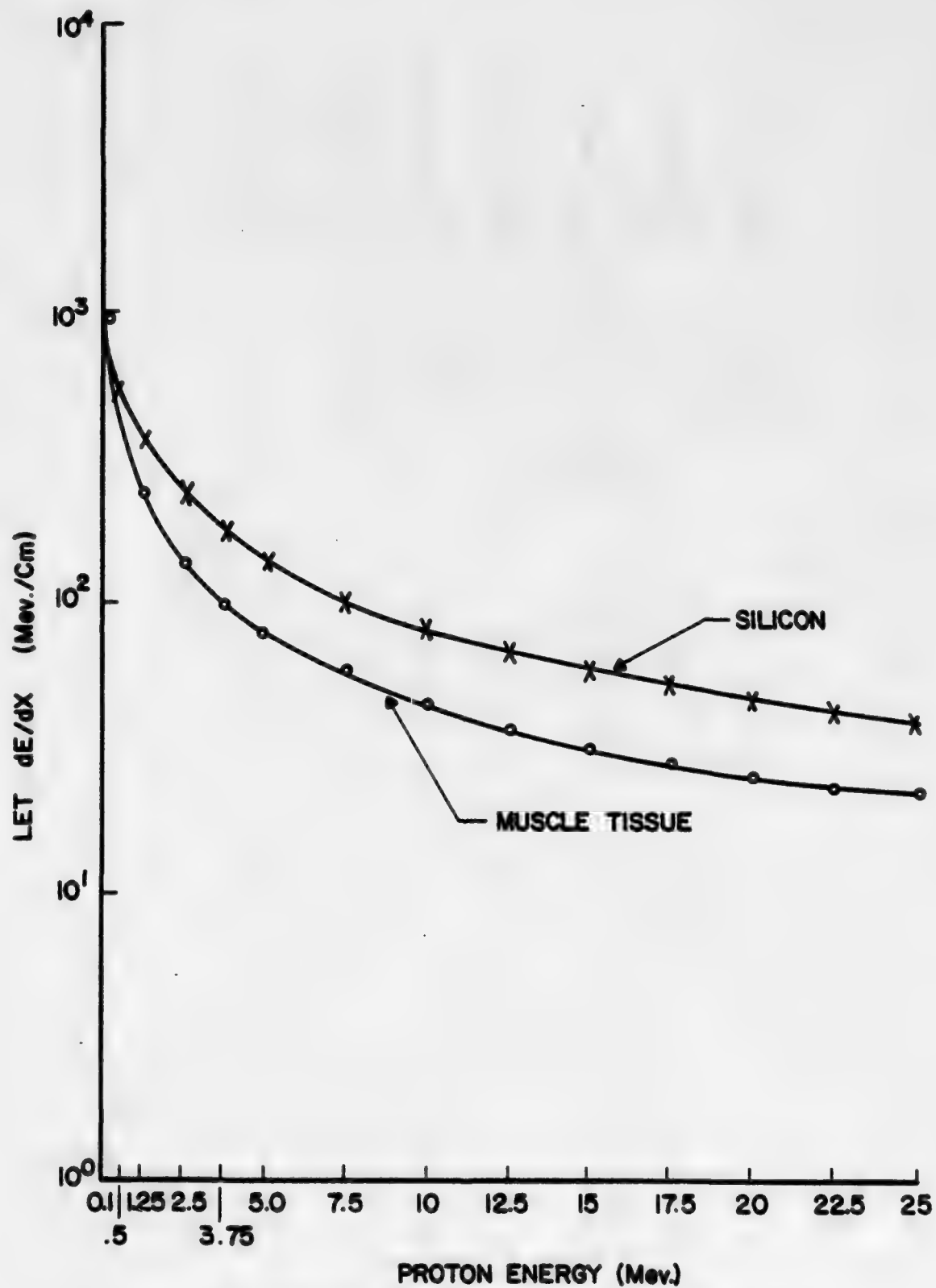


Figure 20. Stopping Power as a Function of Proton Energy

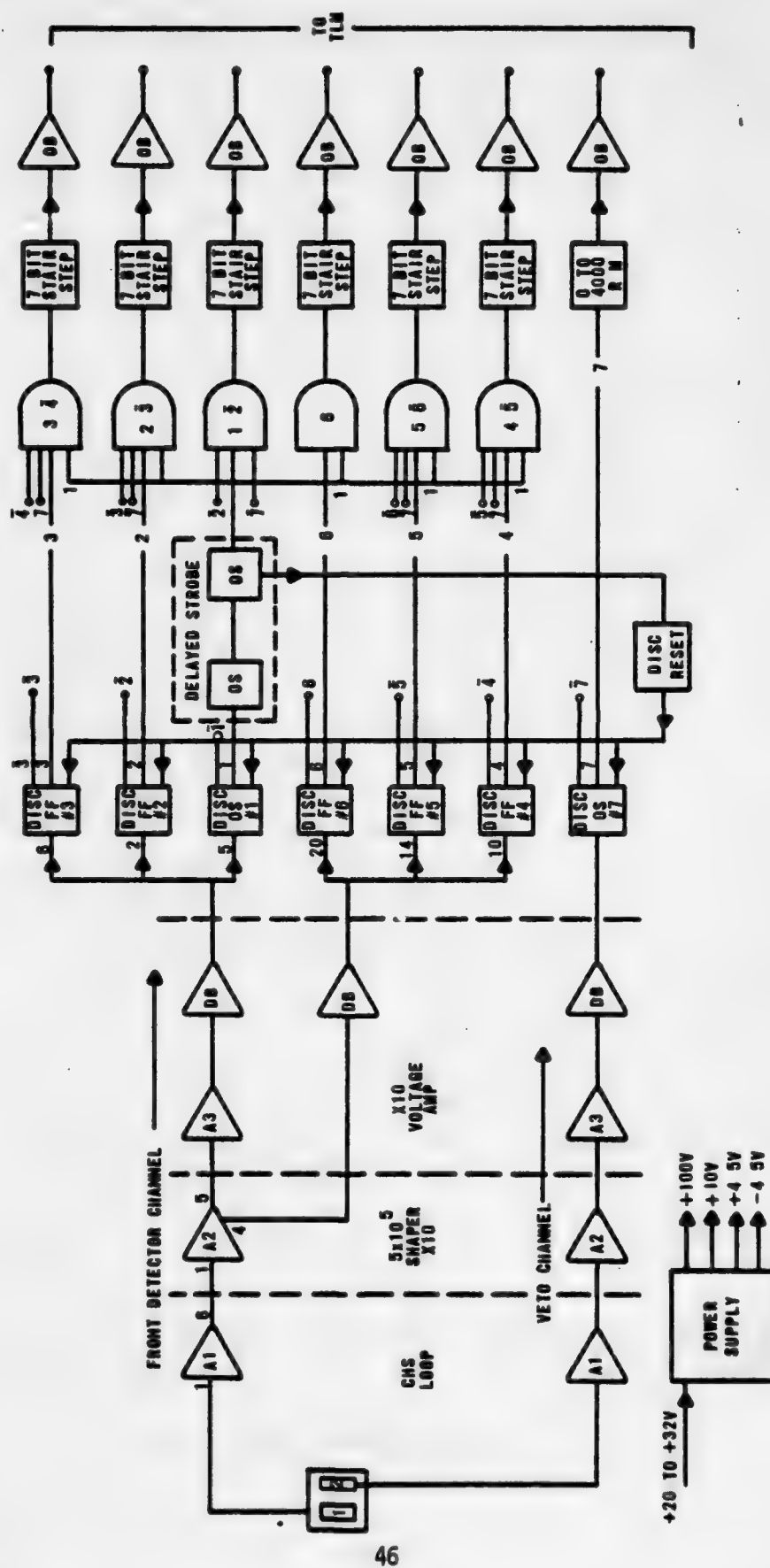
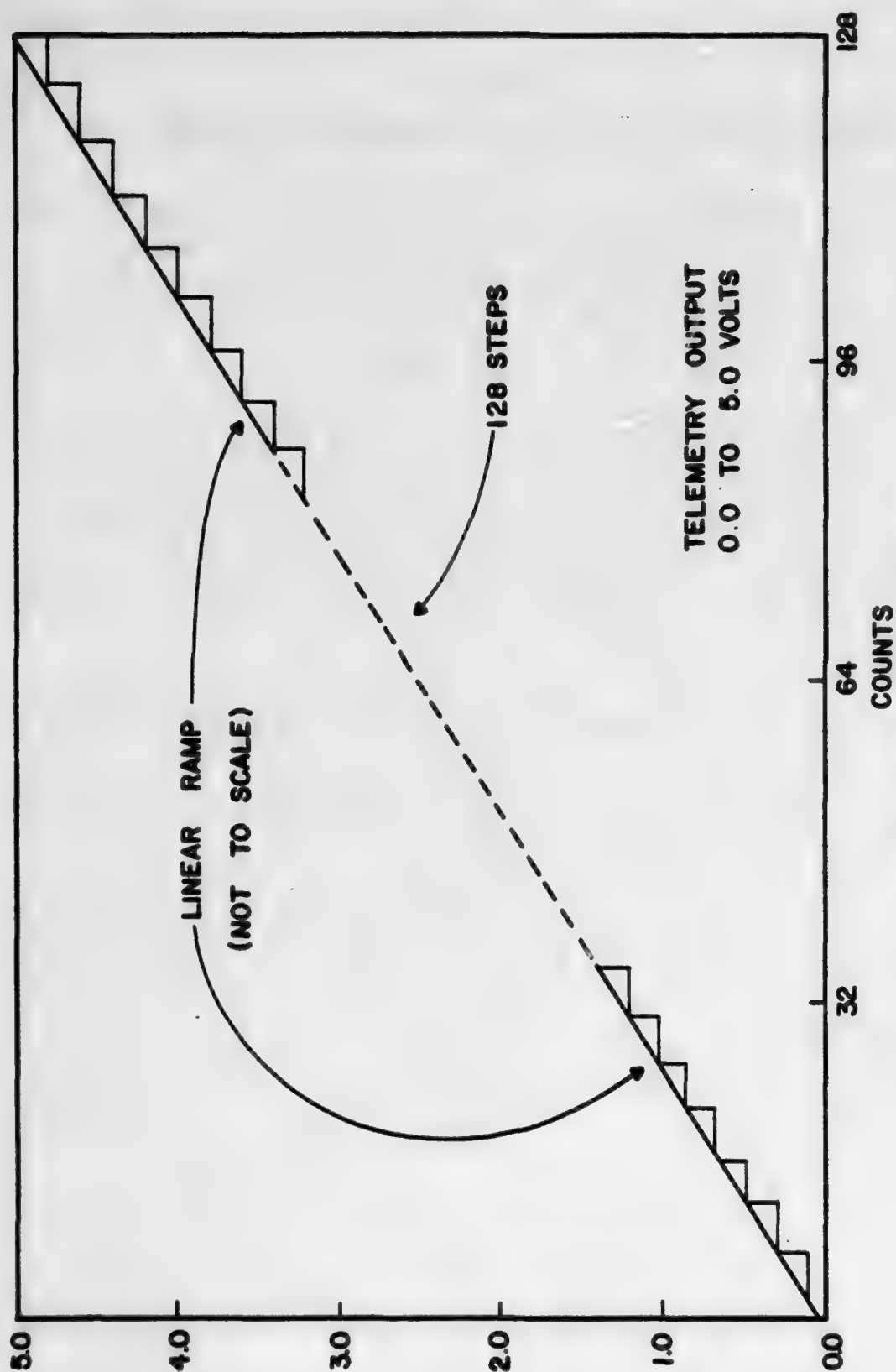


Figure 21. LETs Block Diagram



LINEAR RAMP - 25MV/COUNT
FROM 0 TO 128 COUNTS

Figure 25. LET Ramp Output

SECTION IV

MECHANICAL AND ELECTRICAL DESIGN OF OVERALL ACTIVE DOSIMETER SYSTEM

The active dosimeter mechanical envelope is displayed in figure 27. The mechanical package contains the semiportable tissue-equivalent ionization chamber, linear energy transfer spectrometer and the associated electronic modules previously described. The semiportable radiation sensor was used for radiation surveys in the Skylab II command module.

The individual module mountings in the active dosimeter mechanical envelope are shown in figure 28. The mounting of the modules is designed to withstand accelerations up to 150 g in all directions. All mounting and support brackets for the modules are aluminum. The cover for the modules is also 0.0325-inch thick aluminum. The entire external finish of the active dosimeter, exclusive of TEIC portable radiation sensor assembly, is a chemical (alodine) film conforming to MIL-C-5541.

The portable TEIC radiation sensor is attached by a retractable spring cable to the parent active dosimeter housing. The spring extends to 6.5 feet from the dosimeter chassis for both on-body and spacecraft shielding surveys. When not in survey use, the portable sensor is locked into the active dosimeter package. Locking and unlocking the sensor is accomplished by a quarter turn of the locking mechanism and the simultaneous application of approximately 3 pounds of pressure. This entire sensor-locking mechanism has been successfully tested to shock and acceleration levels up to 150 g's and to vibration levels more severe than the Apollo command module levels.

The active dosimeter electrical interface with the spacecraft is through a single flight-approved electrical connector.

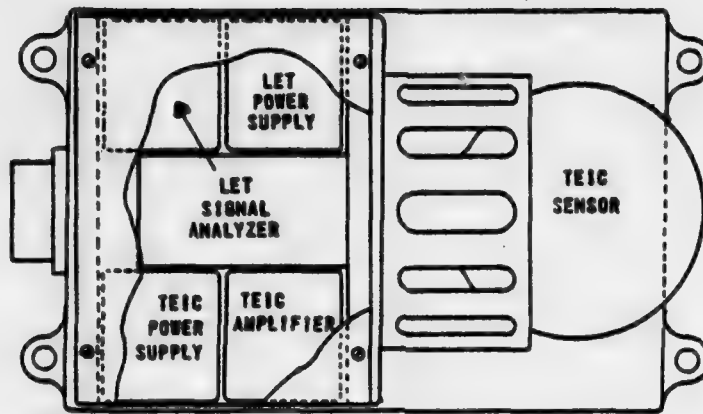


Figure 27. Active Dosimeter Module Mounting (Top View)

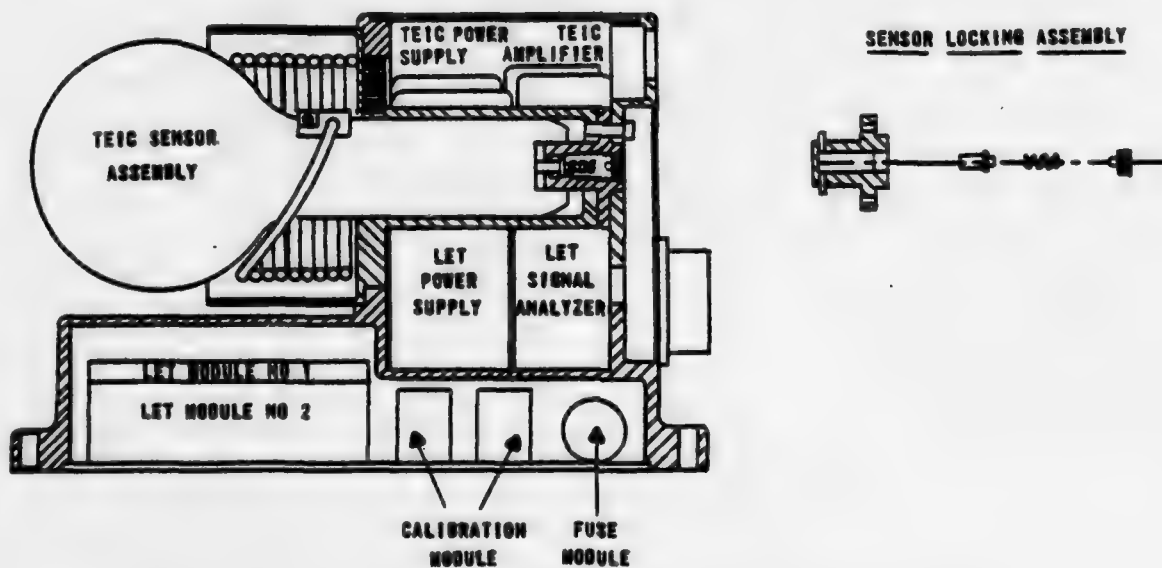


Figure 28. Active Dosimeter Module Mounting Sensor-Locking Assembly (Side View)

SECTION V

TELEMETRY OUTPUTS FOR THE ACTIVE DOSIMETER

The active dosimeter flown on Skylab II has nine data and status output signals. The following table describes each channel, its dosimeter parameter, and ideal sample rate.

<u>Channel</u>	<u>Parameter</u>	<u>Typical sample rate</u>
1	TEIC dose rate	every 0.8 sec
2	LET 0.5 - 2.0 MeV	every 0.8 sec
3	LET 2.0 - 6.0 MeV	every 0.8 sec
4	LET 6.0 - 10.0 MeV	every 0.8 sec
5	LET 10.0 - 14.0 MeV	every 0.8 sec
6	LET 14.0 - 18.5 MeV	every 0.8 sec
7	LET anticoincidence 18.5 - 75 MeV	every 0.8 sec
8	Alpha particle counts 18.5 - 75 MeV	every 0.8 sec
9	Temperature sensor	every minute

SECTION VI

APOLLO ACTIVE DOSIMETER TEST RESULTS

The active dosimeter was required to undergo a rigorous qualification test program to meet all manned spacecraft specifications as well as a number of operational tests to calibrate the system and ensure that it remained in calibration. Separate types of tests were used for the tissue-equivalent ionization chamber and the LET system.

1. TISSUE-EQUIVALENT IONIZATION CHAMBER TEST RESULTS

The tissue-equivalent ionization chambers were calibrated with gamma radiations from the isotopes of cobalt-60 and cesium-137 at the NBS-calibrated radiation ranges of the Sandia Corporation. The output voltage as a function of incident radiation is displayed in figure 29. The response times of the tissue-equivalent ionization chambers were determined during irradiation by the sources described above and are indicated below.

<u>Radiation level</u>	<u>Rise time (sec)</u>	<u>Decay time (sec)</u>
2.9 mrad/hr to 1.05 rad/hr	0.525	1.40
10.0 mrad/hr to 5.7 rad/hr	0.480	1.50
0.5 rad/hr to 16.5 rad/hr	0.21	0.45

The rise time is defined as 90 percent of the lowest radiation value indicated, and the fall time is 110 percent of the lowest radiation level. The instrument is stable for temperatures between 0° and 120°F. For temperatures between -40° to +160°F the instrument does not drift by more than 10 percent from its radiation response at room temperature.

2. LINEAR ENERGY TRANSFER SPECTROMETER DETECTOR TESTING

Three types of tests were developed to calibrate the LET system. These included (1) radiation sources, (2) precision pulser, and (3) cyclotron irradiation. To activate the first two LET data channels (0.5 to 2.5 and 2.5 to 6.0 MeV), 5.476-MeV alpha particles from Americium-241 were used. A typical

spectrum obtained from a solid-state detector using this source is shown in figure 30. The alpha source could not be employed after final assembly of this system because the entire LET detector is hermetically sealed. Therefore, functional testing was conducted with strontium-90 beta rays. The strontium source emits beta rays that penetrate the metal hermetic seal and activate both detectors to test their operation. The spectrum measured in the anticoincidence detector for strontium-90 is shown in figure 31.

A precision 1-micro-microfarad capacitor is mounted to each input of the preamplifiers shown in figure 24 to conduct tests with an electronic pulser. The capacitors are mounted to the first input pin of the preamplifier. The capacitors are connected through a coaxial cable system to pins in the system's power and signal connector. Pulses from a precision pulser are applied to the preamplifier inputs. The test pulse has a rise time of approximately 10^{-8} seconds and a decay time of about 3×10^{-4} seconds. Each solid-state detector produces approximately 4.5×10^{-4} coulombs of charge for each MeV liberated in it. Using the simple relation $V = Q/C$, the pulse amplitude that is equal to 1 MeV is 45 millivolts. Pulses equivalent to 1.5, 4.0, 7.5, 12, 15, and 50 MeV were used to test the six LET channels.

Measurements were conducted at the Oak Ridge, the Texas A&M, and the Harvard cyclotrons using degraded proton beams to ensure that the proper energy detection and pulse discrimination were achieved by the LET electronics. The results of the various irradiations with protons of 5, 9, 12, 15, 20, 25, 30, 100, and 120 MeV verified correct operation of the LET system for these energies.

3. PASSIVE DOSIMETRY SYSTEMS

The passive dosimetry portion of the Skylab radiation monitoring system determines the radiation intensities at five shielding locations within the Skylab II. These intensities are a function of the space radiation environment exterior to the spacecraft, mission length, orbital variables, and dosimeter location within the spacecraft. The passive dosimetry units were located at points approximating maximum, minimum, and intermediate shielding. Each contained the following dosimeters: lithium-fluoride and calcium-fluoride thermoluminescent dosimeters, a quartz-fiber ionization chamber, nuclear emulsions, plastic polymers, and gold and iridium foils.

Each passive dosimeter unit for Skylab includes a series of small, rugged individual dosimeters housed in a sealed aluminum canister. A diagram of the aluminum mounting containers and each of the individual dosimeters within the small cylindrical container are shown in figure 32. Figure 33 shows the aluminum canister construction, Teflon shock mounts, and the mounting arrangement of the individual dosimeters. The canister and the end mounts are anodized aluminum. The canisters are hermetically sealed by a Teflon O-ring. The passive dosimeters do not require electrical power or telemetry connections.

Selection of the dosimeter materials was strongly influenced by the volume and weight limitations which are associated with spacecraft. Each passive dosimetry unit, including all contents and the aluminum container, weighed only 0.37 pound. The weight restrictions did not allow the more standard technique of successively varied and increased shield thickness about each dosimeter to be used. For this reason, the inherent charged particle response of the various individual dosimeters was used to evaluate the particle type and energy cutoff. Only one calcium-fluoride thermoluminescent dosimeter in each canister was shielded. The dosimeters selected for use are discussed individually in the following paragraphs.

a. Thermoluminescent Dosimeters

Several types of thermoluminescent dosimeters are commercially available, but only the glass-enclosed lithium fluoride and calcium fluoride types manufactured by EG&G (ref. 17) are used. When a thermoluminescent material is irradiated, electrons become trapped at lattice imperfections within the crystalline solid. This trapping is relatively stable at temperatures on the order of 70°F, but the addition of large amounts of thermal energy causes the electrons which were trapped within the imperfections of the solid to be thermally agitated, allowing them to combine with charge carriers of the opposite sign. Visible light is emitted in this process which can be correlated with the amount of absorbed energy that has been deposited within the material. Calcium fluoride and two isotopes of lithium fluoride were flown in the Skylab passive dosimeter systems. These materials are sealed within a glass container similar in construction to a small vacuum tube. An ohmic heater allows a known quantity of heat to be applied and also provides a very high degree of reproducibility in the system. The fluoride must be heated in a vacuum or in a pure, inert-gas atmosphere to eliminate spurious luminescence peaks. The

emitted light is measured by using a photomultiplier tube and an associated electronics system to determine the intensity of the light emission. This dosimetry system is quite sensitive and can record total doses as low as 10 millirads, approaching precisions of 10 percent. The percent accuracy improves rapidly as the total dose increases. A shield was used on one of these dosimeters in each canister to provide charged particle cutoff points at reasonably well-defined energies.

Two different lithium isotopes were used to determine the contribution of secondary thermal neutrons to the total dose. Because the ${}^7\text{Li}$ isotope has a very low neutron cross section compared to the ${}^6\text{Li}$, the difference between the readings of the ${}^6\text{Li}$ and ${}^7\text{Li}$ types may be interpreted as the thermal neutron dose.

b. Nuclear emulsions

Practical methods of obtaining comprehensive information on the linear energy transfer (LET) using passive dosimeters are limited to the uses of nuclear emulsions. The most severe problem associated with the use of emulsions on long-duration missions is that of track fading with time. A variety of emulsions are available, and some have more severe fading characteristics than others. Emulsions of the Ilford G-5 and K-2 types are very suitable and have been chosen for use on Skylab. The track fading is considerably less for the G-5 emulsion than for the K-2 types. However, this fading does not introduce particle losses greater than 30 percent for missions of 1 month.

The G-5 emulsion is considerably more sensitive than the K-2 emulsion. Using a combination of these two emulsions allows resolution of proton and alpha tracks of low energies which would be saturated in the G-5 emulsion alone but which still may be cleanly detected in the K-2 emulsion. This arrangement also allows discrimination of electrons from protons and alphas over the LET range 0.2 keV/micron to greater than 85 keV/micron. This is accomplished by postflight microscopic examination of the individual particle tracks in the developed emulsions. The grain density is then used to establish the atomic number of the charged particle, and the straggling and scattering of the tracks are used to differentiate electrons from the heavier protons and alphas.

After a statistically significant number of particle tracks are counted over a broad range of energy deposition values, an integral spectrum is determined. This is then differentiated to obtain a differential spectrum. The

tissue dose, required for comparison with active dosimeter data, is established by assuming the track population in the emulsion is the same as would have existed in an equivalent volume of tissue. The tracks from protons and helium nuclei are very similar, and the majority cannot be distinguished. However, a differential LET distribution for these particles can be determined, and the tissue dose is then found. The tissue-equivalency problems associated with the use of these emulsions are circumvented in this manner.

A large amount of bremsstrahlung is registered in the emulsions with increased electron population. The greater majority of such secondary electrons is readily identifiable.

Emulsions which have grains and grain spacing much larger than nuclear track emulsions are not capable of producing individual tracks. An increase in the optical density as a function of incident radiation intensity for those types of emulsions allows them to be used as dosimeters. Although this method has been widely used in health physics applications, there are still calibration and processing uncertainties as well as serious tissue-equivalency problems with the use of such emulsions in unknown radiation fields. Because the LET cannot be determined, densitometric emulsions cannot be directly corrected to tissue response as can nuclear track emulsions. For these reasons, densitometric emulsions were not included in the Skylab passive dosimeters, and only the Ilford G-5 and K-2 nuclear track emulsions were used. The nuclear emulsions are being processed and analyzed for this experiment by Dr. Herman J. Schaefer of the Naval School of Aviation Medicine.

c. Plastic Polymers

Several plastic polymers are capable of recording the heavy ion component of the galactic cosmic radiation. These detectors have a number of characteristics that make them particularly appropriate for this application. They are light, rugged, compact, insensitive to temperature and humidity changes, have no latent image fading at ordinary temperatures, and are straightforward to process. Since protons and electrons are not registered, the heavy ions can be detected without being masked by an associated proton or electron population. This method allows classification of multicharged particles by their rate of energy loss.

The polymers flown on Skylab consisted of a sandwich of three layers of different polymers, each having a well-defined sensitivity. A particle

traversing this system will leave tracks in some polymers and not in others. Counting tracks in each of the polymers provides the flux of particles above some known value of LET. By subtracting the fluxes recorded in adjacent materials, the flux of particles in a given broad range of LET can be obtained. The resolution of such a system depends upon the number of polymers used, and at least three polymers are required to provide adequate information concerning the heavy particle contribution.

d. Activation Foils

Dosimetry by means of activation foils suffers from two primary difficulties. They are relatively insensitive to low level radiation and the information contained in an activation foil decays with time. Nevertheless, two types of activation foils were suitable for use in the Skylab passive dosimeter units to provide an evaluation of the neutron fluences. These were small gold and iridium foils which were included because of their very low volume and weight.

A small gold activation foil was used to provide information concerning the thermal neutron detector having an effective cross section of 98.9 barns with a half life of 2.7 days. The large cross section tends to offset the radioactive decay resulting from the 2.7-day half life. The thermal neutron detectability within one half life is about 10^6 n/cm². Except for the resonance at 5 eV, gold is not an epithermal or high energy neutron detector. With modern counting equipment and proper care, gold activation equivalent to 1 rad of thermal neutron fluence can still be counted after 10 half lives.

Iridium is sensitive over a broader neutron energy band than gold. Two isotopes of iridium were used to detect thermal as well as higher energy neutrons; both isotopes were contained within the same foil. The $^{77}\text{Ir}^{191}$ isotope is 38.5 percent abundant and under neutron irradiation goes to $^{77}\text{Ir}^{192}$ via two metastable states. The $^{77}\text{Ir}^{193}$ isotope is 61.5 percent abundant and has a neutron capture cross section of 110 barns; the product nucleus is $^{77}\text{Ir}^{194}$. The effective neutron capture cross section for naturally occurring iridium containing both the $^{77}\text{Ir}^{191}$ and $^{77}\text{Ir}^{193}$ isotopes is 453 barns, with 385 barns (ref. 19) being contributed by the 38.5 percent abundant $^{77}\text{Ir}^{191}$.

e. Quartz-Fiber Ionization Chamber

Operation of quartz-fiber dosimeters is well known. They consist of a sensitive chamber, a quartz-fiber electrometer, and a charging system. This

response time is determined by the capacitance between the various parts of the chamber.

Response times of dosimeters of this type are generally quite rapid and are more than adequate to record the slowly accumulating dose anticipated on the Skylab mission. Dose fading is usually not negligible in such dosimeters and may be as large as 1 percent per day; however, the dosimeters selected for this flight, manufactured by the Dosimeter Corporation, Cincinnati, Ohio, have leakages much less than this.

f. Analysis Considerations

For the passive dosimeters to record primarily the radiation dose during the length of the flight and not the background accumulation caused by the galactic cosmic radiation that penetrates to the earth's surface, the flight passive dosimeters were installed in the spacecraft 3 days prior to launch. Ground control dosimeters were used which were configured identically to the flight units. Prompt recovery was important because of the dose-fading characteristics of several of the individual dosimeters.

4. SYSTEM FLIGHT PERFORMANCE DATA AND RESULTS

a. Active Dosimeter Flight Data

The active dosimeter provided measurement of the dose rates and charged particle fluences and spectra during the mission of Skylab II. Data were recovered for large portions of the mission. Intermittent data recovery was not planned initially but was enacted to conserve spacecraft power. The system functioned normally with no anomalies noted in its performance. Following flight on Skylab II, the active dosimeter was returned to the ground and recalibrated using the Sandia Corporation cobalt-60 sources for the ionization chamber and a precision electronic pulser for the particle spectrometer. No significant drifts in either of the active dosimeter subsystems were observed when compared to preflight calibration levels. Temperatures as monitored by the self-contained temperature monitoring system did not vary by more than +20°C over the duration of the mission, indicating that thermal effects on the active dosimeter measurements were negligible.

Peak dose rates recorded by the active dosimeter ionization chamber were on the order of 100 millirads/hour during passes through the highest flux regions of the South Atlantic anomaly. Dose rates varied downward from this

level to the cosmic background at equatorial geomagnetic cutoff of 0.05 millirads/hour. Figure 34 displays a series of consecutive passes of measured dose rates in the South Atlantic anomaly. Figures 35 through 43 are selected data from the active dosimeter for typical Skylab II passes through the South Atlantic anomaly. Dose levels analyzed over the duration of the Skylab II mission show a high degree of constancy for the same B, L points. No unusual solar activity was reported during this period that could have caused measurable changes in the energetic proton component of the trapped radiation as measured by the active dosimeter.

One of the four planned surveys by the astronauts with the portable active dosimeter ionization chamber was conducted without any reported astronaut difficulties. The survey was only partly successful because it was conducted during a grazing pass of Skylab into the South Atlantic anomaly, and data was recovered from only a portion of the survey. Figure 44 shows the variation of dose rate from the ionization chamber with the several shielding locations for which data were recovered. It is observed that the dose rate is reduced by a factor of three for the simulated gut dose from surface or stowed sensor levels. Results are not meaningful for other survey locations performed before a GMT of 169:10:42:45 because the Skylab had not yet entered the South Atlantic anomaly. Planned cosmic radiation surveys similar to those conducted in the South Atlantic anomaly were not conducted because of time limitations on astronaut activities.

The charged particle spectrometer data from the active dosimeter LET system has not been completely analyzed. Preliminary examination of LET data in the South Atlantic anomaly show that the degraded particle spectra internal to the spacecraft have an RBE varying between 1.5 and 2. The data are in agreement with film emulsion results reported on previous Apollo missions and elsewhere on Skylab. Comparisons at this time are at best qualitative because the emulsion data were generated at different shielding locations and include galactic radiation components whose spectral shape is different from the degraded trapped particle spectra. In the South Atlantic anomaly it was generally observed that the internal particle spectra consisted of predominately low energy protons. In the data examined to date, the low energy channel consistently recorded the greatest count rate with each succeeding higher energy channel indicating a decreasing count rate. Confirmation that the low energy particles are protons and not electrons and bremsstrahlung must await the final

analysis of particle tracks in film emulsions flown in the passive dosimeter with similar shielding as the active dosimeter. Alpha and higher Z-particle ($18.5 < E < 75$ MeV) fluxes were usually limited to less than 10 particles/cm²-sec.

b. Passive Dosimeter Data and Results

Postflight readout and analysis of the Skylab II passive dosimeter elements was accomplished within 3 days after completion of the mission. Readings for each of the seven individual sensors in the five locations (figure 45) are summarized in table 3.

The average reading for all Skylab II thermoluminescent dosimeters was 1225 millirads. This may be interpreted as a measure of the average dose that could be received by the crew members operating continuously in the command module (Skylab II). Thermoluminescent dosimeter readings ranged from a maximum reading of 1665 millirads in the least shielded position to 960 millirads at the location of greatest shielding. The mean dose readings of the unshielded calcium and lithium-fluoride thermoluminescent devices at the five passive dosimeter mounting locations were as shown in table 4. The calcium-fluoride thermoluminescent dosimeters shielded by 100 mg/cm² of lead provided the measurements shown in table 5 at the same five locations. The shielded CaF thermoluminescent elements provided readings that were both lower and higher than the unshielded CaF thermoluminescent devices. Readings at locations 1 and 2 were higher for the unshielded CaF and slightly lower for locations 3, 4, and 5 than the shielded CaF. This behavior is not unexpected since the 100-mg/cm² high atomic number material used in the shield is not effective against energetic charged particles. These results also confirm the relative lack of appreciable soft bremsstrahlung X-rays ($E < 200$ keV) within the Skylab command module. The higher shielded dosimeter readings at locations 3, 4, and 5 are attributed to anisotropies (paths of higher radiation entry) within Skylab.

The readings of the ⁶LiF dosimeters (high thermal and intermediate neutron cross sections relative to ⁷LiF) were in all cases lower than the ⁷LiF units. Differences in the average readings between pairs of ⁶LiF and ⁷LiF dosimeters ranged from 78 millirads at the location of least shielding to only 8 millirads at location 4. The ten-unit average of the ⁷LiF was 45 millirads higher than the ⁶LiF ten-unit average. These results indicate no measurable

Table 3

SKYLAB PASSIVE DOSIMETER ACCUMULATED DOSE MEASUREMENTS
(Locations referenced to figure 45)

<u>Location</u>	<u>Dosimeter type</u>	<u>Dosimeter serial number</u>	<u>Recorded dose (millirads)</u>
1	CaF (shielded)	G-810	1595
1	CaF (no shield)	G-830	1640
1	⁶ LiF	L-679	1558
1	⁶ LiF	L-680	1586
1	⁷ LiF	L7-114	1665
1	⁷ LiF	L7-115	1635
1	Ionization chamber	000001	1210
2	CaF (shielded)	F-150	1105
2	CaF	F-905	1130
2	⁶ LiF	L-676	1125
2	⁶ LiF	L-683	1085
2	⁷ LiF	L7-118	1145
2	⁷ LiF	L7-124	1140
2	Ionization chamber	00010	870
3	CaF (shielded)	G-449	1355
3	CaF	G-825	1305
3	⁶ LiF	L-675	1231
3	⁶ LiF	L-694	1261
3	⁷ LiF	L7-110	1290
3	⁷ LiF	L7-117	1305
3	Ionization chamber	00003	950
4	CaF (shielded)	H-165	1000
4	CaF	G-802	975
4	⁶ LiF	L-698	1000
4	⁶ LiF	L-681	1030
4	⁷ LiF	L7-112	1015
4	⁷ LiF	L7-142	1030
4	Ionization chamber	00004	750
5	CaF (shielded)	G-486	1035
5	CaF	G-487	1025
5	⁶ LiF	L-674	960
5	⁶ LiF	L-677	1050
5	⁷ LiF	L-713	1045
5	⁷ LiF	L-715	1070
5	Ionization chamber	000019	820

Table 4

THERMOLUMINESCENT MEAN DOSE VERSUS SPACECRAFT LOCATION

<u>Spacecraft location</u>	<u>Mean thermolumi- nescent dose (millirads)</u>
1	1617
2	1125
3	1278
4	1010
5	1030

Table 5

CALCIUM-FLUORIDE DOSE LEVELS VERSUS SPACECRAFT LOCATION

<u>Spacecraft location</u>	<u>CaF shielded dose (millirads)</u>	<u>CaF unshielded dose (millirads)</u>
1	1595	1640
2	1105	1130
3	1355	1305
4	1000	975
5	1035	1025

neutron contribution to dose over the range of 0.025 eV to 10 keV. Previous estimates in the literature had predicted from 0.5 to 10 percent neutron contributions to dose from the entire spectrum of secondary neutrons produced by nuclear collisions at shielding thicknesses ranging from 10 g/cm² to 50 g/cm². It would appear from the ⁶LiF/⁷LiF differential measurements that the secondary neutrons are confined to higher energies.

The quartz-fiber discharge ionization chambers provided the measurements at the passive dosimeter locations as shown in table 6.

Table 6

QUARTZ-FIBER IONIZATION CHAMBER DOSE READINGS

<u>Spacecraft location</u>	<u>Dose level (millirads)</u>	<u>Thermoluminescent dosimeter/ionization chamber dose ratio</u>
1	1210	1.34
2	870	1.29
3	950	1.35
4	750	1.35
5	820	1.26

The readings by the discharge ionization chambers were lower by an average of 1.32 than the thermoluminescent devices. The relative constancy of the thermoluminescent dosimeter to ionization chamber dose ratios indicates that the lower ionization chamber readings are primarily a result of the greater inherent shielding of the ionization chambers and their underresponse to energetic protons. The ionization chambers have approximately 0.4 g/cm² aluminum shielding versus 0.15 g/cm² aluminum equivalent shielding for the thermoluminescent dosimeters.

The gold and iridium foils showed no measurable neutron fluence. Their resultant readings agree with the thermoluminescent dosimeter ⁶LiF/⁷LiF measurements. The detection threshold for fast neutron activation of the iridium foils is less than 10³ n/cm² for neutron energies above 10 keV. Since the half life for the activation processes is approximately 80 days, about 10³ n/cm² may be considered as an upper limit on the energetic neutron dose produced in Skylab. The fluence threshold for thermal neutrons for the 30-day

mission was established at less than 10^3 n/cm² by the gold-foil measurements, since this represents the lower fluence detectability threshold.

The passive dosimetry measurements reported here for Skylab II show a direct dependence on the shielding between the naturally occurring space-radiation environment and the onboard-radiation sources and the various sensing elements. The complex shielding distributions about each of the five passive dosimeter containers are shown in figure 46. The shielding in all cases is sufficiently thick so that the geomagnetically trapped electrons are almost entirely absorbed by the Skylab II spacecraft (ref. 20). The radiation levels recorded by the Skylab passive dosimeters consist principally of penetrating protons with lesser contributions from alpha particles, higher Z-charged particles, and bremsstrahlung X-rays. The accumulated spectral distribution by particle type and energy will be determined from the film emulsion and heavy particle track detector analysis. Based on earlier Apollo CSM film-emulsion measurements (ref. 21), the dose is estimated to consist of 90 percent protons, with the other constituents mentioned comprising the remaining dose.

The quality factor of radiation in the Skylab II, based on earlier Apollo command module measurements (ref. 21), should range from 1.5 to 2.0.

The dose levels based on active dosimeter ionization chamber and spectrometer measurements in the Skylab II were accumulated chiefly in the South Atlantic anomaly. These trapped radiation account for 90 percent of the total rad dose reported in this paper. Cosmic rays comprise the remainder of the naturally occurring dose. In no cases did passive dosimeter packages located at greater spacecraft shielding record larger doses than more lightly shielded units. This confirms previous measurements (ref. 4) in which no dose buildup with increased shielding was found. These agree with the preflight measurements at the five passive dosimeter locations.

One of the principal objectives of the Skylab II experiment D008 was to establish an empirical test of existing space-radiation transport and shielding codes used for future mission planning. Initial comparisons (ref. 22) were made by using the Lockheed-developed space shielding codes and the passive dosimetry total dose measurements. Remarkable agreement was found using the shielding codes and the final thermoluminescent total doses at each of the five Skylab II locations. Table 7 shows the results of this comparison.

Table 7

COMPARISON OF PASSIVE DOSIMETER TLD MEASUREMENTS AND LOCKHEED
SPACE SHIELDING CODE THEORETICAL DOSE COMPUTATIONS

<u>Spacecraft location</u>	<u>Calculated dose, rads</u>	<u>Average TLD dose, rads</u>	<u>CaF TLD, rads</u>		<u>LiF TLD, rads</u>
			<u>Shielded</u>	<u>Unshielded</u>	
1	1.850	1.613	1.595	1.640	1.611
2	1.177	1.122	1.105	1.130	1.124
3	1.314	1.291	1.355	1.305	1.271
4	1.438	1.008	1.000	0.975	1.019
5	1.154	1.031	1.035	1.025	1.031

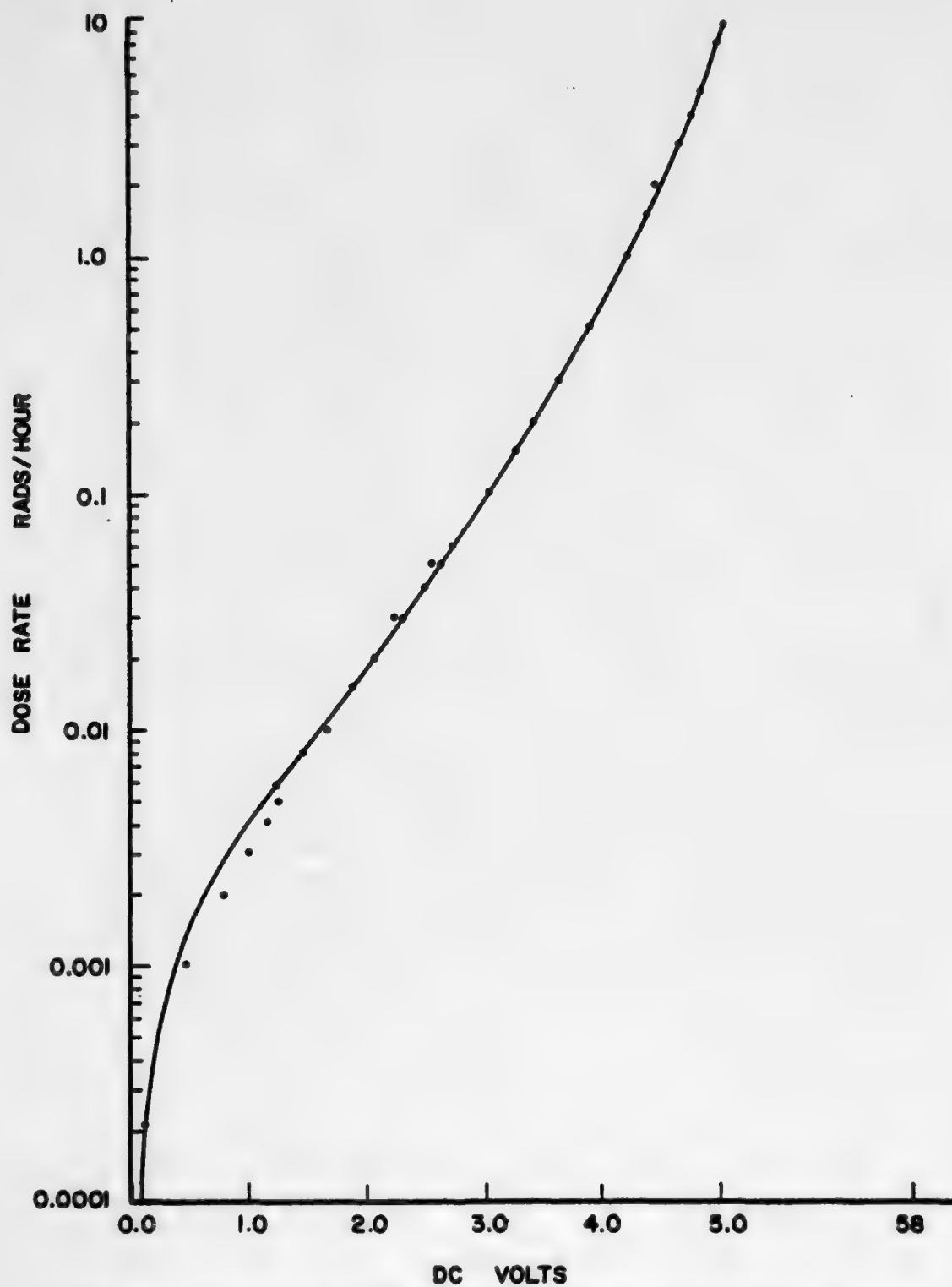


Figure 29. Tissue-Equivalent Ionization Chamber Calibration Data

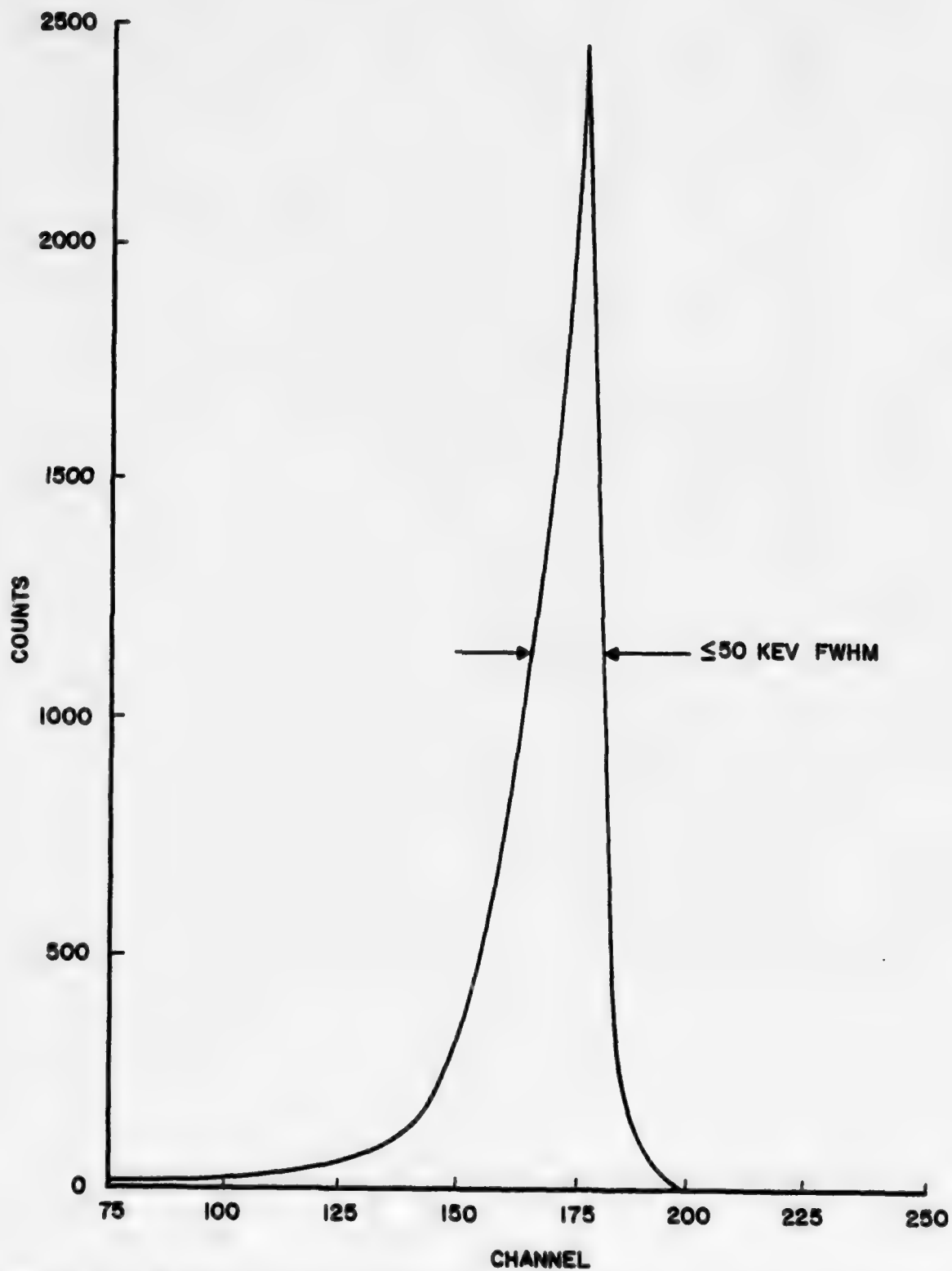


Figure 30. Americium-241, 5.476-MeV Alpha Particle Spectrum, Entrance Detector

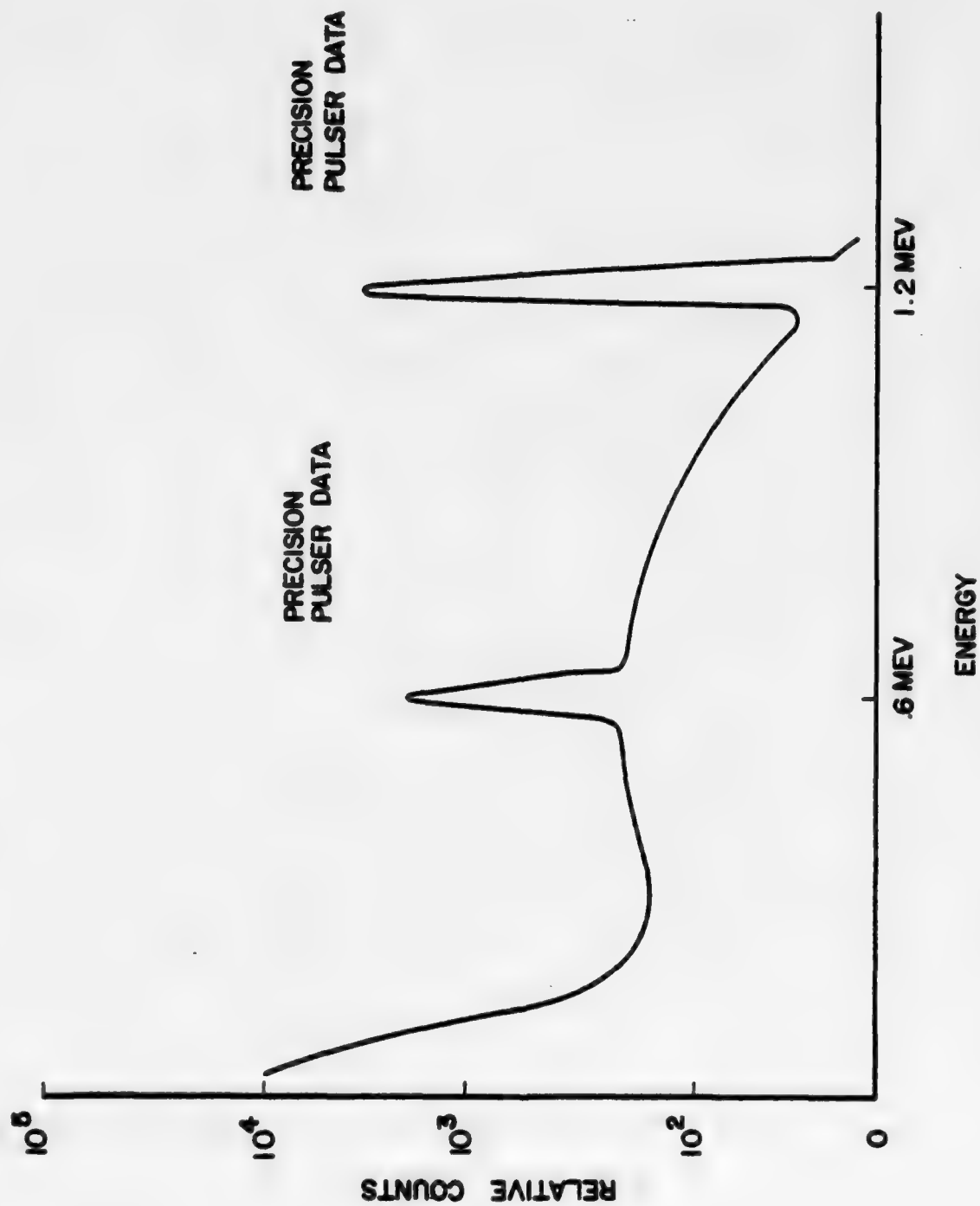
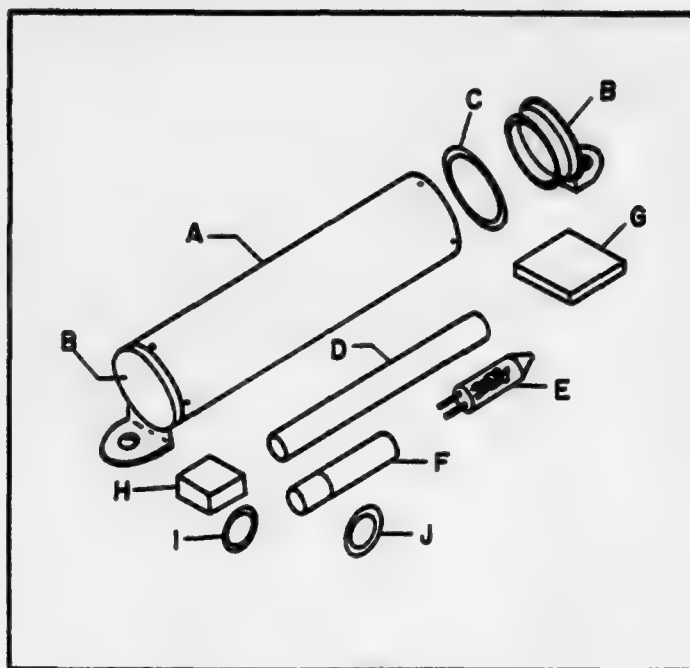


Figure 31. Anticoincident Detector Sr-90 Spectrum



- A. Aluminum dosimeter unit housing
- B. Aluminum dosimeter unit housing end plate
- C. Teflon seal
- D. Ionization chamber, pocket dosimeter
- E. Thermoluminescent dosimeter
- F. Thermoluminescent dosimeter shield
- G. Polymer dosimeter
- H. Nuclear emulsion dosimeters (types K-2 and G-5)
- I. Gold foil
- J. Iridium foil

Figure 32. Complete Dosimeter Unit (Graphic Anatomy)

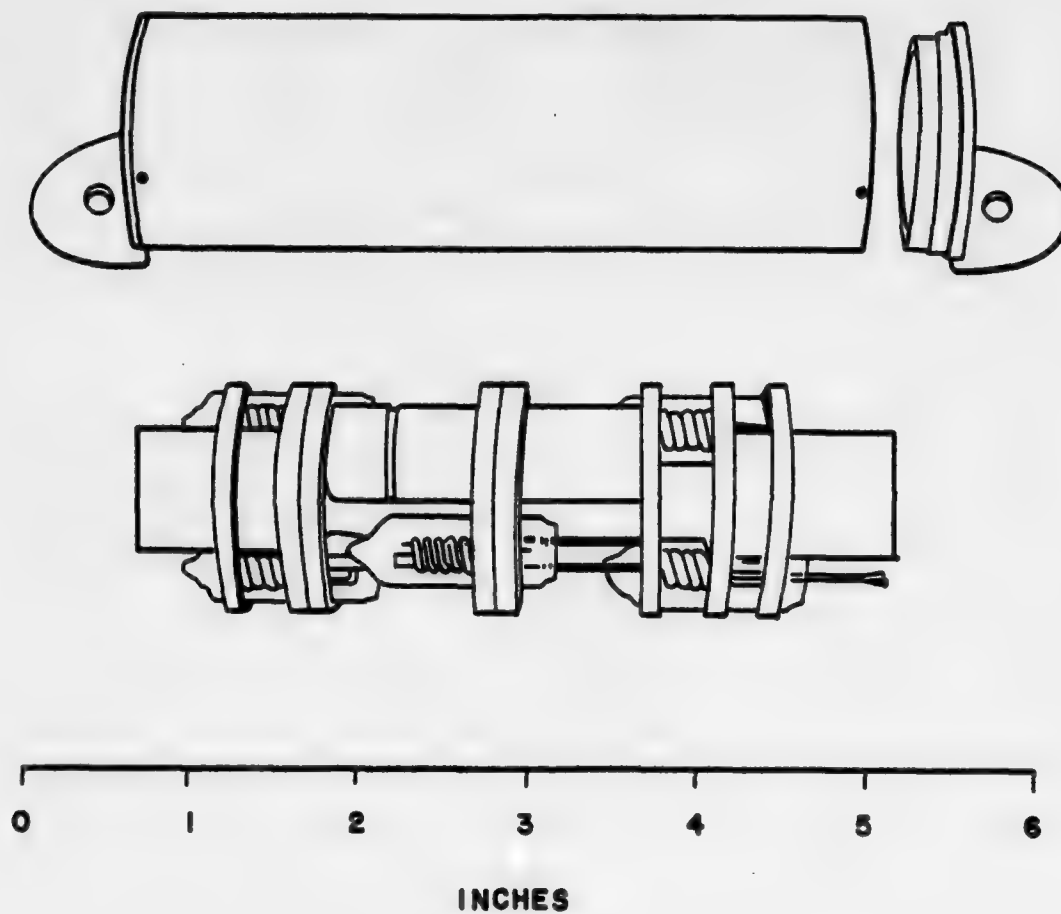


Figure 33. Passive Dosimeters Mounting Package

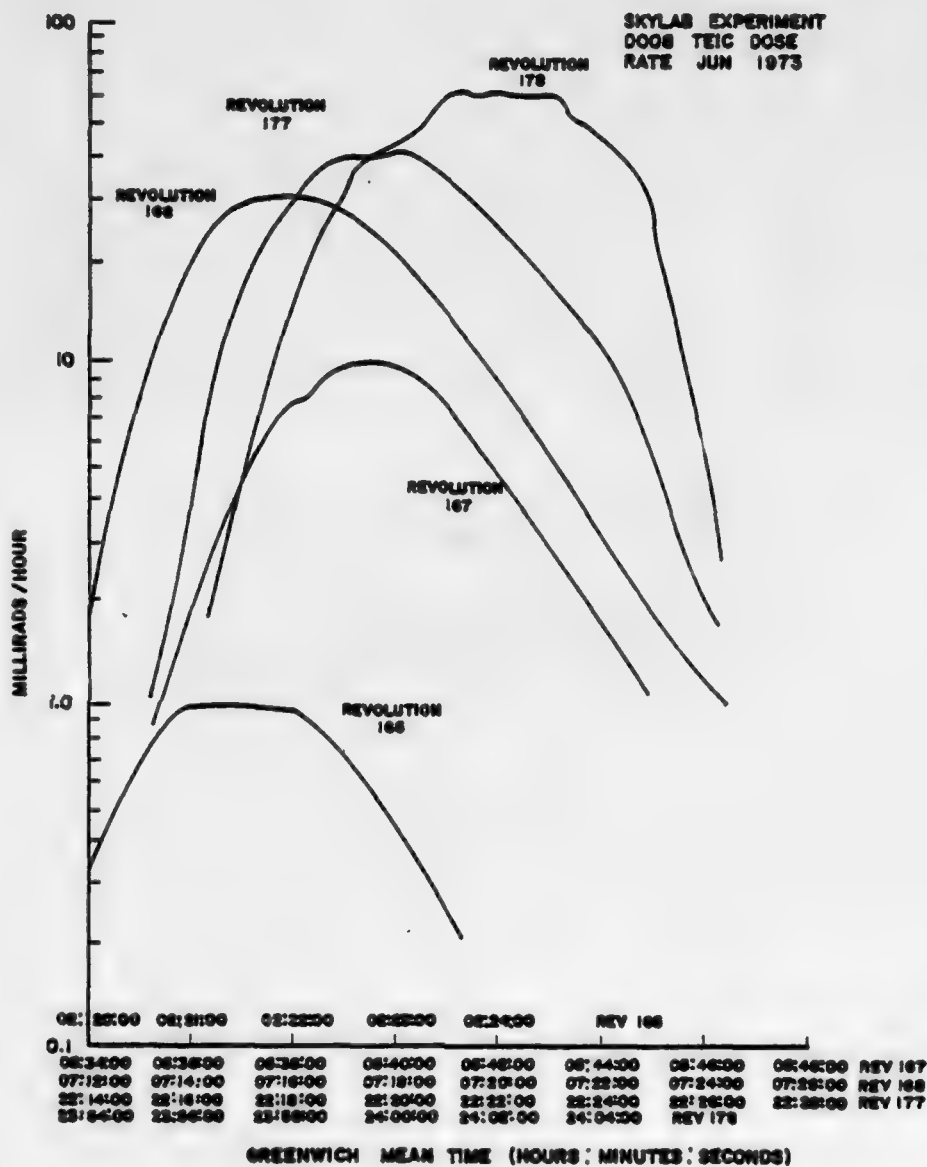


Figure 34. South Atlantic Anomaly Series of Revolutions

SKYLAB EXPERIMENT
DOOS TEIC DOSE
RATES JUN 1973

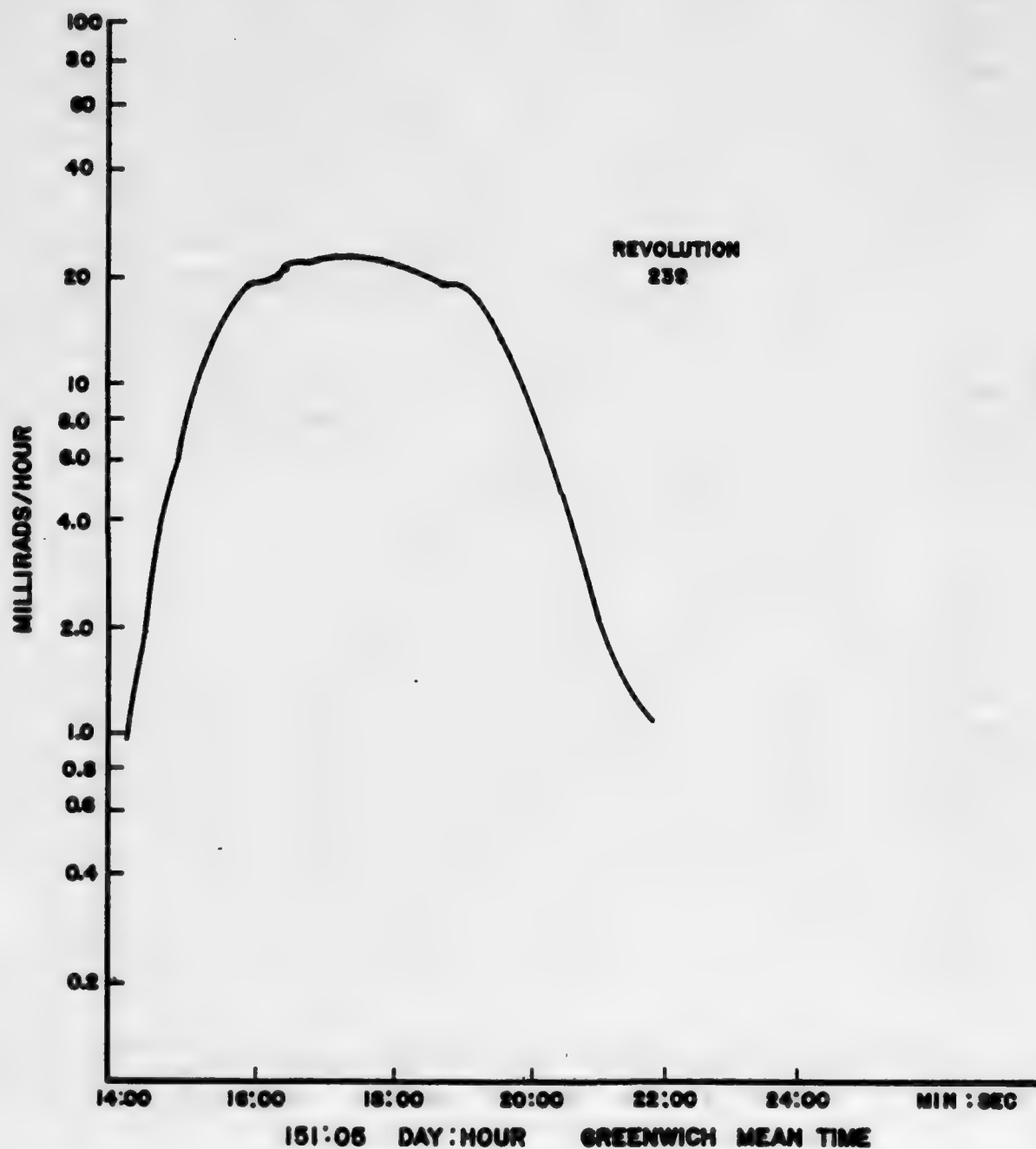


Figure 35. Active Dosimeter South Atlantic Anomaly Dose Rates

SKYLAB EXPERIMENT
DOOS TEIC DOSE
RATES JUN 1973

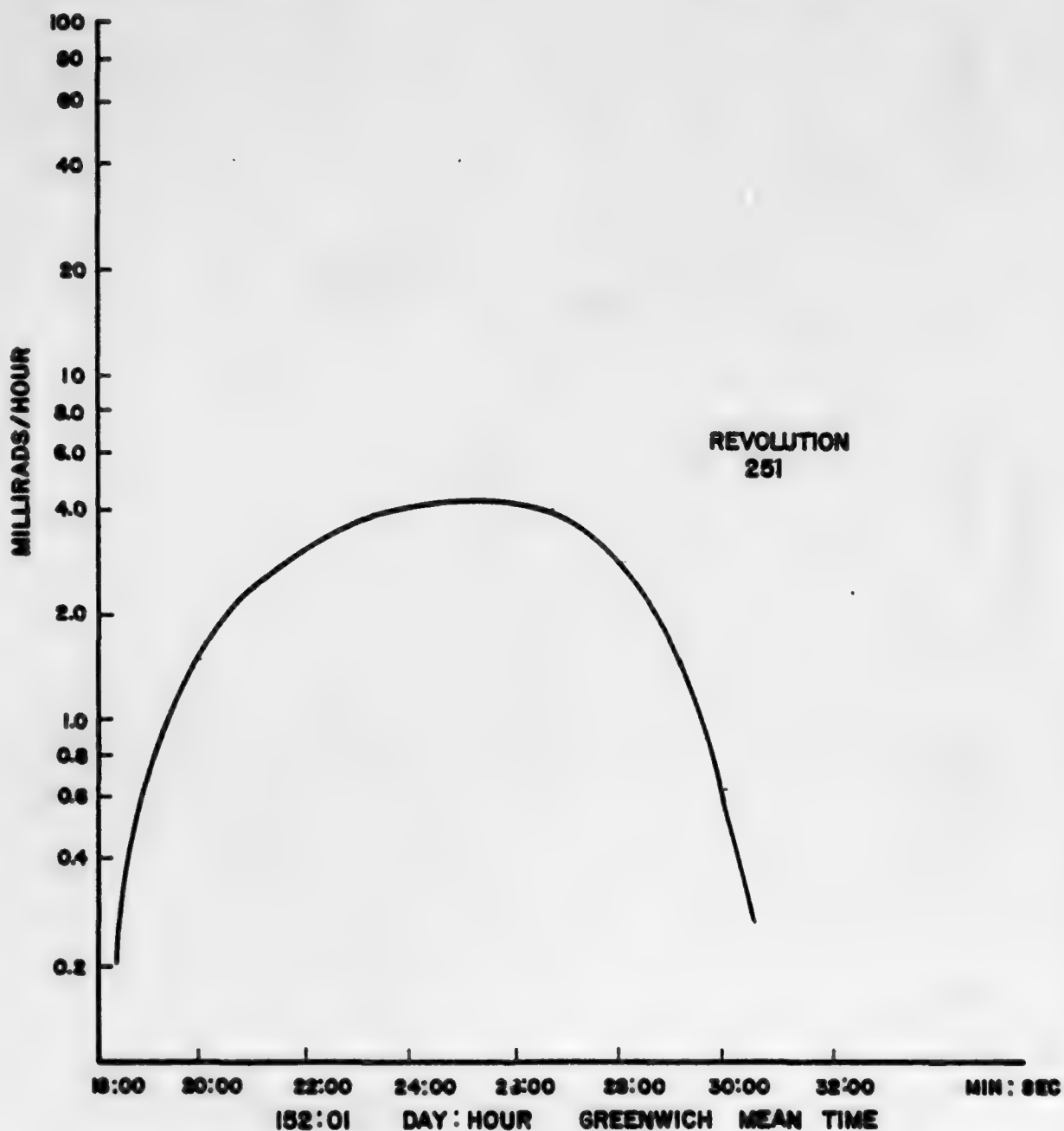


Figure 36. Active Dosimeter South Atlantic Anomaly Dose Rates

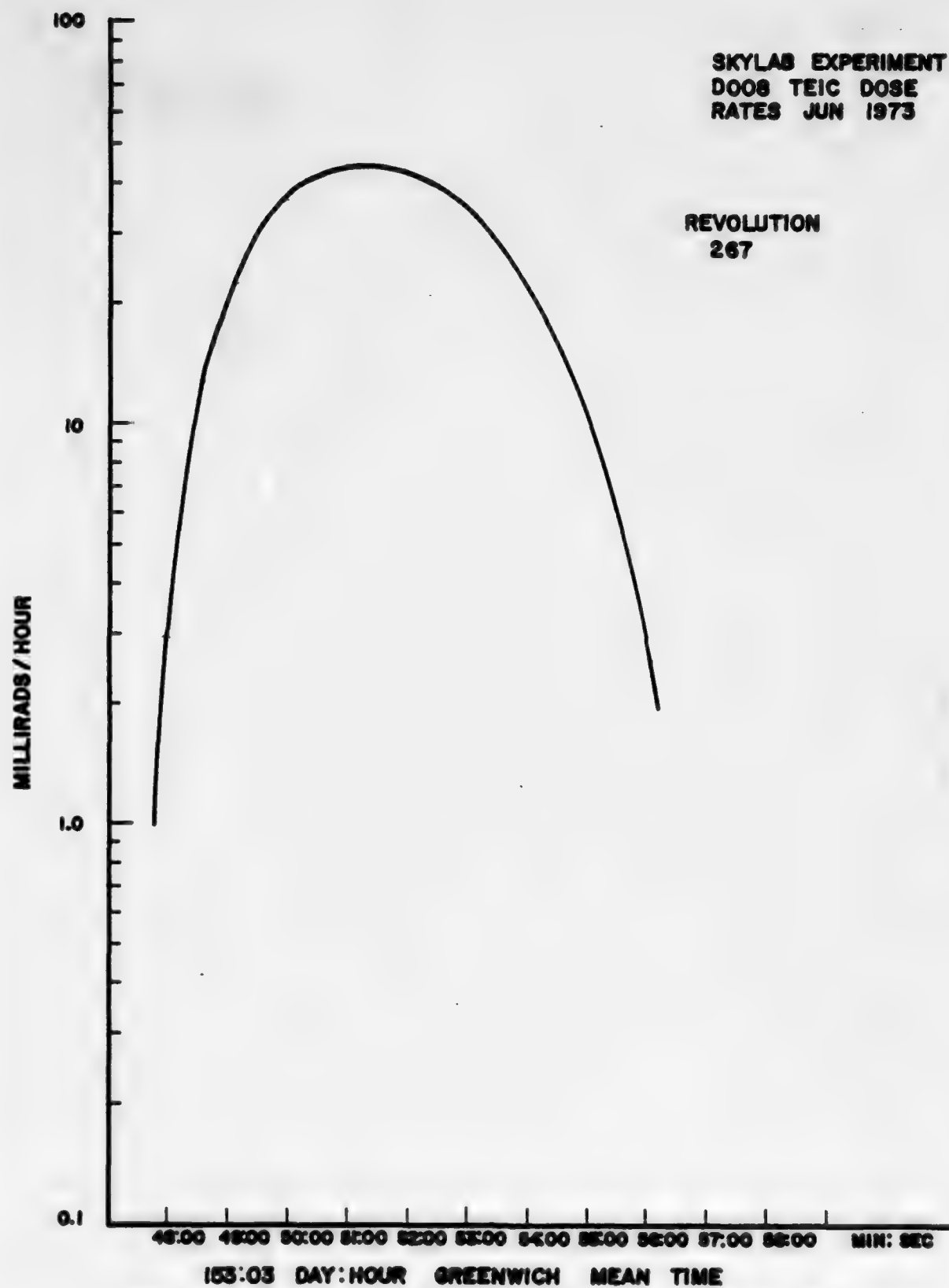


Figure 37. Active Dosimeter South Atlantic Anomaly Dose Rates

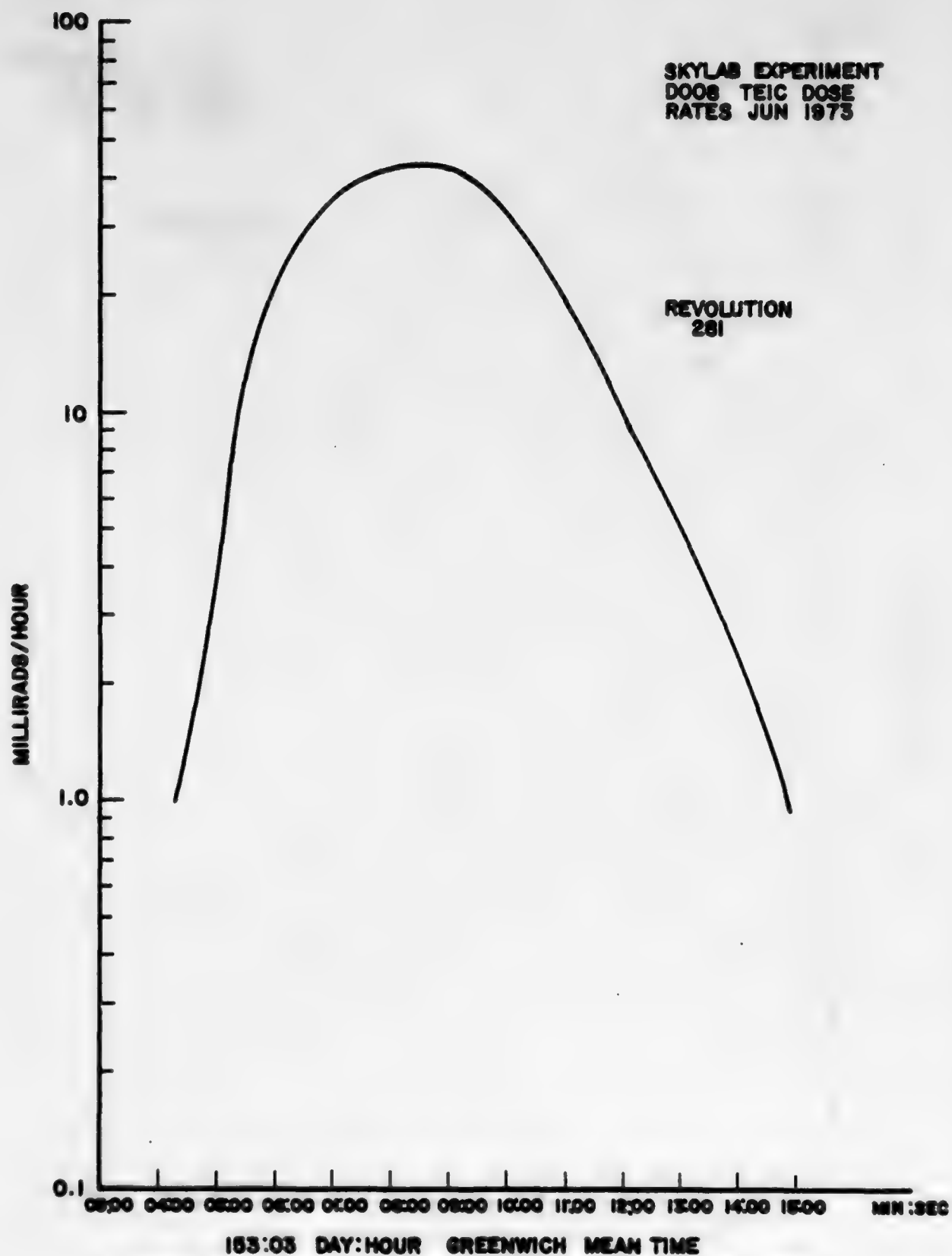


Figure 38. Active Dosimeter South Atlantic Anomaly Dose Rates

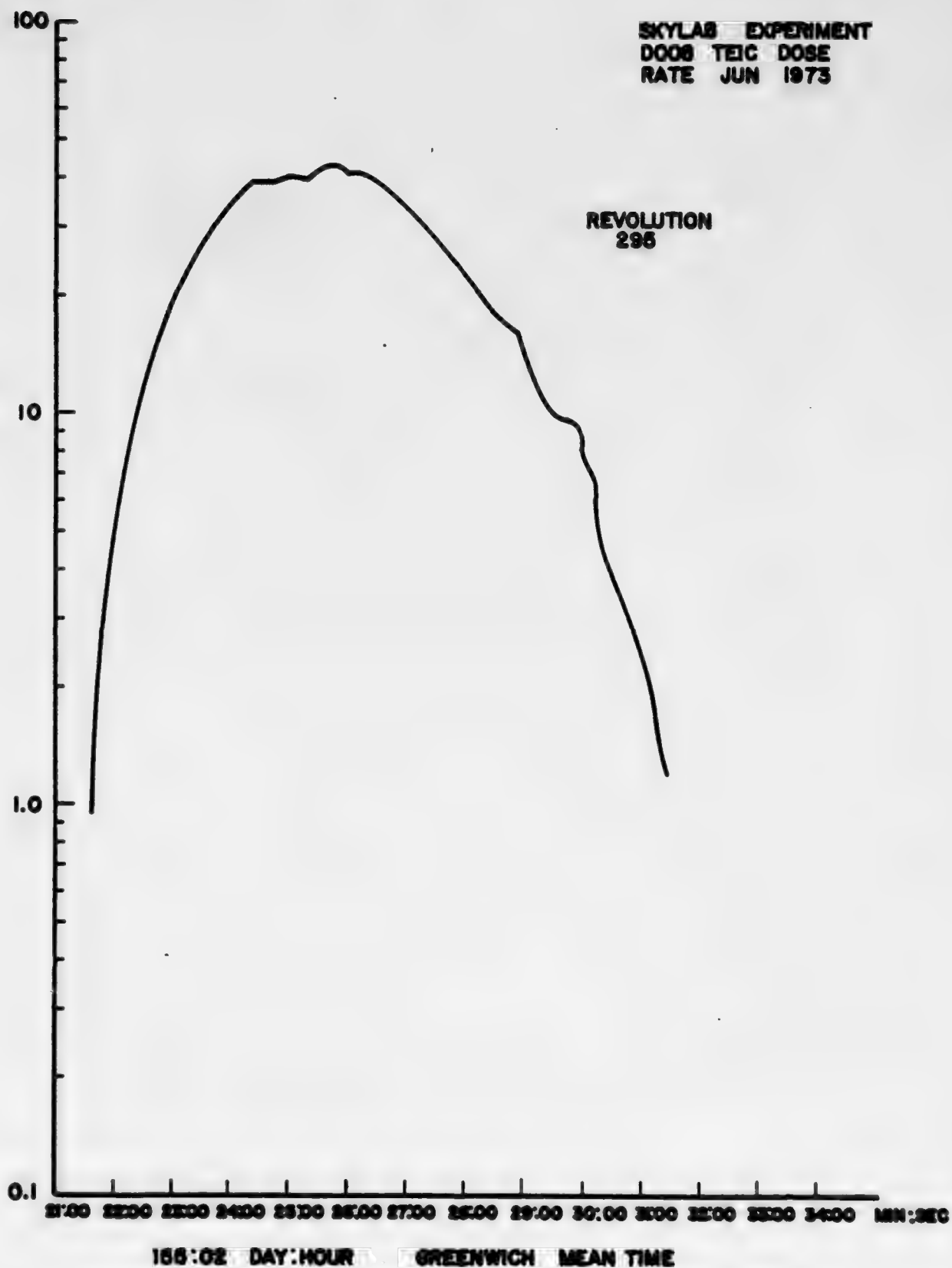


Figure 39. Active Dosimeter South Atlantic Anomaly Dose Rates

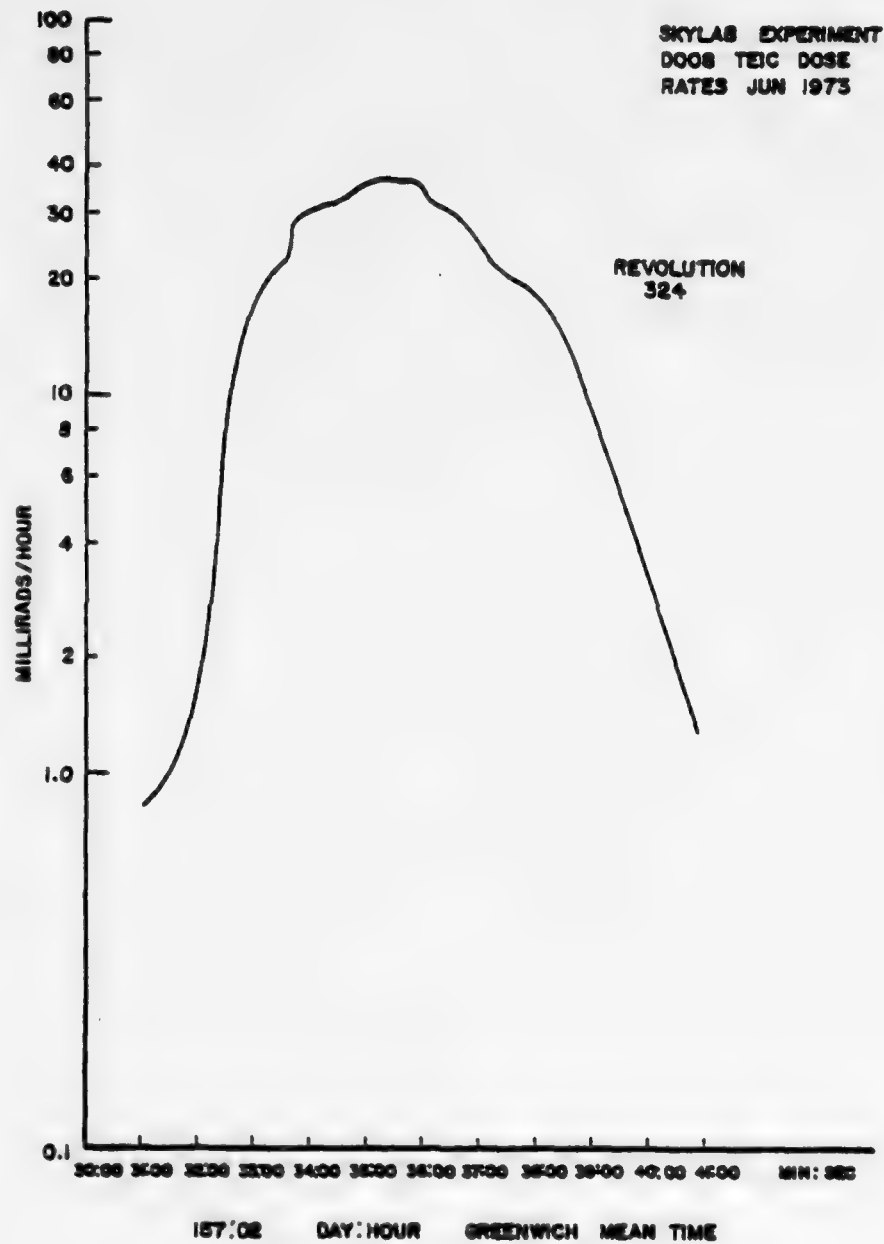


Figure 40. Active Dosimeter South Atlantic Anomaly Dose Rates

SKYLAB EXPERIMENT
DOOS TEIC DOSE
RATES JUN 1973

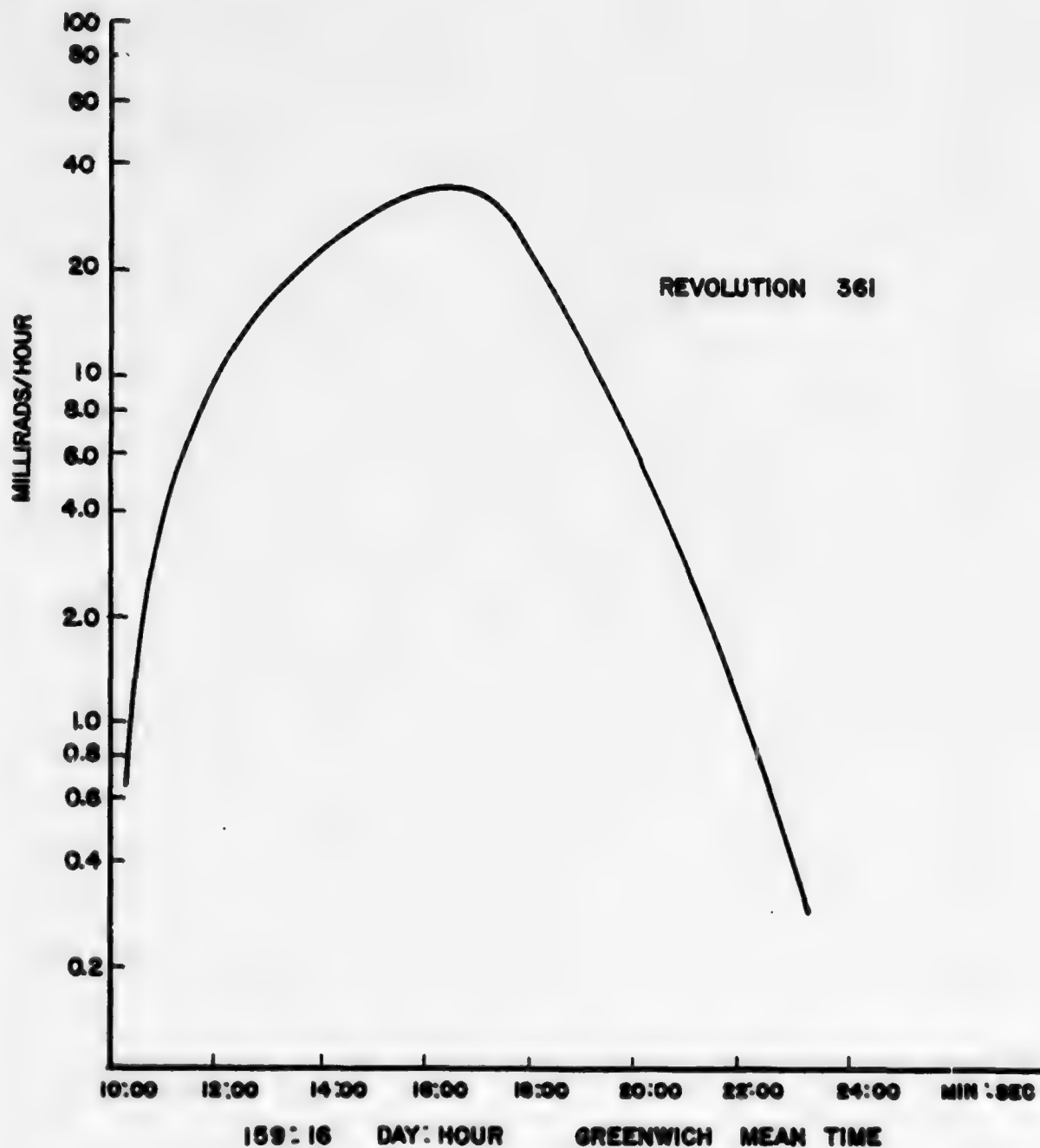


Figure 41. Active Dosimeter South Atlantic Anomaly Dose Rates

SKYLAB EXPERIMENT
DOOS TEIC DOSE
RATES JUN 1973

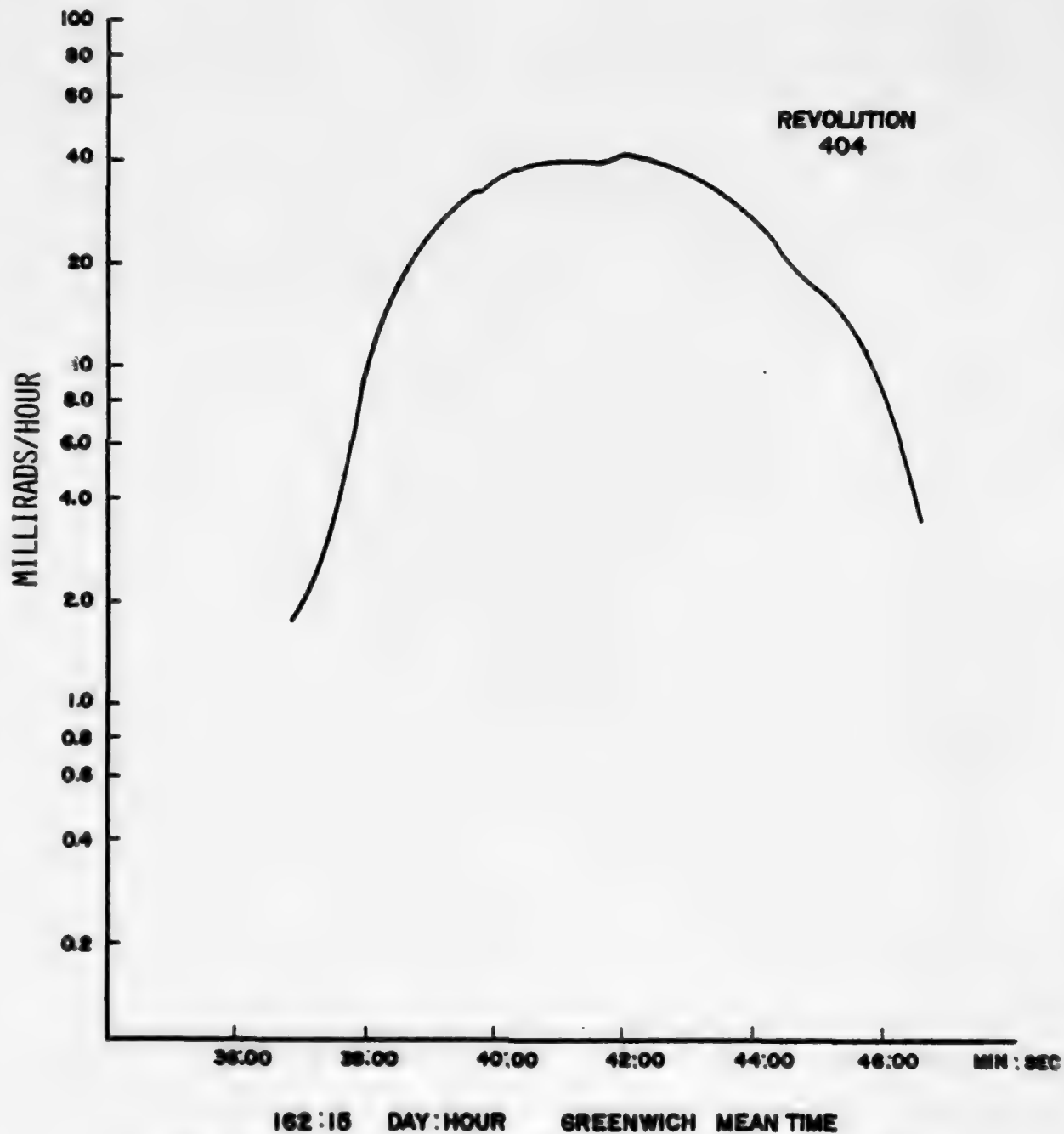


Figure 42. Active Dosimeter South Atlantic Anomaly Dose Rates

SKYLAB EXPERIMENT
DOOS TEIC DOSE
RATES JUN 1973

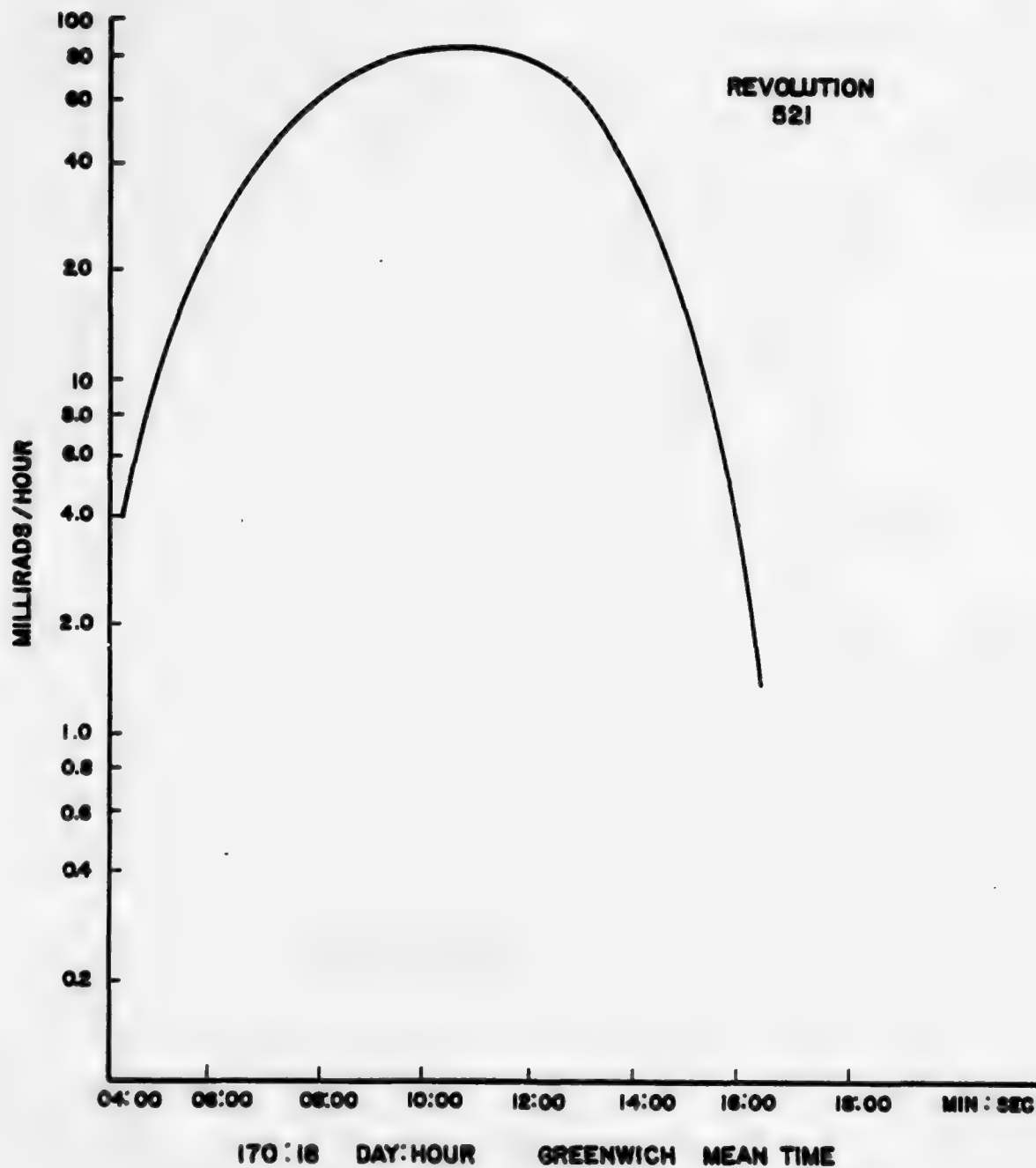
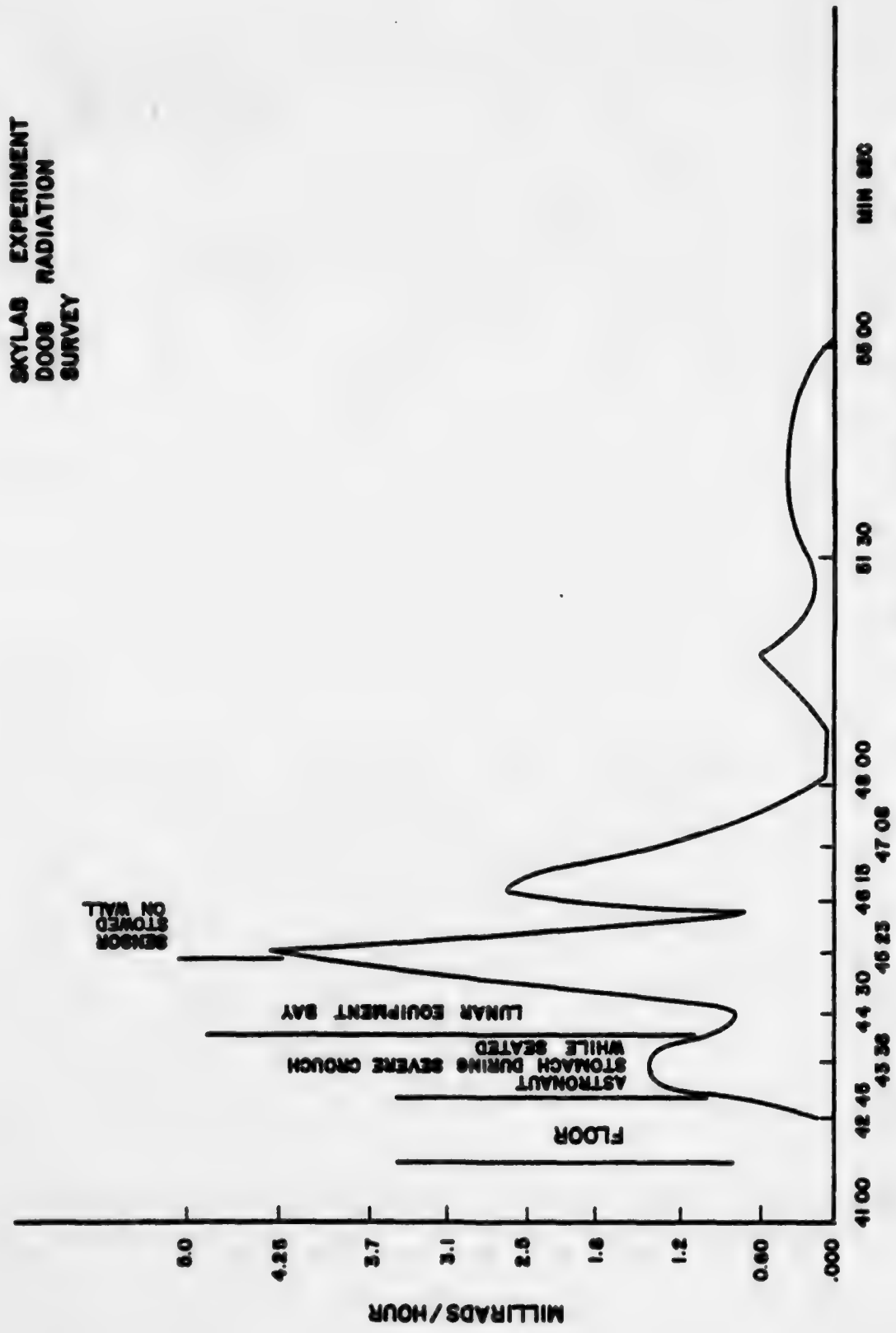


Figure 43. Active Dosimeter South Atlantic Anomaly Dose Rates

SKYLAB EXPERIMENT
DOOS RADIATION
SURVEY



169 10 DAY HOUR GREENWICH MEAN TIME
Figure 44. Astronaut Radiation Survey in Skylab II

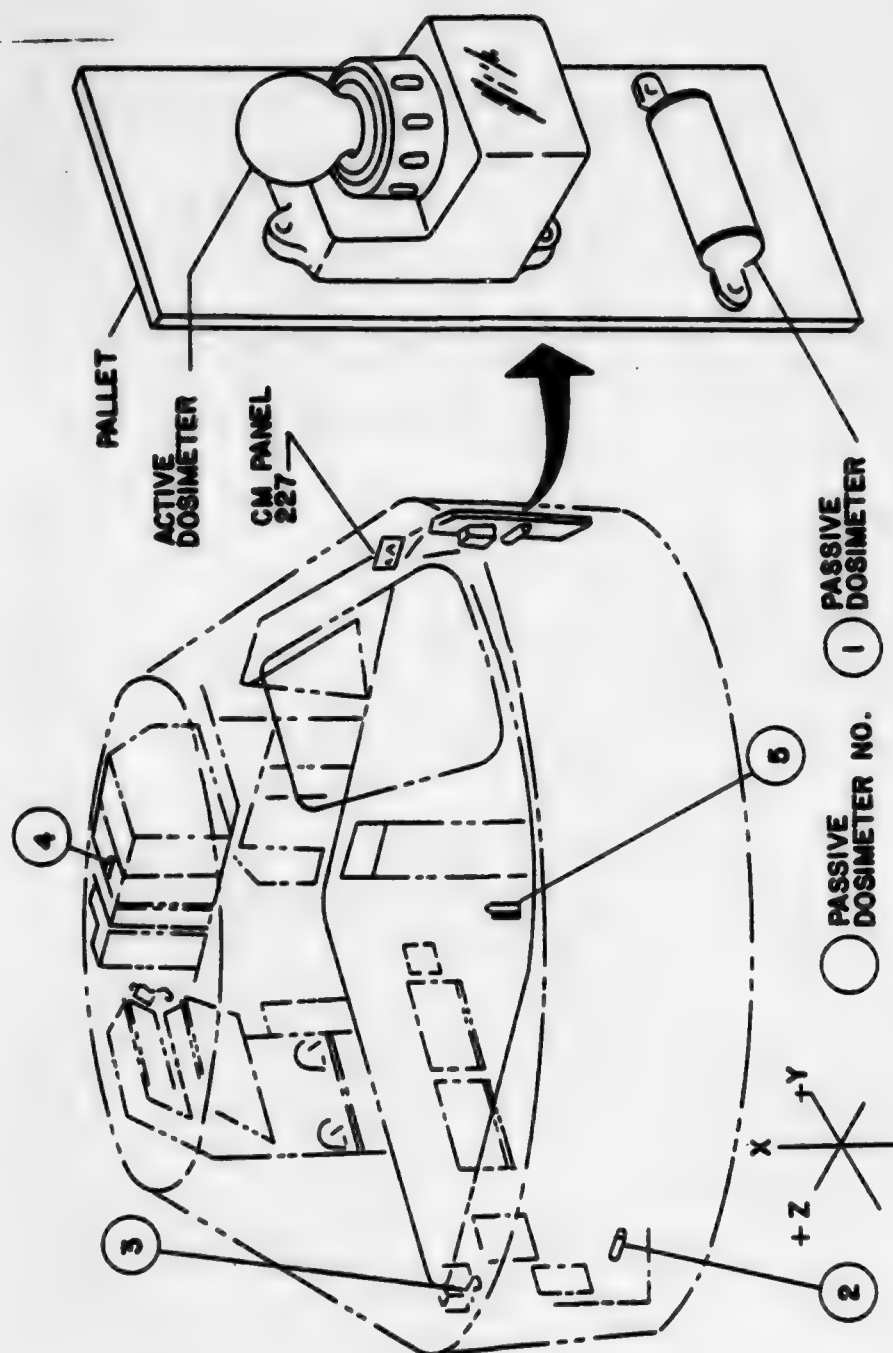


Figure 45. Command Module (Skylab II) Indicating Five Mounting Locations for D008 Radiation

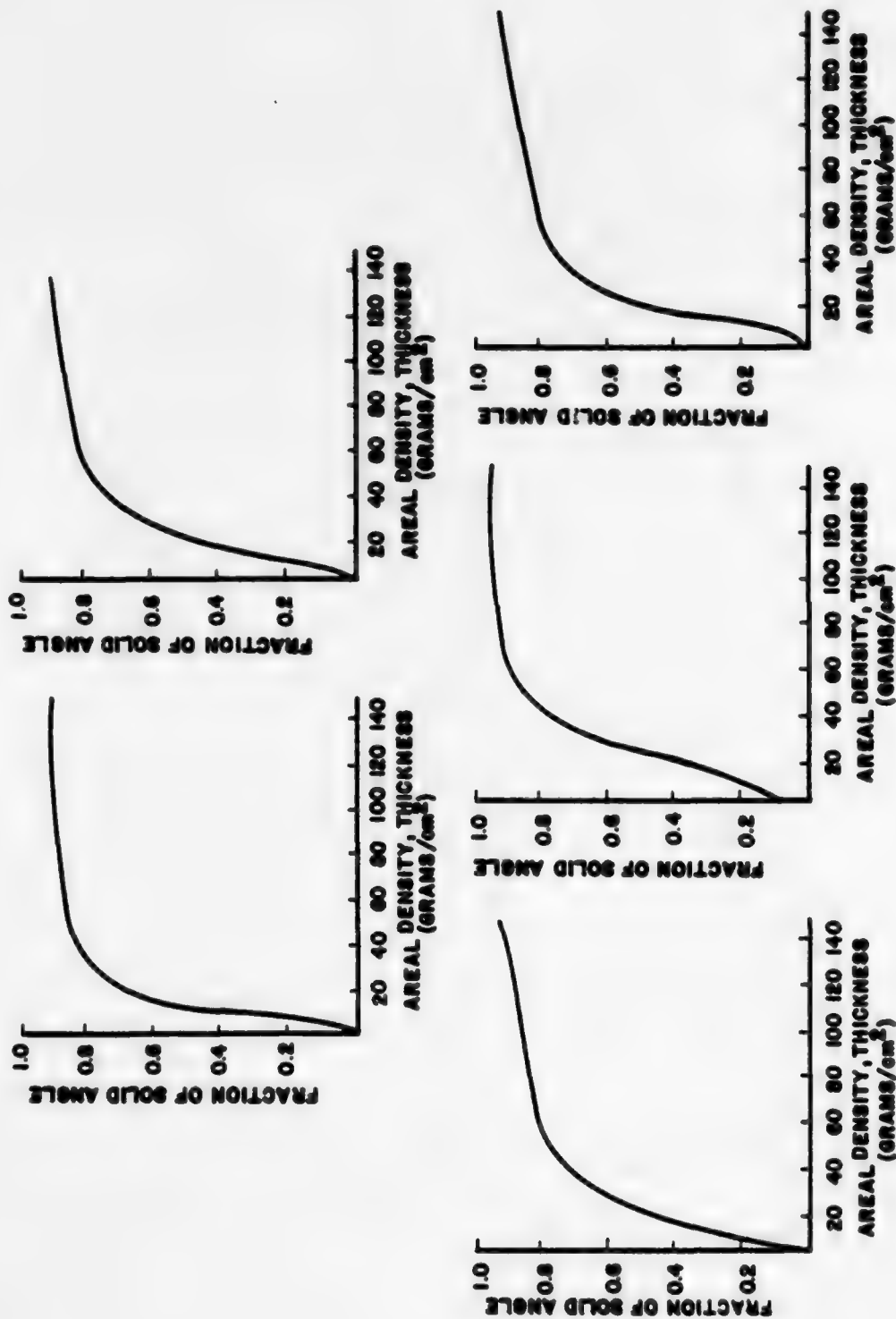


Figure 46. Shielding Distributions for the Five Passive Units

SECTION VII

CONCLUSIONS

Both active and passive dosimetry systems functioned as planned for the Skylab II. The astronaut use of the active dosimeter proved the sensor design in space was practical. The systems survived all launch and thermal environments without any degradation of performance. Initial analysis of the active dosimetry data has proven their effectiveness in measuring mixed fields of radiation. The following observations were established by the Skylab II active dosimeter measurements.

a. Dose rates of 100 millirad/hour occurred in the South Atlantic anomaly at Skylab altitudes and orbits.

b. Radiation levels in the millirad/hour range occurred for up to 20 minutes on the deepest anomaly passes.

c. Particle spectrometer data from the LET sensor confirms other measurements (externally flown electron/proton spectrometer, film emulsion, and computer code predictions) which indicated that the trapped particle dose is primarily from protons.

d. The RBE for a limited number of South Atlantic anomaly revolutions varies from 1.5 to 2. Refinements of the active dosimeter LET data, especially in the low energy $0.5 < E_p < 2.5$ MeV channel, must be performed using film-emulsion data which is being processed.

e. Outer zone trapped electron doses in the Skylab II are very small.

The passive dosimetry results provide the following conclusive observations.

a. The peak integrated doses measured onboard Skylab II at the location of minimum shielding lead to average daily exposures of 50 millirad. This compares with doses of 16 millirad/day on the Gemini 4 flights (ref. 4) at lower altitudes (180 nm versus 235 nm) and 30° versus 55° inclinations. The Skylab II dose levels clearly show the effect of increased altitude and inclination. This is even more pronounced when one considers that the 1964 Gemini doses were obtained behind considerably lighter shielding and include the

AFWL-TR-73-222

effects of artificial electrons which contributed significantly (>30 percent) to the total dose. Artificial electrons have decayed to negligible levels for the Skylab mission (ref. 23).

b. The dose projection for the 2-month Skylab III mission is 3.2 rads for operations in the command module. The workshop doses would be higher (approximately 4 rads) and a corresponding maximum of 8.0 rem for the 2-month mission.

c. The measurements presented in this report were not influenced by solar flare particles because no major solar flare particle events in the vicinity of the earth were observed in the Skylab I/II mission. Solar particles in the equatorial portions of the Skylab orbit would be largely shielded by the earth's magnetosphere except for short-time exposures at the highest latitudes. This shielding should be sufficient to prevent any hazardous radiation levels to the astronauts even from the largest particle events. Polar-orbiting manned satellites would, of course, be subject to high fluences of solar particles. Manned missions operating at higher altitudes even in equatorial orbits for extended periods would accumulate significant exposures. Practicable shielding does not reduce the exposure levels by significant amounts due to the high energy of the trapped proton component of the space radiation environment. It would appear that the only alternative to considerably higher altitude manned operations will be careful monitoring of the radiation environment and limitations enforced on the orbital times of the astronauts.

REFERENCES

1. Taylor, L. S., International Commission on Radiation Units Report II, p 3, Wash, DC, 1968.
2. "Physical Aspects of Irradiation," National Bureau of Standards Handbook 85, p 105, March 1964.
3. Langham, W., "Biological Effects of Ionizing Radiation," Chs. I, II, and III, Aerospace Medicine, Vol 36, No. 2, 1965.
4. Schneider, M. F., et al., "Experiment D-8, Radiation in Spacecraft, Gemini 4," First Manned Spaceflight Symposium, p 171, Wash, DC, 1965.
5. Langham, W., "Biological Effects of Ionizing Radiation," Ch. III, Aerospace Medicine, Vol 36, No. 2, p 32, 1965.
6. Scott, W. W., Estimates of Primary and Secondary Particle Doses Behind Aluminum and Polyethylene Slabs Due to Incident Solar Flare and Van Allen Belt Protons, RSIC-18, Oak Ridge National Laboratory, TN, July 1967.
7. United States National Radiation Protection Subcommittee, M-4 Report, 1967.
8. Attix, F. H., Roesch, W. C., Radiation Dosimetry, pp 340-341, Academic Press, New York, 1968.
9. Spencer, L. V., Attix, F. H., "A Theory of Cavity Ionization," Radiation Res., 3:239, 1955.
10. Shonka, F. R., et al., Proceedings of the Second United Nations International Conference on the Peaceful Uses of Atomic Energy, 21, p 184, 1958.
11. "Report of the International Commission on Radiological Units and Measurements (ICRU)," National Bureau of Standards Handbook 78, 1959.
12. Janni, J. F., Proton Absorption in Dose Equated Materials, AFWL-TR-65-3, Air Force Weapons Laboratory, Kirtland AFB, NM, 1965.
13. Flugge, S., Handbuch Der Physik, Vol 45, Sec. 5, pp 9-16, 1958.
14. Starodubtsev and Romanov, The Passage of Charged Particles Through Matter, United States Atomic Energy Commission Translation, T.R. 6468, pp 203-206, 1965.
15. Rossi, H. H., Rosenzweig, O., Radiology, 64, No. 3, pp 290-299, March 1955.
16. Janni, J. F., Calculations of Energy Loss, Range, Pathlength Straggling, Multiple Scattering, and the Probability of Inelastic Nuclear Collisions for 0.1 to 1000 MeV Protons, AFWL-TR-65-150, Air Force Weapons Laboratory, Kirtland AFB, NM, September 1966.
17. Durkee, R. K., et al., Energy and Rate Dependence Studies, EG&G Technical Report S-237-R.

18. Murphy, H. M., Summary of Neutron and Gamma Dosimetry Techniques, AFWL-TR-66-111, Air Force Weapons Laboratory, Kirtland AFB, NM, 1967.
19. Lederer, C. M., Holtaucen, J. M., Perlman, I., Table of Isotopes (Sixth Edition), John Wiley & Sons, Inc., New York, 1967.
20. Hopkins, Keith, Private Communications on Results of Dose Calculations Using the SPARES Radiation Codes, March 1970.
21. Schaefer, H. J., Sullivan, J., Nuclear Emulsion Measurements of the Astronauts Radiation Exposure on Apollo VII, NAMI-1060, Naval Aerospace Medical Institute, February 1969.
22. Hardy, A., Beaver, R., Leffler, J., Atwell, W., Hopkins, K., Skylab Radiation Analysis, SL 1/2 Report (Private Communications), July 1973.
23. Singley, G., Vette, J., The AE-4 Model of the Outer Radiation Zone Electron Environment, NSS-DC-72-06, NASA Goddard Spaceflight Center, August 1972.
24. Fortney, R., TRW Systems, Redondo Beach, CA, Private Communications, 1969.

APPENDIX

LINEAR ENERGY TRANSFER SPECTROMETER SENSOR DESIGN CONSIDERATIONS

A number of important factors influence the design of proton and alpha particle telescopes like those used in the LET sensors described in this report. A unified approach to the analysis of a number of these factors has been proposed by Fortney (ref. 24). These are described and analyzed as follows:

- a. Anticipated count rate
- b. Geometry of the collimator and the size of the second (anticoincidence) detector
- c. Energy variation with angle of incidence for particles which are just stopped in the detector
- d. Leakage of high energy protons through the side shielding
- e. Data contamination from other radiation (electrons, bremsstrahlung, and galactic cosmic rays)

1. ANTICIPATED COUNT RATE

Available Van Allen Belt trapped proton data ordered according to the McIlwain B and L parameters indicate that the proton flux will be most intense in the regions of the South Atlantic geomagnetic anomaly and that the peak intensity will occur at 45°W longitude between 20° and 25°S latitude for an altitude of 500 km. The B and L parameters for this region of space are approximately $L = 1.20$ and $B = 0.20$. Integral and differential proton flux-energy data are presented for this peak region in figures 47 and 48, respectively. The Air Force Weapons Laboratory's FESS satellite data were used to calculate the curves in figure 49 of proton spectra after penetrating various thicknesses of material. Table 8 gives the total omnidirectional flux penetrating the indicated thicknesses of aluminum with specified residual energies.

The actual count rate per channel will be at most one-fourth the corresponding omnidirectional value given in table 8, depending on the degree of collimation of the LET sensor. The factor of one-fourth is valid in that only

Table 8

OMNIDIRECTIONAL PROTON FLUX (protons/cm² sec) AT B = 0.20 AND L = 1.20
WHICH FALL IN GIVEN ENERGY RANGES AFTER PENETRATING SHIELDING

Residual energies (MeV)	Shield thicknesses (gm/cm ² Al)			
	<u>1.0</u>	<u>$\sqrt{2}$</u>	<u>2.0</u>	<u>$2\sqrt{2}$</u>
0.5 - 2	1.77	1.38	1.07	0.84
2 - 6	6.96	5.42	4.22	3.32
6 - 10	19.75	15.40	11.97	9.40
10 - 14	21.80	17.00	13.21	10.40
14 - 18.5	29.50	23.00	17.90	14.05
0.5 - 18.5	79.80	62.20	48.37	38.01

one-half the omnidirectional flux is intercepted from a given 2π steradians and that only one-half of that radiation (assuming isotropy) will penetrate the given 1 cm² of the detector. These considerations lead to the following two important results:

a. The total LET count rate ($E < 18.5$) will be less than 10 to 20 counts per second, depending on shielding and collimation.

b. The lowest energy channel (highest LET) will experience a count rate less than 0.2 to 0.5 counts per second.

Because of the relatively low count rate in the lowest energy channel, care must be exercised to prevent any contamination of this channel. Also, the low count rates make it mandatory for the LET electronics to have a capability of recording single events in all channels.

2. COLLIMATOR GEOMETRY

Although the solid angle of the collimator and the area of the first detector determine the LET count rates, the view permitted by the collimator must not allow particles to penetrate the first detector and miss the second detector. Assuming a first detector with 1-cm² surface area and 2-mm sensitive depth and a 2.8-cm² x 1-mm second detector, the maximum angle of incidence from the normal at which a particle can penetrate the first detector at the edge and still be rejected by the second detector can be obtained in the manner

shown in figure 50. Assuming that the 0.118-cm path length required for a 1-MeV proton to deposit 0.5 MeV in silicon in the first detector is equal to the 0.095-cm path length required for 0.4 MeV in the second, the maximum angle of incidence is $\tan^{-1} (0.35/0.2)$ or 60° . This is important because the 250- to 600-proton/cm²/sec monodirectional proton flux > 55 MeV is much greater than the 1-proton/cm²/sec, $0.5 < E < 18.5$ MeV penetration flux given in table 8. It should be noted that these unwanted counts can occur only in a small ring of area around the periphery of the first detector. At the 60° incidence angle, a proton of energy 55 MeV can penetrate a 1.5-g/cm² shield and the two detectors, leaving 0.5 MeV in the first detector and less than 0.4 MeV in the second. Thus, these protons can cause spurious, unwanted counts.

To maximize the counting rates for the LET spectrometer, it may be desirable to use a collimator with a half angle greater than 60° . In this case, the second detector greater than 2.8 cm² is used to guarantee anticoincidence. However, the maximum proton energy stopped in the first detector will increase as a function of slant thickness, as discussed previously.

3. MAXIMUM ENERGY DEPOSITED BY PROTONS

In an isotropic flux, more particles pass through a given square centimeter of material surface at angles of incidence other than normal to the surface. Mathematically, the flux striking a given square centimeter of surface at a given angle of incidence is proportional to the product of the sine and cosine of the given angle measured from the normal to the area. That is, very little flux is perpendicular to the surface ($\sin \theta \rightarrow 0$ as $\theta \rightarrow 0^\circ$) and very little cross section area is exposed to the flux parallel to the surface ($\cos \theta \rightarrow 0$ as $\theta \rightarrow 90^\circ$). Consequently, flux incident at angles other than 45° is very important to the count rate in the channel for energies > 18.5 MeV. This is because the first detector can stop higher energy protons as the angle of incidence increases. Table 9 indicates the energies deposited by protons just stopped in the 2-mm detector as a function of the angle of incidence.

From table 9 it is evident that protons cannot be stopped in the first detector at angles of incidence greater than 15° without producing pulses energetic enough to contaminate the >18.5 -MeV alpha particle channel. However, this condition can be modified either by restricting the angle of incidence by a collimator or by increasing the threshold of alpha channel to correspond with the maximum angle of incidence.

Table 9

MAXIMUM PROTON ENERGY DEPOSITED AS A FUNCTION OF ANGLE OF INCIDENCE

<u>Angle of incidence (degrees)</u>	<u>Energy (MeV)</u>
75	39.0
70	33.0
60	26.6
45	22.0
30	19.6
15	18.54

4. LEAKAGE PARTICLES

The relative importance of the leakage of protons can be obtained qualitatively from figure 50, where the penetrations spectra are presented for 17-gm/cm² and 34.8-gm/cm² tungsten shields (106.5 and 160 MeV). It is apparent that the flux attenuated by the shield is about one-tenth that unattenuated by the shield. The second or anticoincidence detector provides protection from the rear 2 π steradians. However, anticoincidence will not be provided from the rear at the detector edge for protons having angles of incidence greater than 60°.

For the forward 2 π steradians, the counts from a given incident angle are proportional to $\sin \theta \cos \theta$. Integrating this function gives $1/2 \sin^2 \theta$, or 0.5, for θ equal 0 to $\pi/2$. Ten percent of the counts are due to the flux with incident angles <13° because $1/2 \sin^2 13^\circ = 0.05$, or 10 percent of 0.5.

Assuming a collimator with a 13° half angle, 10 percent of the possible counts are unattenuated by the shield. That flux attenuated by the collimator represents 90 percent of the count rate and is reduced an order of magnitude to 9 percent of the original unattenuated count rate. Thus, the leakage count rate in this case is about one-half of the counts in any given energy channel. Opening the collimator improves the ratio of unattenuated protons, although the definition of particles >18.5 MeV is degraded.

5. OTHER RADIATION

In addition to protons and alpha particles, the LET spectrometer can detect electrons, bremsstrahlung, and galactic cosmic rays (GCR). The fission electrons trapped in the magnetosphere have decayed to the point that electron anomaly data obtained in November 1966 have been interpreted to contain a natural spectrum of the form $j = 8.8 \times 10^4 e^{-3.4E}$ electrons/cm²/sec MeV or $J(>E) = 163 \times 10^4 e^{-3.4E}$. This spectrum represents 1.087×10^3 electrons/cm²/sec, $E > 0.5$ MeV, and 0.33 electrons/cm²/sec, $E > 2.0$ MeV. Electrons of less than 2 MeV cannot deposit 0.5 MeV in the first detector after penetrating 1 gm/cm² of aluminum. The Vette electrons for 1968 include the Starfish electrons which, when decayed three years, give 0.77 electrons/cm²/sec, $E > 2.0$ MeV. The electron count rate in the 0.5- to 2-MeV channel thus will approach that of the protons when the collimator is small and the spacecraft shielding is about 1 gm/cm². With larger collimator half angles and greater spacecraft shielding (2 gm/cm²), the electron fluxes would appear to be small due to the flatness of the spectra.

Even when the electrons are stopped by the spacecraft and the spectrometer shielding, bremsstrahlung will be produced by the stopping of the electrons. Bremsstrahlung calculations performed for the electron spectrum at $L = 1.3$ show that the ratio of photons > 0.5 MeV to electrons > 2.0 MeV is 0.03. This ratio is low due to the fact that in 1965 the electron spectrum was flat for energies < 2 MeV. Calculations performed for the Vette AE3 spectrum indicate that the ratio becomes 1.0 due to the steepness of the spectrum ($J = Ae^{-3.4E}$). The weighted ratio, $0.33 (1.0) + 0.77 (0.03)$, is 0.35. As the bremsstrahlung flux and efficiency are both less than for protons, the counts due to bremsstrahlung are considered very small.

Galactic cosmic rays (GCR) which penetrate the edge of the first detector at angles of incidence greater than 60° can possibly miss the anticoincidence detector. Because of the small GCR flux, the small area affected, and the small fraction of flux arriving from directions which effectively miss the second detector, this flux is considered to be an insignificant source of possible miscellaneous counts in the 0.5- to 2-MeV channel.

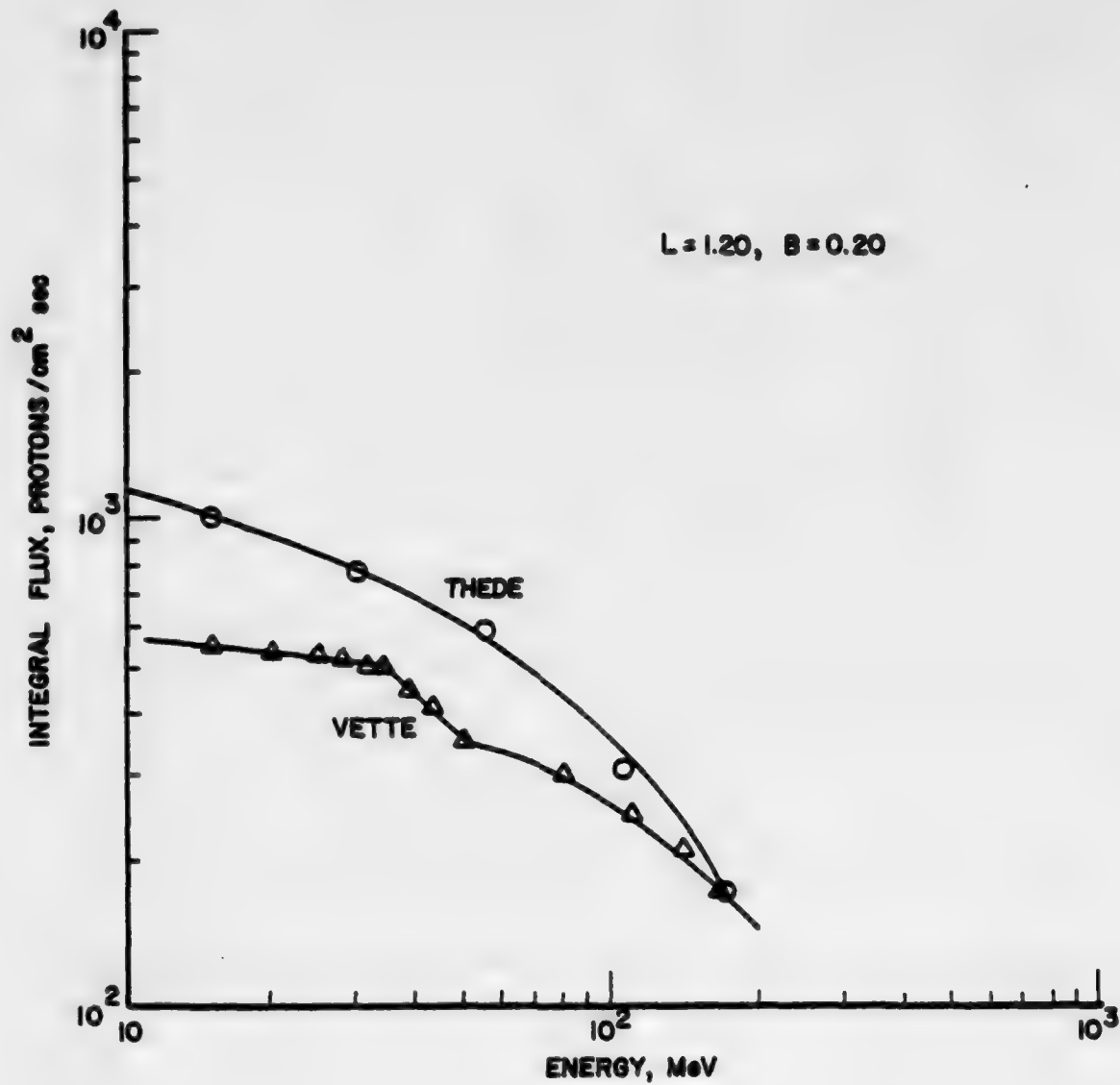


Figure 47. Proton Integral Flux Energy Spectra

AD-A032 409

AIR FORCE WEAPONS LAB KIRTLAND AFB N MEX
SKYLAB II - RADIATION DOSIMETRY SYSTEMS AND FLIGHT RESULTS.(U)
SEP 76 G C AINSWORTH, M F SCHNEIDER

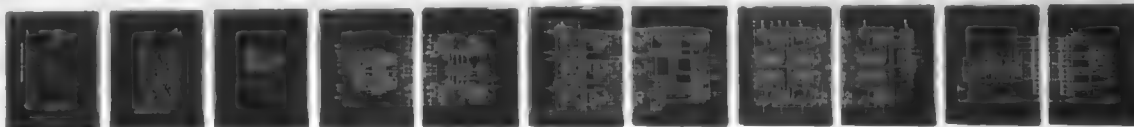
F/G 18/4

UNCLASSIFIED

AFWL-TR-73-222

NL

2 OF 2
ADA
032 409



END
DATE
FILMED
3 77
NTIS

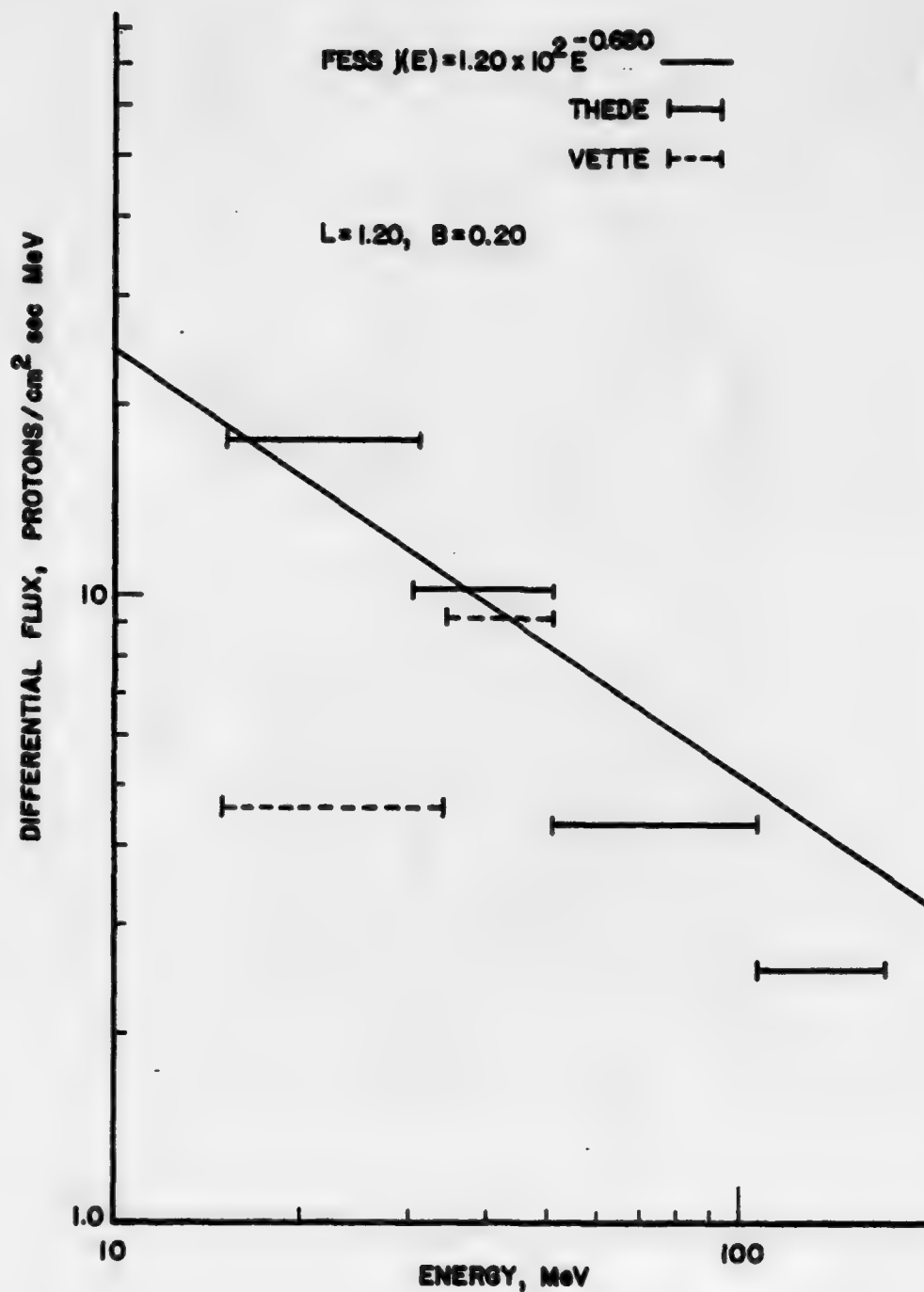


Figure 48. Proton Differential Flux Energy Spectra

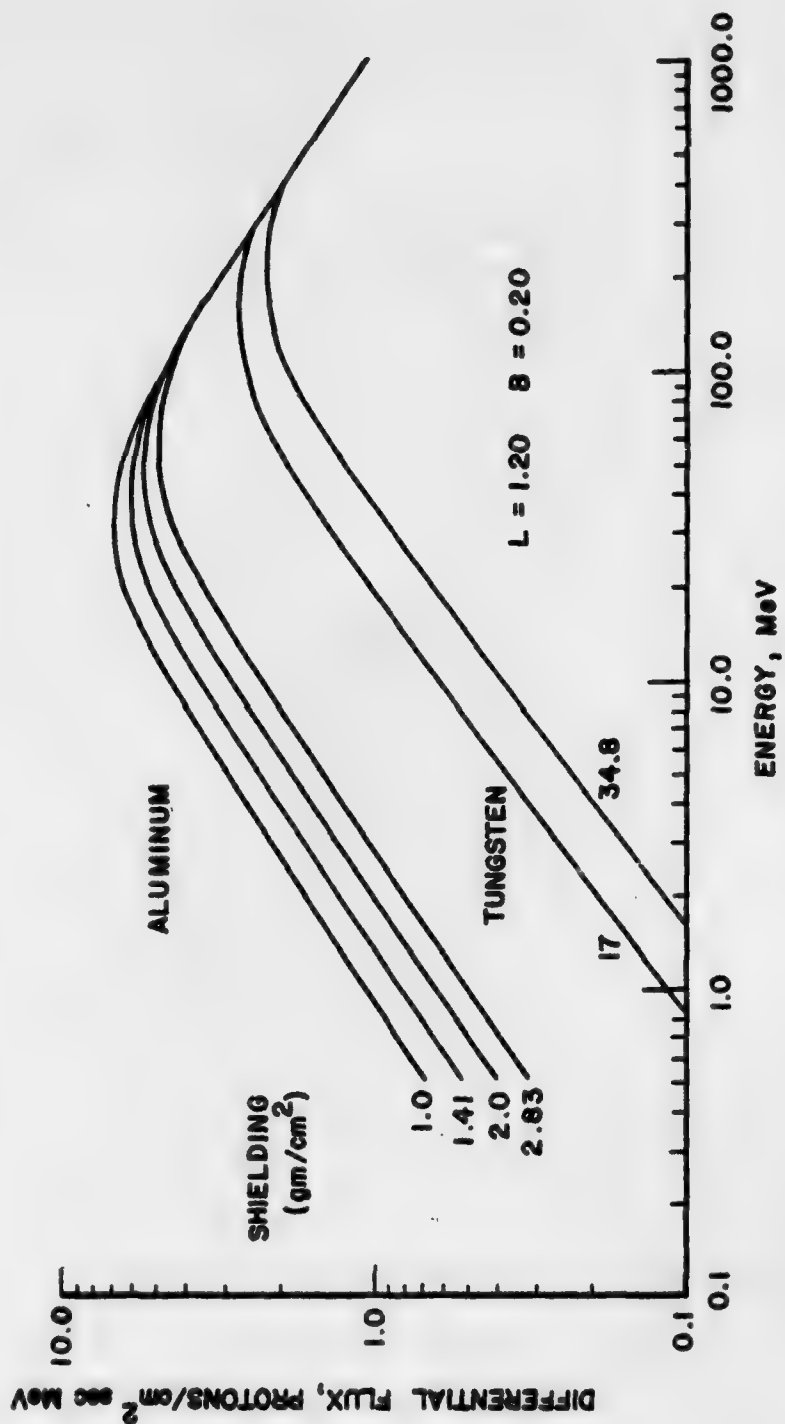


Figure 49. Differential Proton Penetration Spectra

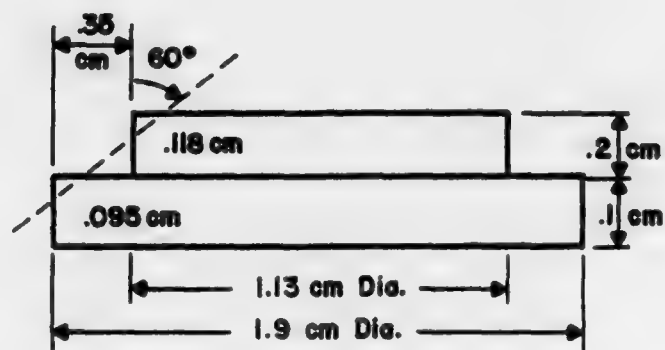


Figure 50. Proton Penetration Geometry

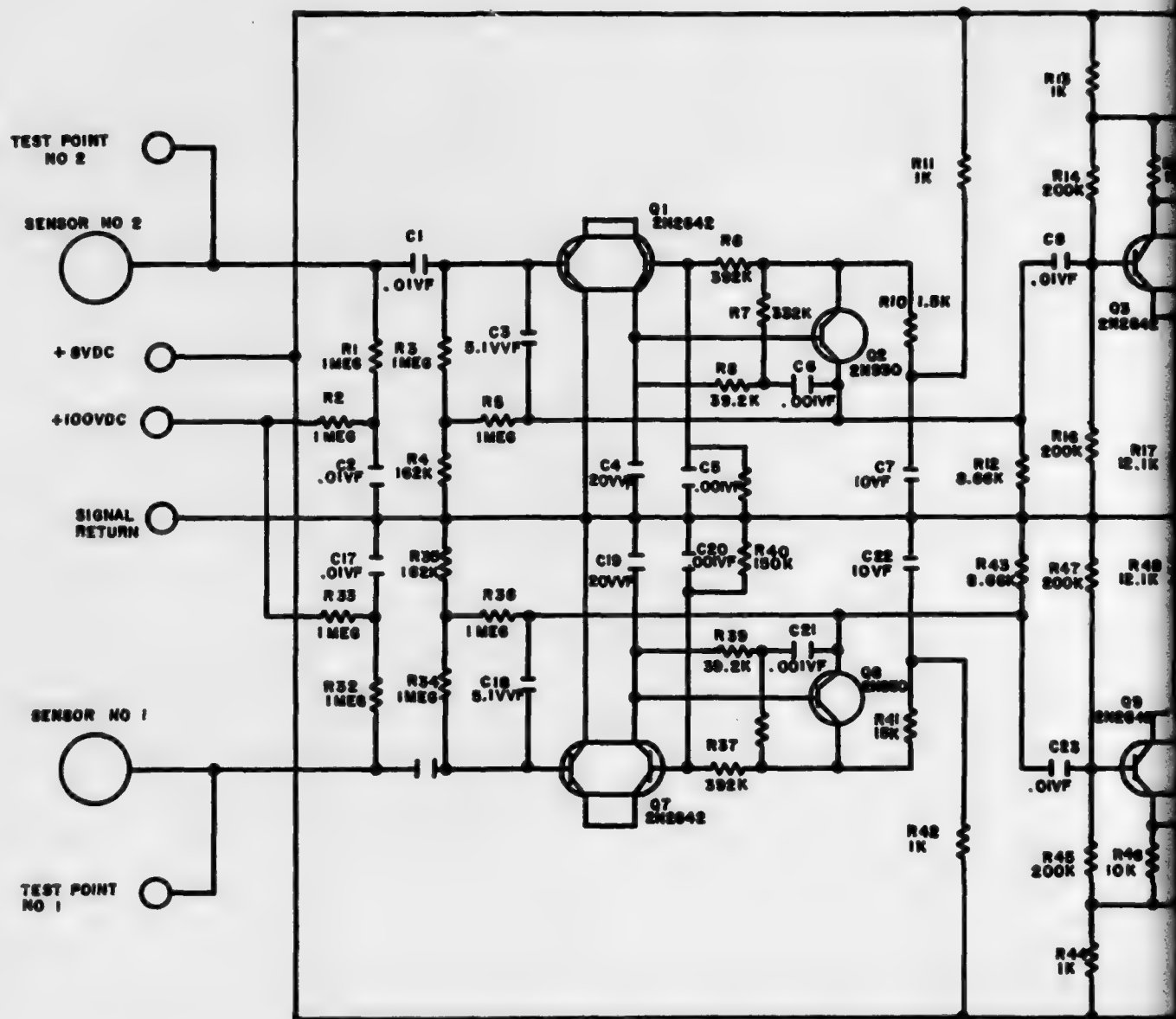
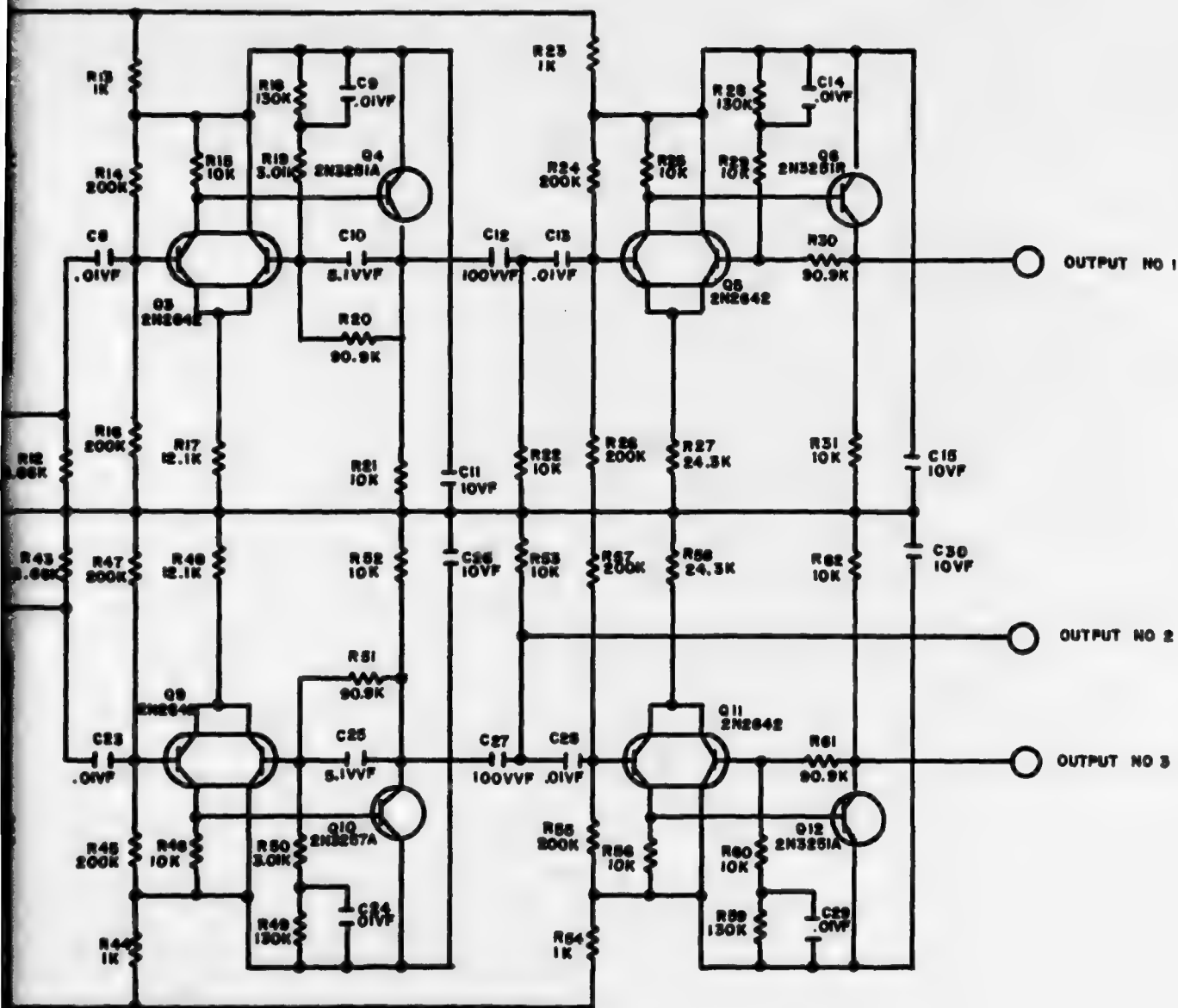
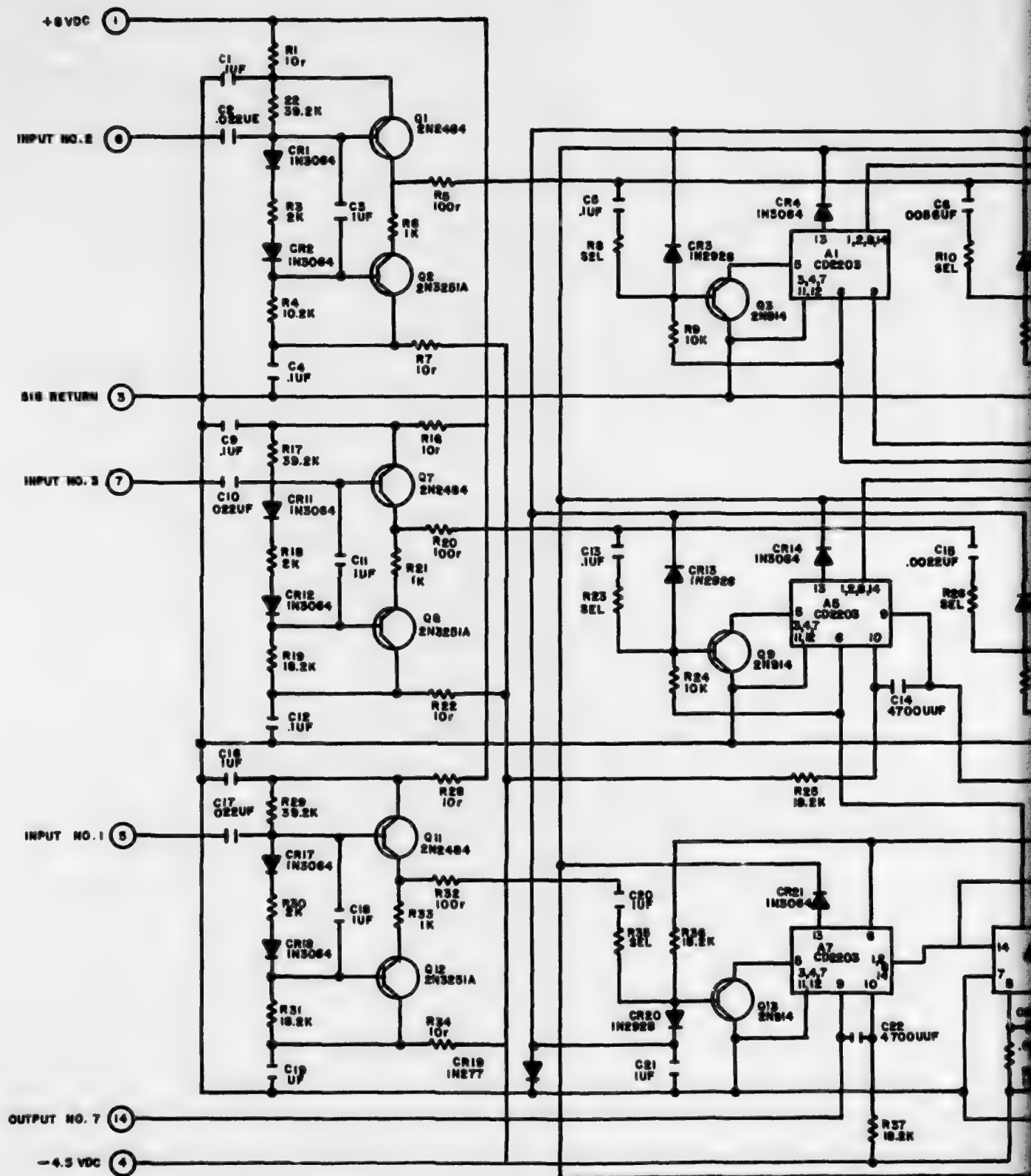


Figure 22. Schematic Detectors and Preamplifiers
97





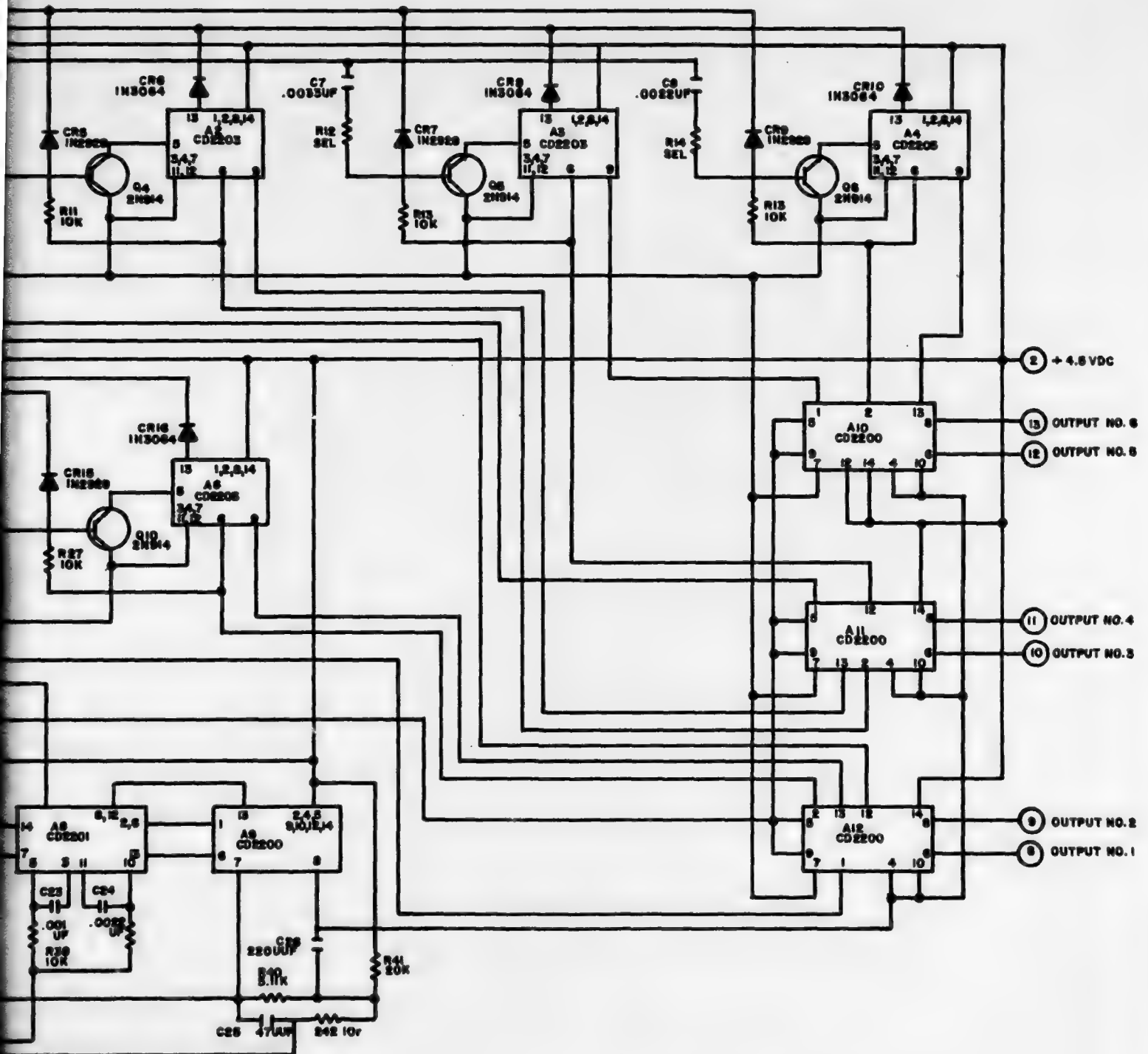


Figure 23. Schematic Signal Analyzer

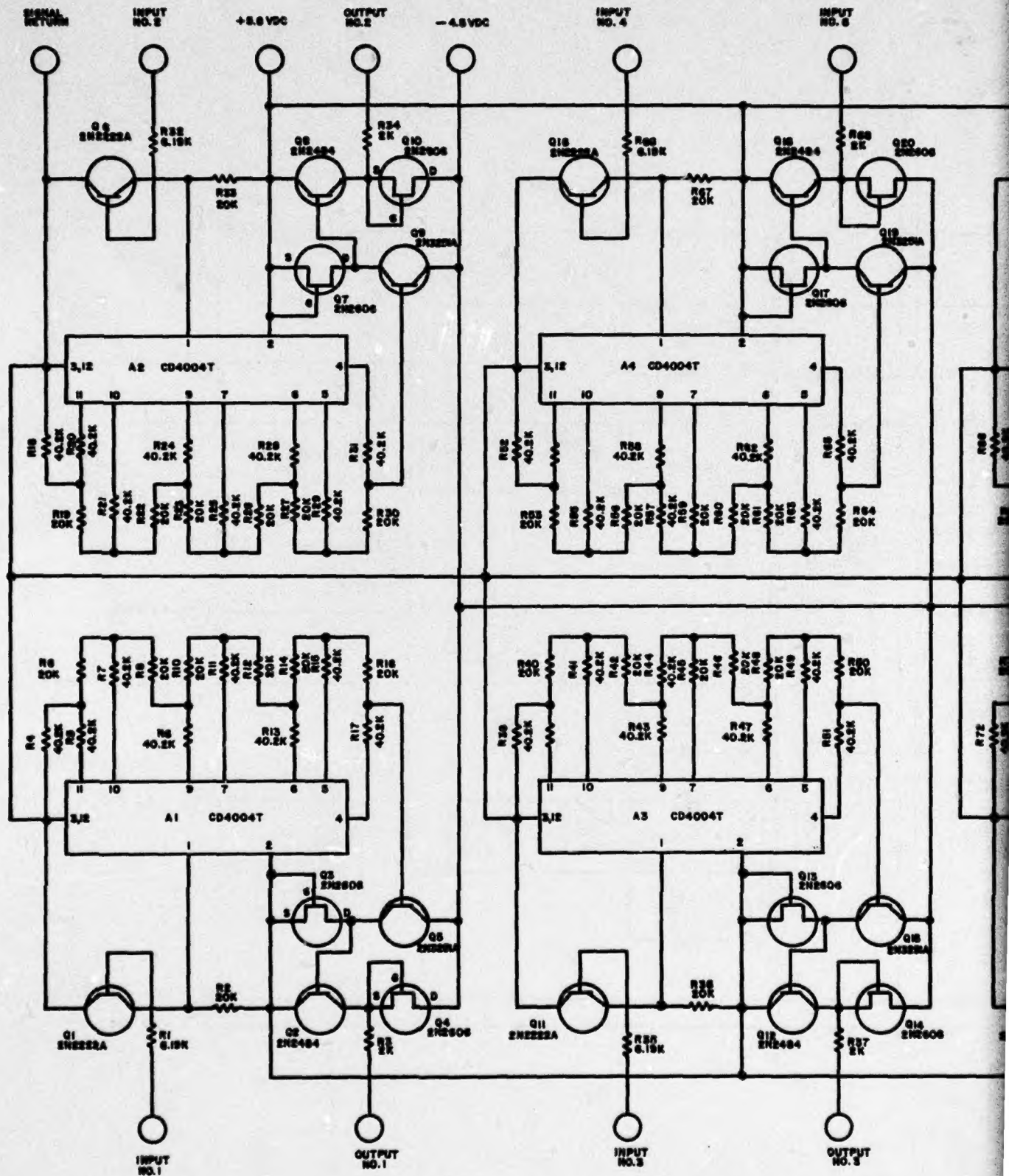
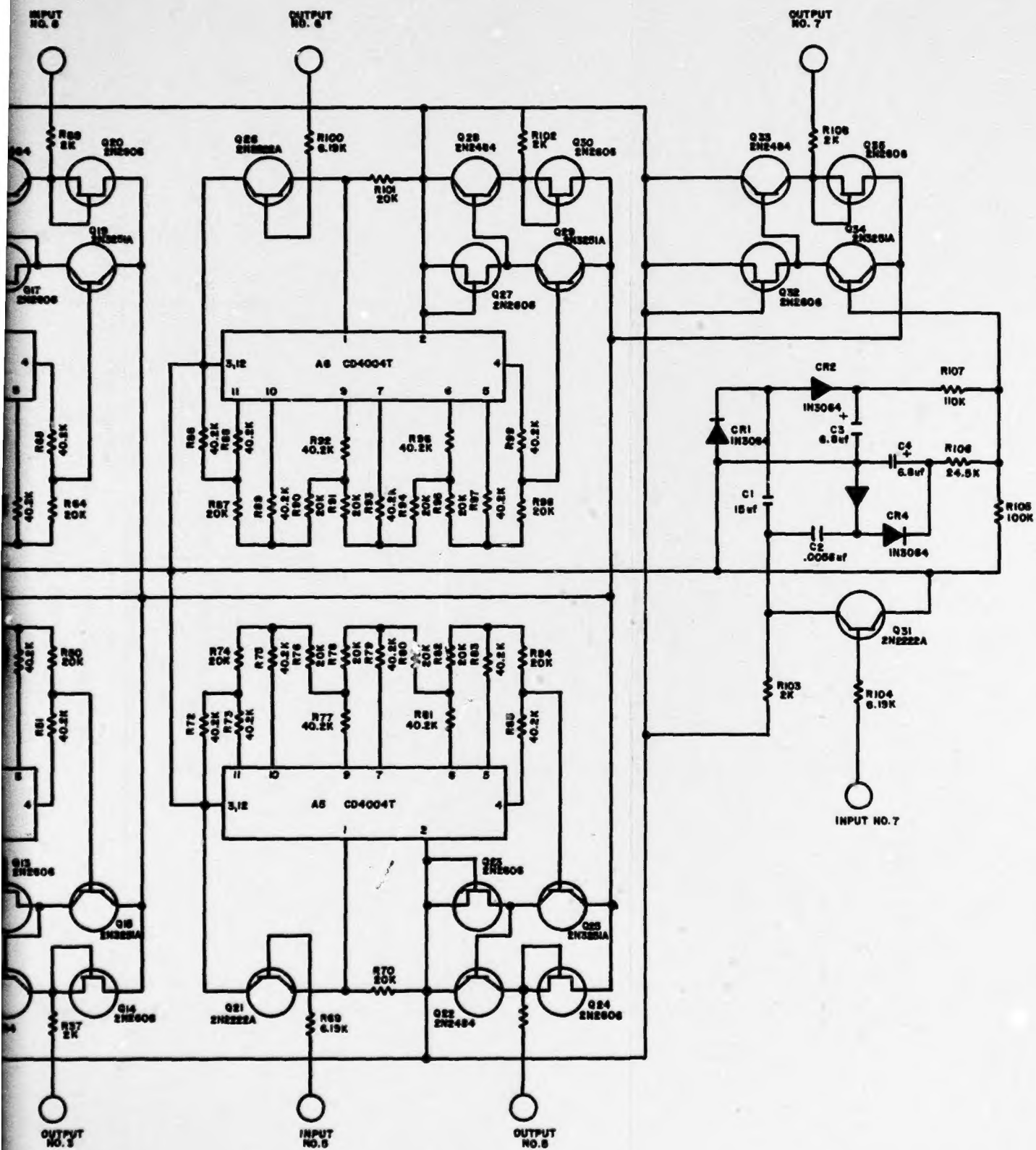
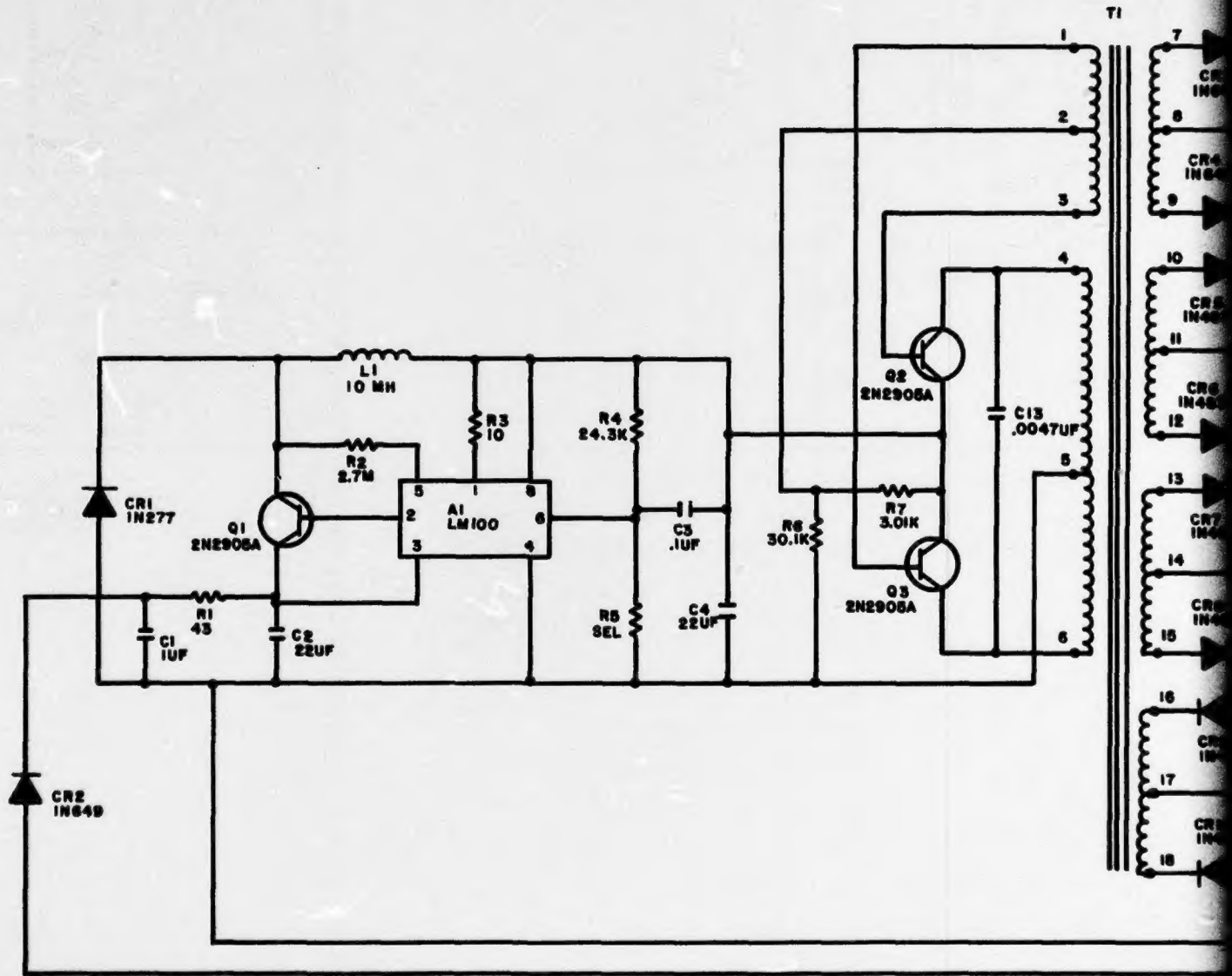


Figure 24. Schematic Counter and Output





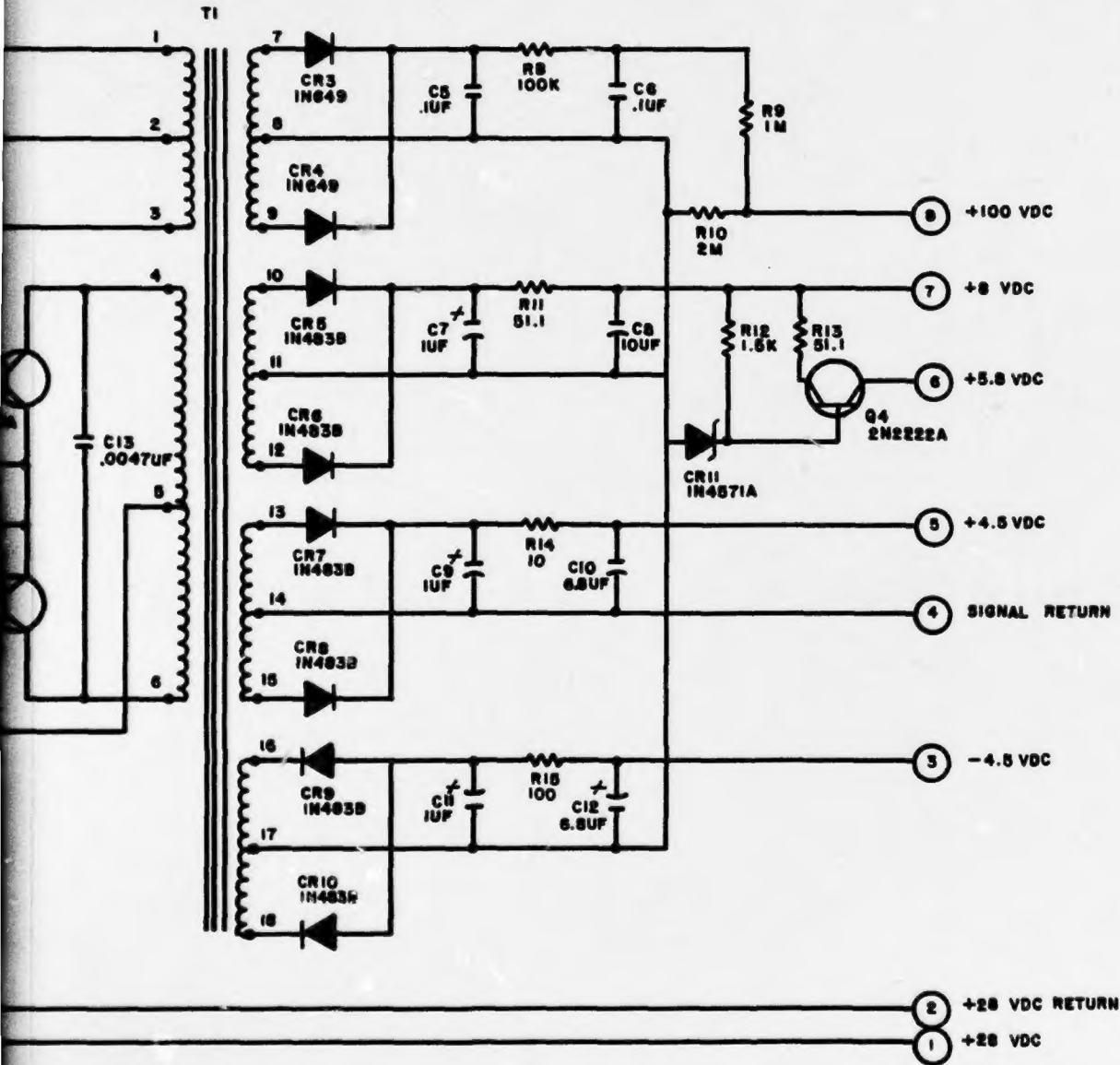


Figure 26. Schematic of Power Supply